DEVELOPMENT OF HIGH PERFORMANCE LONG WAVELENGTH
INFRARED HGCDTE FOCAL PLANE ARRAYS

A THESIS SUBMITTED TO
THE GRADUATE SCHOOL OF NATURAL AND APPLIED SCIENCES
OF
MIDDLE EAST TECHNICAL UNIVERSITY

BY

BERNA BARUTCU

IN PARTIAL FULFILLMENT OF THE REQUIREMENTS
FOR
THE DEGREE OF MASTER OF SCIENCE
IN
ELECTRICAL AND ELECTRONICS ENGINEERING

SEPTEMBER 2019

Approval of the thesis:

DEVELOPMENT OF HIGH PERFORMANCE LONG WAVELENGTH INFRARED HGCDTE FOCAL PLANE ARRAYS

submitted by **BERNA BARUTCU** in partial fulfillment of the requirements for the degree of **Master of Science in Electrical and Electronics Engineering Department, Middle East Technical University** by,

Prof. Dr. Halil Kalıpçılar
Dean, Graduate School of **Natural and Applied Sciences**   _____

Prof. Dr. İlkay Ulusoy
Head of Department, **Electrical and Electronics Eng.**   _____

Prof. Dr. Cengiz Beşikci
Supervisor, **Electrical and Electronics Eng., METU**   _____

Examining Committee Members:

Prof. Dr. Haluk Külah
Electrical and Electronics Eng., METU   _____

Prof. Dr. Cengiz Beşikci
Electrical and Electronics Eng., METU   _____

Prof. Dr. Mehmet Parlak
Physics, METU   _____

Prof. Dr. Yüksel Ergün
Physics, Anadolu University   _____

Assist. Prof. Dr. Serdar Kocaman
Electrical and Electronics Eng., METU   _____

Date: 11.09.2019

I hereby declare that all information in this document has been obtained and presented in accordance with academic rules and ethical conduct. I also declare that, as required by these rules and conduct, I have fully cited and referenced all material and results that are not original to this work.

Name, Surname: Berna Barutcu

Signature:

ABSTRACT

DEVELOPMENT OF HIGH PERFORMANCE LONG WAVELENGTH INFRARED HGCDTE FOCAL PLANE ARRAYS

Barutcu, Berna
Master of Science, Electrical and Electronics Engineering
Supervisor: Prof. Dr. Cengiz Beşikci

September 2019, 108 pages

This thesis study reports the characterization of long wavelength infrared (LWIR) HgCdTe photovoltaic detectors with the p on n structure and 9.5 μm cut-off wavelength grown by molecular beam epitaxy on CdZnTe substrates and fabricated with different passivation processes. The characterization study was conducted at both pixel and focal plane array (FPA) levels. While the detectors exhibit diffusion dominated dark current at temperatures at and above 130 K under reverse bias voltages typically used in imaging applications, the major component of the dark current is trap assisted tunneling (TAT) at low temperatures (80 K). We carried out a detailed characterization study on the detector pixels with 30 μm pitch in order to identify the properties of the traps establishing the generation-recombination (G-R) and the TAT currents. Dark current analysis study yielded a hole trap in the n-side at an energy of $0.36E_g$ (E_g is the bandgap of the absorber material) measured from the valence band edge with a density in the order of 10^{14} cm^{-3}. While this trap has been reported in the literature, we explored the further properties of this trap including the capture cross section characteristics exhibiting capture barrier as well as the effect of it on the signal to noise ratio of the detector through the G-R and TAT components of the dark current contributing to the 1/f noise of the detectors.

Shunt (ohmic) leakage current was observed in the detectors fabricated with different passivation processes including CdTe and CdTe/ZnS subjected to different annealing conditions. The absence of this leakage current in a detector fabricated with the same material but with properly applied and processed CdTe passivation suggests that it originates from the surface. We have also observed that the shunt current component introduces significant 1/f noise with a noise coefficient, α, in the order of that of the G-R current (10^{-3}). The TAT current is observed to introduce 1/f noise to exhibit noise current at 1 Hz expressed as $0.8 \times 10^{-6}(I_{TAT})^{0.57}$.

The detectors exhibit a peak specific detectivity of ~1×10^{11} cmHz$^{1/2}$/W at 78 K with f/2 optics corresponding to temporal noise equivalent temperature difference of ~20 mK with an integration time as low as 400 μs. We also present the characteristics of a mid-format (320x256) focal plane array (FPA) fabricated with the same material in order to assess the FPA level performance of the detectors.

Keywords: LWIR HgCdTe, Dark Current Modeling, Trap Assisted Tunneling, Noise Analysis

ÖZ

YÜKSEK PERFORMANSLI UZUN DALGABOYU KIZILÖTESİ CIVA KADMİYUM TELLÜR ODAK DÜZLEM MATRİSLERİNİN GELİŞTİRİLMESİ

Barutcu, Berna
Yüksek Lisans, Elektrik ve Elektronik Mühendisliği
Tez Danışmanı: Prof. Dr. Cengiz Beşikci

Eylül 2019, 108 sayfa

Bu tez çalışmasında CdZnTe pullar üzerine büyütülüp farklı pasivasyon prosesleri kullanılarak üretilmiş olan n üzeri p yapıya ve 9.5 μm kesim dalgaboyuna sahip uzun dalgaboyu kızılötesi HgCdTe fotovoltaik dedektörlerin karakterizasyonu rapor edilmektedir. Dedektörler, görüntüleme uygulamalarında tipik olarak kullanılmakta olan ters eğimleme gerilimleri altında 130 K ve üzerinde sıcaklıklarda difüzyon baskın karanlık akım özellikleri sergilerken, 80 K ve altında karanlık akım ana bileşeni tuzak yardımlı tünelleme olmaktadır. Çoğalma-birleşme ve tuzak yardımlı tünelleme akımlarını oluşturan tuzakların özelliklerini inceleyebilmek için 30 μm piksel adımına sahip dedektör piksellerinin üzerinde detaylı bir karakterizasyon çalışması yürütülmüştür. Karanlık akım analizi sonucunda, n tarafında valans bant kenarından ölçülmüş olan 0.36 E_g (E_g malzemenin enerji boşluğu) enerjisine ve 10^{14} cm^{-3} yoğunluğa sahip boşluk tuzakları bulunmuştur. Literatürde raporlanmış olan bu tuzakların özellikleri derinlemesine çalışılmıştır. Tuzakların yakalama bariyeri olarak davranmasını sağlayan yakalama kesiti ve tuzak yakalama kesitinin karanlık akımın çoğalma-birleşme ve tuzak yardımlı tünelleme bileşenleri yoluyla sinyal gürültü oranına ve dolayısıyla 1/f gürültüsüne etkileri incelenmiştir.

CdTe ve CdTe/ZnS katmanlarının farklı koşullarda tavlanmasıyla elde edilen değişik pasivasyon sürecine tabi tutulan dedektörlerde paralel kaçak akım gözlenmiştir. Paralel kaçak akımın düzgün uygulanmış CdTe pasivasyona sahip aynı malzemeden üretilmiş dedektörlerde görülmemesi paralel kaçak akımın yüzeyden kaynaklandığı düşündürmektedir. Ayrıca bu yüzey kaçak akım bileşeninin 1/f gürültüsüne çoğalma-birleşme akımı seviyesinde (10^{-3}) etki ettiği gözlemlenmiştir. Tuzak yardımlı tünelleme akımının ise 1 Hz frekansta $0.8 \times 10^{-6}(I_{TAT})^{0.57}$ ilişkisi ile 1/f gürültüsü oluşturduğu bulunmuştur.

Dedektörler 78 K'de f/2 optik ve ~400 μs gibi oldukça düşük bir entegrasyon süresi ile ~20 mK zamansal gürültü eşdeğer sıcaklık farkına karşılık gelen $\sim 1 \times 10^{11}$ cmHz$^{1/2}$/W tepe dedektivite değeri göstermiştir. Ayrıca, dedektörlerin odak düzlem matrisi (ODM) seviyesinde performansını değerlendirmek için aynı malzeme kullanılarak üretilmiş olan orta formatlı (320x256) ODM karakterizasyonu sunulmuştur.

Anahtar Kelimeler: LWIR HgCdTe, Karanlık Akım Modellemesi, Tuzak Yardımlı Tünelleme, Gürültü Analizi

To my family

ACKNOWLEDGEMENTS

TABLE OF CONTENTS

LIST OF TABLES

TABLES

LIST OF FIGURES

FIGURES

xvi

CHAPTER 1

INTRODUCTION

Long-wavelength infrared (LWIR) and mid-wavelength infrared (MWIR) regions are widely used for many applications such as medical, commercial, energy conservation and military. $Hg_{1-x}Cd_xTe$ is one of the most critical material for detection applications over entire electromagnetic spectrum including MWIR and LWIR. While the material is very difficult and sensitive to handle and process, it is still the dominating material especially in the LWIR band for thermal imaging. The advantages of $Hg_{1-x}Cd_xTe$ arises from the adjustable and direct band-gap, high and sharp absorption coefficient and the suitability of a lattice-matched substrate (CdZnTe) which is transparent to infrared radiation. This thesis study reports the fabrication and detailed characterization of LWIR HgCdTe focal plane array (FPA) having 320x256 format and 30 μm pixel pitch. $Hg_{1-x}Cd_xTe$ epilayer with x=0.23 used in this study was grown by molecular beam epitaxy (MBE) at the Quantum Devices and Nanophotonics Research Laboratory of the Electrical and Electronics Engineering Department, Middle East Technical University (METU).

The first chapter of this thesis is a short introduction to infrared sensors including figure of merits. Chapter 2 is devoted to the history and properties of $Hg_{1-x}Cd_xTe$, as well as the status of HgCdTe detector technology. The detector epilayer structure and fabrication procedure details of test arrays and the 320x256 FPA are given in Chapter 3. Electrical and optical characterization of test pixels and FPA including dark and photo current measurements, diffusion length analysis, responsivity/detectivity measurements are summarized in Chapter 4. Conclusion including future works is presented as a final chapter.

In the following section, basics of infrared radiation, infrared detectors and figures of merit for focal plane arrays and infrared detectors are presented.

1.1. Basics of Infrared Radiation

In the year 1800, Sir William Herschel explored infrared (IR) radiation. The aim of his experiment was to measure the energy distribution of sunlight by using a prism and thermometer in sunlight. Herschel noticed that the temperature was even higher when a thermometer was exposed beyond the visible light. He concluded that there must be another type of light which is now called infrared [1]. Besides, he continued his experiments, and he found that the behavior of invisible lights was similar to visible ones and all obeyed reflection, absorption and transmission rules [2].

All objects having a temperature above 0 K (absolute zero) emit and absorb electromagnetic radiation. Since the wavelength of the thermal emission of very hot objects is in the visible range, human eye can detect these objects. However, the thermal emission of room temperature or colder objects can only be detected by thermal camera. For all matters including blackbody, the amount of energy emitted at a specific wavelength depends on the emissivity and temperature of the object. Blackbody which absorbs all incoming radiation for entire spectrum is an ideal emitter, and its thermal radiation is only dependent on temperature. With the contribution of Sir William Herschel, Balfour Stewart and Gustav Kirchhoff, Max Planck established the formula which states the blackbody having a temperature above absolute zero (0 K) emission spectrum which is known as Planck's Law. The blackbody spectral exitance is expressed by

$$M_\lambda(\lambda, T) = \frac{2\pi hc^2}{\lambda^5 \left(e^{\frac{hc}{\lambda kT}} - 1\right)} \quad \left(\frac{W}{cm^2 - \mu m}\right) \tag{1.1}$$

where k is Boltzmann's constant, c is the speed of light in vacuum, h is Planck's constant, T is the absolute temperature of the blackbody in Kelvin and λ is the radiation wavelength.

The infrared band is between the visible and the millimeter wave regions corresponding to wavelength of 0.7 μm to 1 mm. The blackbody exitance for different temperatures is shown in Figure 1.1 including both visible and infrared bands. The spectral exitance curves have maxima at certain temperatures. Wien's law states the displacement of the maximum as function of object temperature as follows [3]

$$\lambda_{max}(T) = \frac{2898}{T} \quad \mu m \qquad (1.2)$$

where λ_{max} is the wavelength which corresponds to maximum emission of blackbody, and T is the blackbody temperature (K).
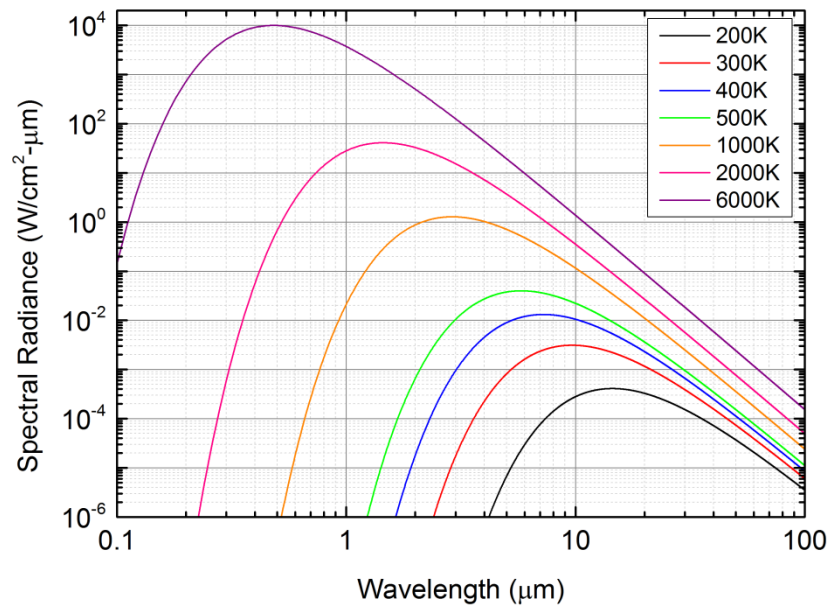
Figure 1.1. The spectral radiation of blackbody for different temperatures.

As Wien Law states, the object temperature is inversely proportional to the wavelength of peak emission. For the hotter objects like Sun (6000 K), the maximum emission occurs at the visible wavelength corresponding to yellow color. The peak occurs at around 10 μm for objects near room temperature.

The atmosphere attenuates the infrared radiation by two different mechanisms, namely absorption and scattering. Water vapor, nitrogen, oxygen, methane, carbon monoxide, ozone and carbon dioxide are the most abundant gases in the atmosphere. These gasses absorb the infrared radiation at some wavelengths. Atmospheric transmission spectrum at sea level is given in Figure 1.2. The infrared radiation windows determined by transmission are described as follows:

Near infrared (NIR) band is 0.7 – 1.1 μm.

Short wavelength infrared (SWIR) band is 1.1 – 2.5 μm.

Mid wavelength infrared (MWIR) band is 3.0 – 5.5 μm.

Long wavelength infrared (LWIR) band is 8.0 – 14.0 μm.
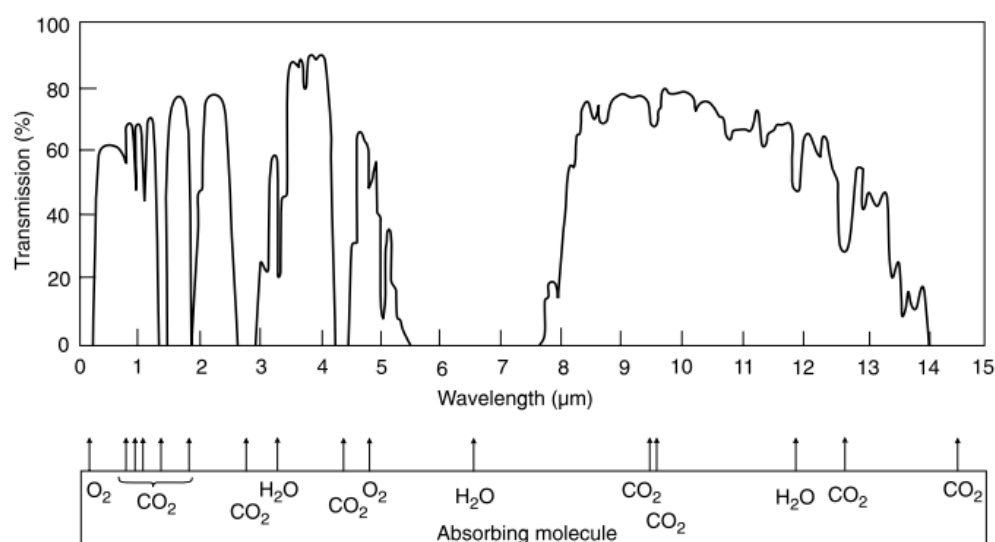
Figure 1.2. Transmission of atmosphere at sea level [4].

In addition to absorption, atmosphere also scatters the infrared radiation. There are two different scattering mechanisms, namely Rayleigh and Mie scattering. Rayleigh scattering is observed when the radiation interacts with particles and molecules that are smaller in diameter than the incoming radiation wavelength. This scattering is inversely correlated to fourth power of wavelength, hence with the increasing of wavelength of radiation, the scattering due to Rayleigh scattering mechanism becomes

negligible. On the other hand, when the particle diameter is comparable with the wavelength of incident light, the dominant effect is seen to arise from wave nature of radiation, which results in Mie scattering. It depends on the size, concentration and distribution of particles, and environmental conditions affect the Mie scattering. The light scattering regions with respect to particle radius and wavelength are summarized in Figure 1.3.
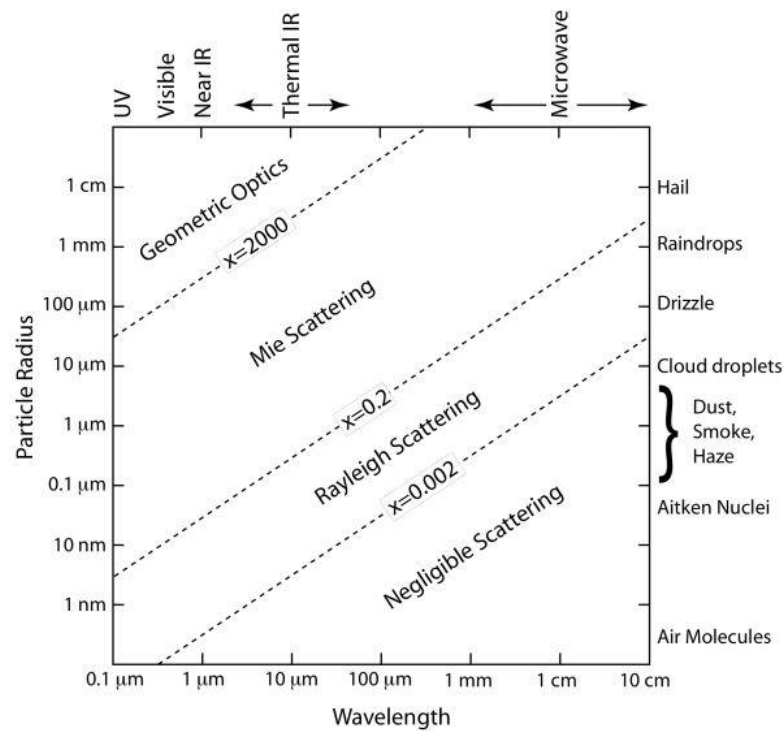
Figure 1.3. Single scattering depending on particle size, the light wavelength and the refractive index [5].

As can be seen from both spectral radiation spectra and Wien's Law, since the peak radiant power by room temperature targets is around 10 μm, LWIR detectors receive higher photon flux from ambient temperature targets. At the same time, the 8-14 μm band has better transmission through mist and smoke. On the other hand, one can prefer using MWIR detectors, the 3-5 μm band, if higher contrast is required [4].

1.2. Figures of Merit for Infrared Detectors

The performance of focal plane arrays is usually defined by various figures of merit to compare different technologies. The most important ones are responsivity, quantum efficiency, noise equivalent temperature difference and detectivity. These parameters will briefly be given in the next sections.

1.2.1. Quantum Efficiency

A measure of the probability of the contribution of the photons falling on the detector to the photocurrent is defined as quantum efficiency. There are different mechanisms which affect the quantum efficiency. In the case of reflections from the upper surfaces and the inadequate thickness of the absorber layer, incoming photons are not totally absorbed decreasing the external quantum efficiency. Even if absorption occurs, it may not lead to the creation of electron-hole pair, or the created electron-hole pairs may be lost by recombination before they can contribute to the photocurrent. These events determine the internal quantum efficiency. By considering both internal and external quantum efficiency, the overall quantum efficiency is described as follows

$$\eta = \frac{\eta_{int}(1-r)(1-e^{-\alpha t})}{1-re^{-\alpha t}} \qquad (1.3)$$

where η_{int} is the internal quantum efficiency, t is thickness of the absorber layer, r is the reflection coefficient and α refers to absorption coefficient. Figure 1.4 summarizes quantum efficiency for different detector materials.
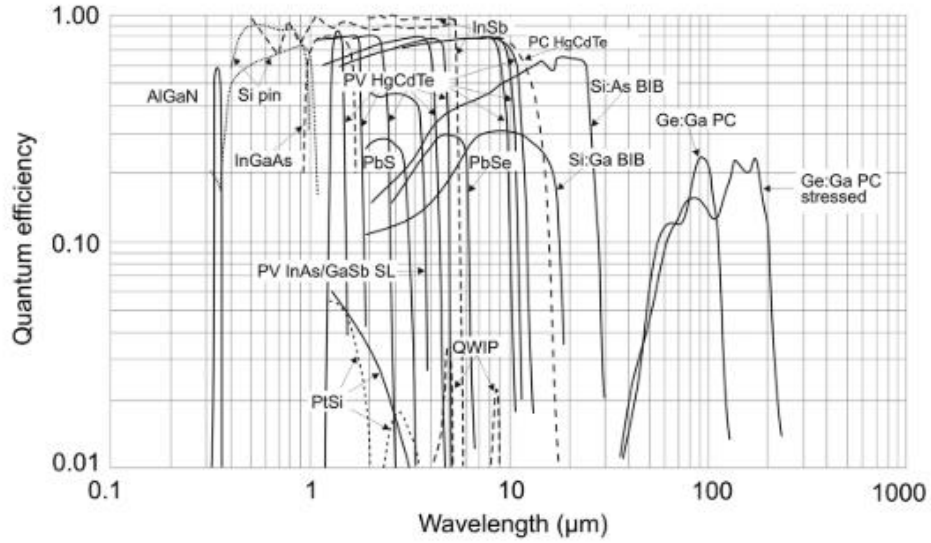
Figure 1.4. Quantum efficiencies of different detectors [6].

1.2.2. Responsivity

Responsivity is described as the output of the detector produced in response to incoming power on detector. The output of detector can be in the form of photocurrent or photovoltage.

$$Responsivity\ (R) = \frac{signal\ output\ (A\ or\ V)}{total\ incident\ power\ (W)}. \tag{1.4}$$

Responsivity can be expressed as follows

$$R(\lambda) = q\eta g\frac{\lambda}{hc}\ (A/W) \tag{1.5}$$

where λ is the wavelength, g is the photoconductive gain which is 1 for photovoltaic detectors, η is the quantum efficiency, and c is the speed of light in vacuum. Blackbody responsivity is another derivative of responsivity, and it is the signal output from a detector in response to 1 Watt of radiative power from a blackbody at temperature T which is expressed as

$$R_{BB}(T) = \frac{I_{photo}}{\phi} = \frac{\int_0^\infty R(\lambda)\phi(\lambda)d\lambda}{\int_0^\infty \phi(\lambda)d\lambda}. \qquad (1.6)$$

Although a large responsivity is necessary for good sensitivity, responsivity by itself does not provide any information about any intrinsic noise in the device. In other words, high responsivity does not mean that it enables high performance in low level background radiation case.

1.2.3. Noise

Noise is defined as fluctuations in the measured signal. A detector itself and a readout system are two sources of noises. Some noise sources cannot be avoided since they are fundamental mechanisms. Johnson (Nyquist or Thermal) noise, shot noise and capacitor noise are the fundamental noise components in infrared detectors.

1.2.3.1. Johnson (Thermal or Nyquist Noise)

Thermal fluctuations exist in a conductor when the temperature is above 0 K. Thermal noise is white noise, which means the noise level is not dependent on frequency. Thermal noise can be expressed as [7]

$$V_n(rms) = \sqrt{4kTR_D\Delta f} \qquad (1.7)$$

$$i_n(rms) = \sqrt{\frac{4kT\Delta f}{R_D}} \qquad (1.8)$$

where T is temperature, Δf is the measurement bandwidth and R_D is the dynamic resistance.

1.2.3.2. Shot (Photon) Noise

Shot noise arises because both photons and charge carriers are quantized. In photon detectors, a photon either excites an electron or not. Due to this quantization, a fluctuation occurs, and it affects the signal to noise ratio especially at low level background. Shot noise comes in sight when a bias voltage is applied, unlike Johnson

8

noise. Carrier generation is a random process depending on the random arrival of photons and quantum efficiency. Shot noise is observed in photovoltaic detectors where photogenerated charge carriers overcome a potential-energy barrier in order to contribute to the current. In open circuit photovoltaic detectors, since there is no bias voltage, shot noise is zero [8]. Shot noise is replaced by generation recombination noise in photoconductors. Shot noise current is expressed as

$$i_n(rms) = \sqrt{2q(I_{dark} + I_{photo})\Delta f} \qquad (1.9)$$

where Δf is the measurement bandwidth and q is the electron charge.

1.2.3.3. 1/f (Pink) Noise

1/f noise is present when the bias current flows, and it is absent in the open circuit photovoltaic detectors. It becomes dominant at low frequencies and starts to decrease with the increase of frequency. The noise arises in the signal over wide range of frequencies and becomes dominant below critical frequency. After a critical frequency, Johnson and shot noise become dominant. The typical noise spectrum of a photodetector is shown in Figure 1.5.
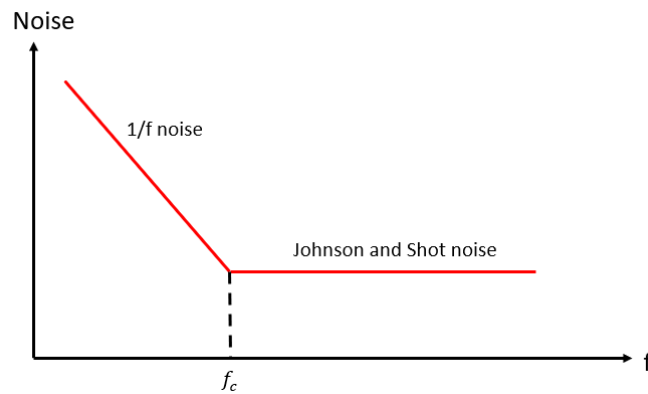
Figure 1.5. Frequency spectrum of noise.

1.2.3.4. Capacitor Noise

A real capacitor has a shunt resistance. Due to shunt resistance, thermal noise of capacitor should be taken into consideration. Capacitor noise voltage is expressed as

$$V_n(rms) = \sqrt{\frac{kT}{C}}$$ *(1.10)*

where C is the capacitance. With the increasing of shunt resistance, noise spectral density will decrease. On the other hand, the bandwidth will increase, and this eliminates the dependence of resistance value on capacitor noise voltage.

1.2.4. Signal-to-Noise Ratio

The signal-to-noise ratio (S/N) basically describes the cleanliness of a given signal. However, S/N by itself cannot indicate the performance of the detector. By applying more signal irradiance to the same detector, a better S/N ratio can be obtained.

1.2.5. Noise Equivalent Power

The noise equivalent power (NEP) equals to the incoming power generating an output signal which is equivalent to rms noise output. In other words, NEP is signal output level that yields a unity S/N. It indicates the minimum detectable radiation power, and it should be small for a good detector. NEP can be expressed by

$$NEP = \frac{\phi}{S/N} = \frac{v_n}{R_v} = \frac{i_n}{R_i}.$$ *(1.11)*

NEP by itself is insufficient to compare detector technologies, since it depends on test conditions (photon flux and bandwidth of measurement) and detector area.

1.2.6. Specific Detectivity

The inverse of NEP is defined as detectivity (D) of a detector

$$D = \frac{1}{NEP}.$$ *(1.12)*

Since the detectivity parameter still does not eliminate the dependency of the detector performance on the test conditions and detector area, both D and NEP are not useful to compare different detectors. The specific detectivity (D*) is introduced eliminate these dependencies. For a specific field of view and object temperature, D* value indicates the performance of the detector. D* should be high for good detectors. Specific detectivity is given by

$$D^* = \frac{\sqrt{A_d \Delta f}}{NEP} = \frac{\sqrt{A_d \Delta f}}{i_n} R_i \qquad (1.13)$$

where A_d is the detector area, R is the responsivity, and i_n is the noise of the detector.

1.2.7. Noise Equivalent Temperature Difference

Noise equivalent temperature difference (NETD) is described by the minimum detectable temperature difference between background and the target. NETD is a composite figure of merit similar to NEP, however even if it depends on the optic parameters such as system noise and f number, NETD is used as a figure of merit of a detector. NETD is the temperature difference that gives an output signal equivalent to rms noise level [9]. NETD is expressed as

$$NETD = \frac{(4F/\#^2 + 1)\sqrt{\Delta f}}{\sqrt{A_d} \int_0^\infty T(\lambda) D^*(\lambda) \frac{dM_{target}(\lambda)}{dT} d\lambda} \qquad (1.14)$$

where *F/#* is the f number expressed as the division of the focal length to the aperture diameter, *T* is the atmospheric transmission, *D** is the specific detectivity and *M* is the target spectral exitance.

1.3. Classification of IR Detectors

Infrared detectors operate based on the convergence of infrared radiation into electrical signals. The majority of IR detectors are divided into two sub-categories, photon and thermal. In thermal detectors, absorption of photons results in change in some physical properties of material which are used to generate an output signal.

Therefore, the nature of photon does not affect the detector's output, only the absorption mechanism is essential for imaging systems. Thermal detectors do not require any cooling system, and they can operate at room temperature. However, even if they are light, durable, reliable and exhibit a low-cost technology, they are not suitable for many applications requiring fast response and high detectivity. There are different types of uncooled detectors such as bolometers, thermocouples, pyroelectric detectors and Golay cells [1].

In photon detectors, the radiation interacts with electrons within the material and is absorbed by three different ways. The fundamental optical excitation processes are shown in Figure 1.6. In quantum wells, intersubband absorption occurs between the energy levels of a quantum well formed in the valance or conduction band. In addition to quantum wells and bulk semiconductors, type-II superlattice is also based on optical excitation processes. The energy difference between the first heavy-hole state and the conduction miniband determines the bandgap in type-II superlattice. [6].

In intrinsic detectors, the fundamental bandgap of the semiconductor limits the wavelength of the detection and are mostly available for detection below 20 μm wavelength. Photons with lower energy than bandgap cannot excite any electron from valance band, and the response of the detectors drops very rapidly. For intrinsic detectors, HgCdTe, InGaAs and InSb are widely used. They operate as photovoltaic or photoconductive detectors.
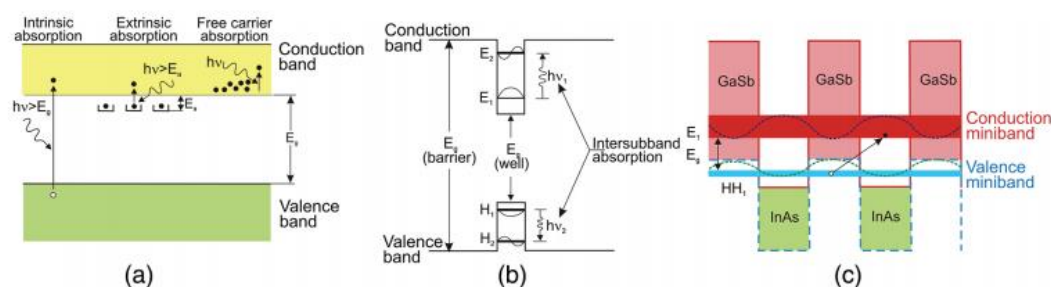
Figure 1.6. Optical excitation processes in: (a) bulk semiconductors, (b) quantum wells, and (c) type-II InAs/GaSb superlattices [6].

In photoconductive devices, the working principle depends on change in material resistivity. With the absorption of incident photons, the photo-generated charge carriers result in an increase of the conductivity of the material. Since there is no internal electric field, electric field should be built by external reverse bias to collect photo-generated carriers before they recombine. The current measured through the photoconductor indicates the illumination level of the material; hence the output is expected to be linearly proportional to the input optical power. However, since large bias is required and their current levels are much higher, photoconductive detectors are not suitable for dense FPAs even though they provide high responsivity. The basic structure of a photoconductor is shown in Figure 1.7.

In extrinsic detectors, the excitation occurs at an impurity center. The energy level of the doped impurities determines the detection wavelength. Since the requirement energy to excite carriers from impurity level to the bottom of conduction or top of valance band is smaller than the intrinsic ones, the detection wavelength is larger. The typical operating wavelength is larger than 20 μm, which is in the very longwave infrared band. For extrinsic detectors, Si:As and Si:Ga are widely used. The level of the need for cooling is the main difference between extrinsic and intrinsic detectors. Extrinsic detectors need cooling down to very low temperatures (even below cryogenic temperatures) to achieve high sensitivity in contrast to intrinsic detectors.
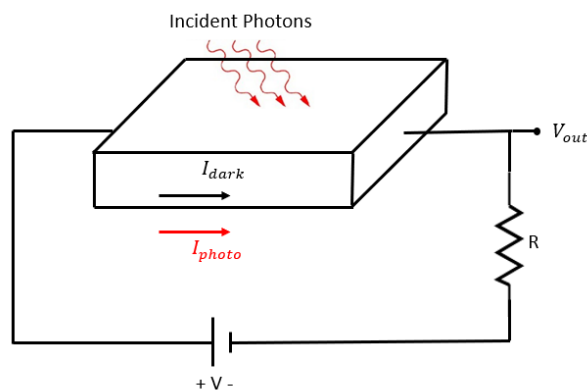
Figure 1.7. Basic structure of a photoconductor.

Another type of photon detector is the quantum structured detector. A multi quantum well layer structure used as a detector is called a QWIP, quantum well infrared photodetector. Quantum wells are constructed with the narrower bandgap material such as GaAs encapsulated by wider bandgap materials such as AlGaAs. The transitions in this type of detector can be in three different ways, bound to bound, bound to quasi-bound and bound to continuum. Even though QWIP is a photoconductor, it provides high detector impedance, low power consumption and fast response time [1]. Hence, it is applicable for large format FPAs. The drawback of QWIP is that QWIP devices are not capable of normal incident light absorption without any grating layer. Quantum dot infrared detectors (QDIP), differ from QWIPs in the sense that the quantum wells replaced by quantum dots. QDIPs are formed by the deposition of a layer of dots, typically with diameters on the order of nanometers on a well material. The detection mechanism of quantum structures depends on the intraband photoexcitation of electrons from confined states. The most promising property of QDIPs is the possibility of absorption of incident light normal to the growth direction unlike QWIPs. Hence, there is no need to fabricate a grating which may cause difficulties in process steps [11]. In addition to the capability of normal incident absorption, the dark current is expected to be lower in QDIPs resulting in higher detectivities due to the confinement in all three directions. However, due to difficulties in growth and fabrication technologies, QDIPs do not show their theoretical success in practical applications yet.

Type II strained super-lattice, SLS, is a structure constructed by repeating thin layers sequence of different materials. The hole and electron levels are separated, and transitions occur where the overlap occurs between wave function of the carriers. In order to absorb the incident radiation properly, the layers should be extremely thin.

In photovoltaic devices, the minority carriers are responsible for detection. The photo-generated charge carriers, holes and electrons, are separated by internal potential barrier which builds an electric field. The separated charge carriers move in opposite directions due to electric field. P-n homo- and hetero-junctions, metal-insulator-

semiconductor (MIS) photo-capacitors and Schottky barriers have potential barriers. The most widely used configuration of photovoltaic detector is a photodiode, which is simply a p-n junction [10]. Since there is already electric field due to separation of majority carriers, there is no need for large reverse bias to collect electrons and holes. Electron-hole pairs are excited with the incident radiation, they diffuse toward p-n junction, and they are swept by the built-in electric field to opposite directions resulting in photocurrent. The photo-generated carriers lead to a photocurrent proportional to the quantum efficiency of the material. The structure and the current voltage characteristic of a photodiode are illustrated in Figure 1.8.
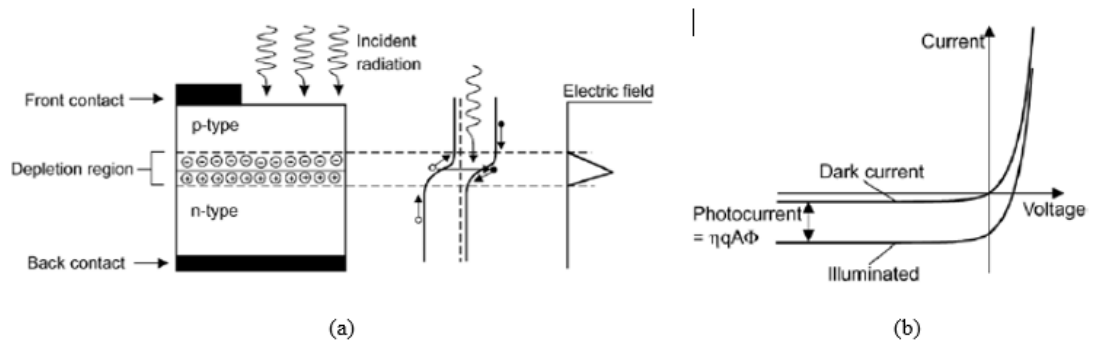
Figure 1.8. The p-n junction with depletion region and electric field distribution and (b) I-V characteristic of a photovoltaic p-n diode [12].

1.4. Comparison of Thermal and Photon Detectors

Thermal detectors have no wavelength dependence since the nature of the incoming photons does not affect the output as long as the incoming photon has an energy which can excite electrons. Hence, they exhibit a flat spectral response which is not proportional to energy of incoming photons as long as they can be absorbed. On the other hand, the response of photon detectors depends on wavelength. Since the photon energy (and the radiation power falling on the detector) decreases with increasing photon wavelength, the spectral responsivity shows a linear increase with increasing wavelength, until the photon energy falls below the bandgap. The cut-off wavelength indicates the wavelength at which the responsivity falls to half of the peak responsivity

[6]. The relative spectral response characteristics of thermal and photon detectors are given in Figure 1.9.

Thermal detectors such as bolometers are better than photon detectors for applications which high sensitivity and speed are not prior for detection, due to their low cost, no need for cooling and ease to use. However, high sensitivity and fast response can only be achieved by photoconductor, photovoltaic or QWIP detectors which need cooling.
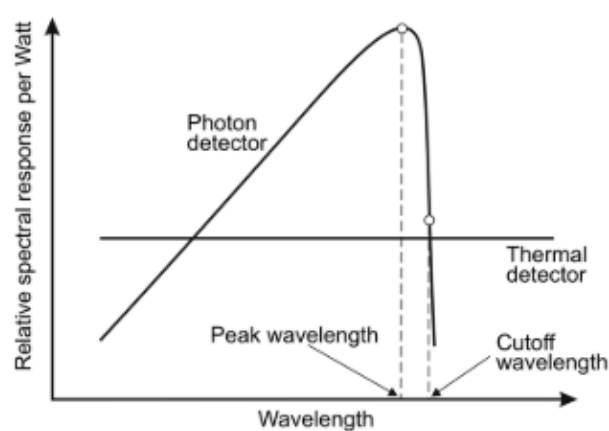
Figure 1.9. Relative spectral response of thermal and photon detectors [6].

The most important parameter to characterize the detector is detectivity. The photovoltaic detectors have higher specific detectivity than both photoconductors and thermal detectors. The comparison of the detectivity of the state-of-art infrared sensors are shown in Figure 1.10 [13], [14].
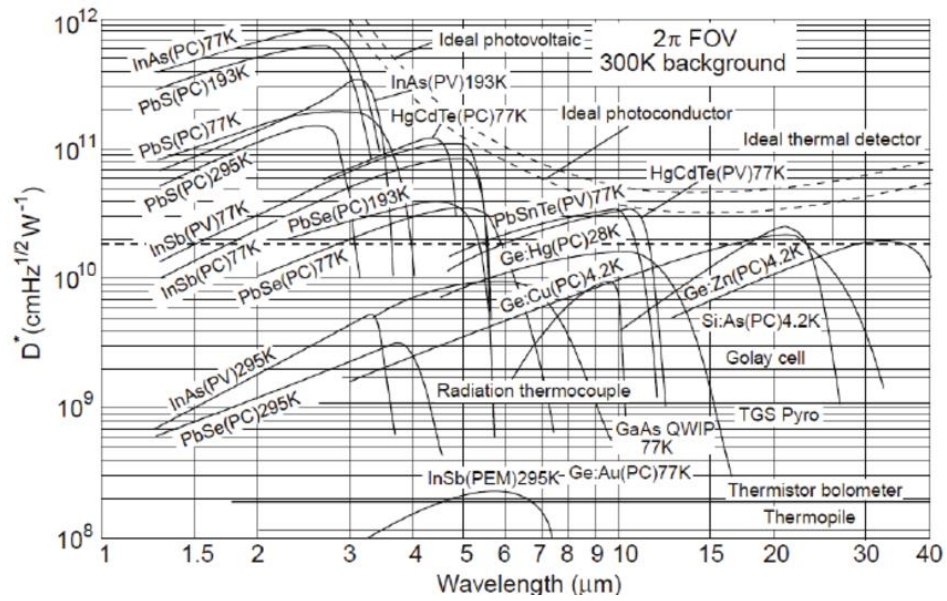
Figure 1.10. The theoretical curves for specific detectivity for ideal photon and thermal detectors [10].

Short introduction to infrared sensors including basic principles of infrared radiation, figures of merit for infrared detectors, classification of IR detectors and comparison of them are given in this chapter. In the next chapter, history of $Hg_{1-x}Cd_xTe$ detectors and the state of the art HgCdTe detector technology will be summarized.

CHAPTER 2

MERCURY CADMIUM TELLURIDE
INFRARED DETECTORS AND FOCAL PLANE ARRAYS

$Hg_{1-x}Cd_xTe$ (mercury cadmium telluride, HgCdTe) is an alloy of HgTe (mercury telluride) and CdTe (cadmium telluride). Nowadays, HgCdTe is the most widely used infrared detector material for photon sensors operating in the SWIR, MWIR and LWIR bands [15].

2.1. History of HgCdTe

The first study on HgCdTe was reported in 1958 and 1959 by Lawson and colleagues. They recognized that the bandgap of the material changed continuously from the bandgap value of HgTe to that of CdTe by changing the mole fractions of CdTe and HgTe in the alloy. Discovering of variable bandgap of HgCdTe alloy indicated that HgCdTe can be used in a lot of applications of infrared radiation, both for IR sensing and imaging over a wide spectral range [16].

Three generations of infrared detector devices can be seen in the development of HgCdTe detectors namely the first, the second and the third generations. Photoconductive arrays were the first generation of devices, and they were built in the US as early as 1964 after developing Bridgman crystal growth technique. In the 1970s, the high-performance mid-wave and long-wave sensing linear arrays were developed by using n type photoconductors. In 1969, Bartlett and colleagues reported background limited performance in the longwave infrared region for photoconductors operated at cryogenic temperature. The first generation HgCdTe devices are still in use for many applications such as carbon dioxide detection, FTIR spectroscopy, missile guidance, etc. The second generation of devices consists of photovoltaic two-dimensional arrays and their production rate is high. Verie and Granger published the

first intentionally formed junction for HgCdTe photodiode by using Hg vacancy doped material [12]. The third generation consists of two-color detectors and avalanche photodiodes. With respect to other generations, the third generation provides better thermal resolution and higher frame rates as well as multicolor functionality with higher number of pixels [17]. The technical developments such as dry etching for reducing pixel pitch and advanced readout concepts were necessary to develop the third generation devices. An evolution timeline of HgCdTe IR detectors can be seen in Figure 2.1.
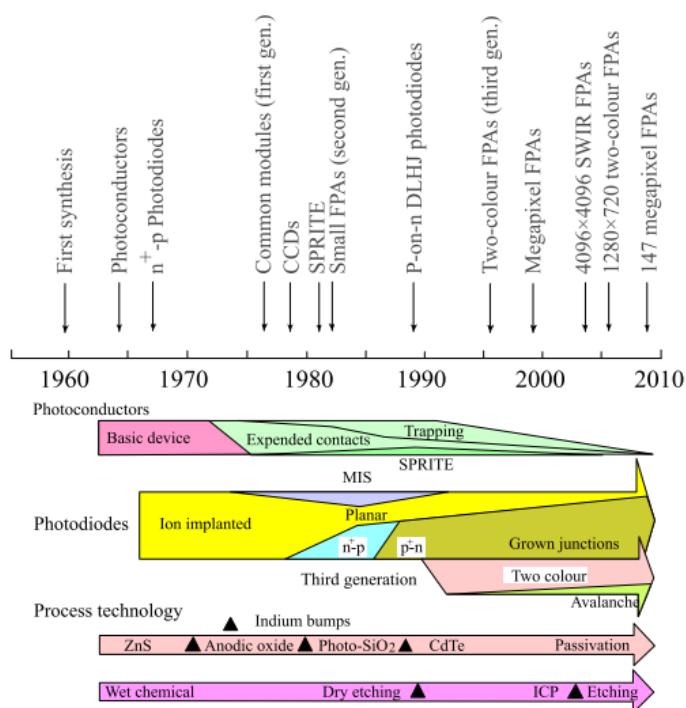
Figure 2.1. History of development of HgCdTe detectors [17].

2.2. Material Properties of HgCdTe

HgCdTe ternary alloy is an ideal detector material, and it has structure of the zinc blende semiconductor. Two key features of HgCdTe can be listed as follows: arrangeable energy bandgap for detection in the 1-30 μm wavelength range and direct bandgap with high absorption coefficient. Besides, variation of lattice constant with composition is very small which enables growing graded gap structures and high-

20

quality hetero-layers. These advantages allow the usage of HgCdTe for detectors operated as both photodiode and photoconductor structures. In the following sections, some material properties of HgCdTe will be described.

2.2.1. Lattice Parameter

One of the several properties of HgCdTe qualifying it as highly useful material for infrared detection is the availability of a lattice matched, wide bandgap substrate (CdZnTe) for epitaxial growth. The crystal and surface quality are significantly affected by the substrate-epitaxial layer lattice constant mismatch. As seen from Figure 2.2 the lattice constants of HgTe and CdTe are very similar, which are 6.481 Å and 6.461 Å at room temperature, respectively. The lattice mismatch between HgTe and CdTe in the HgCdTe alloy is negligible [18].
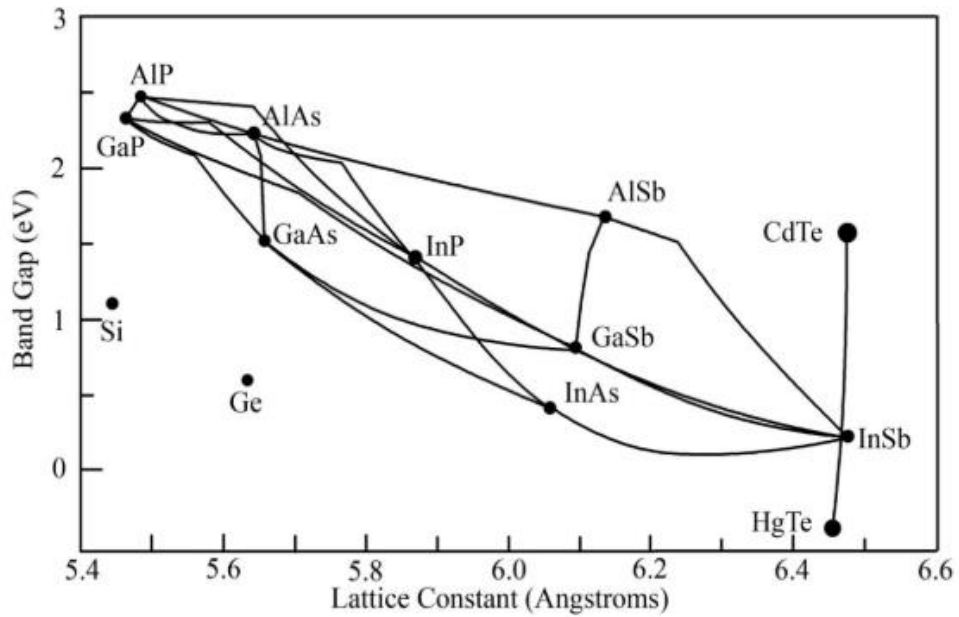
Figure 2.2. Lattice constant vs. bandgap of some semiconductor materials [18].

The variation of lattice constant, a, at room temperature with respect to cadmium composition, x, was expressed by Higgins *et al.* [19] as

$$a(x) = 6.4614 + 0.0084x + 0.0168x^2 - 0.0057x^3 \ (\text{Å}) \qquad (2.1)$$

21

where x is the mole fraction of Cd. As can be seen from Figure 2.3, the lattice constant is changed by only 0.015% between MWIR and LWIR infrared bands, corresponding to the Cd mole fractions of 0.3 and 0.2, respectively. This explains why HgCdTe is not the only suitable material for the entire infrared band but is also the most preferred semiconductor for dual-band structures.
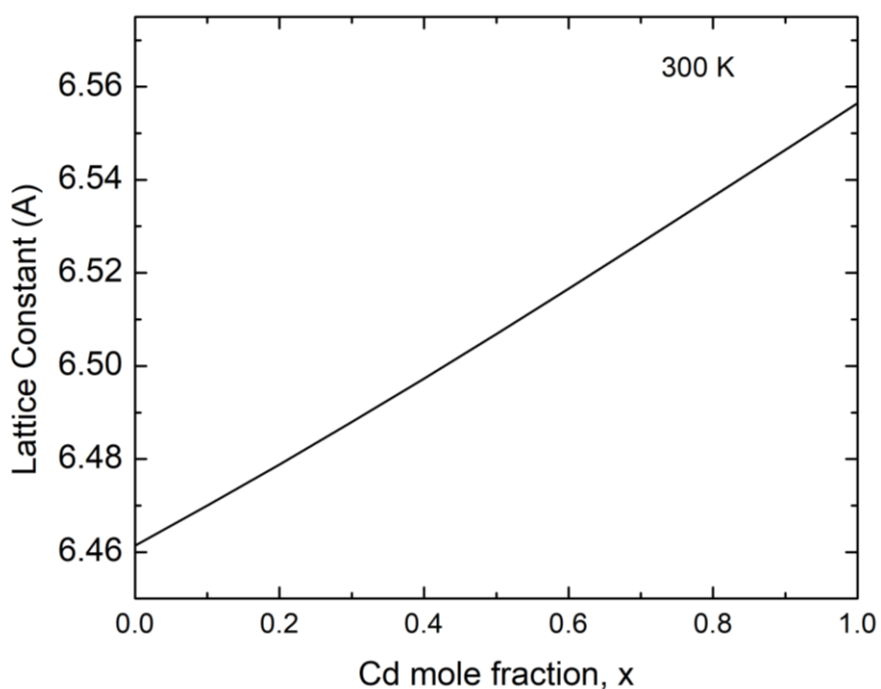
Figure 2.3. Lattice parameter of Hg₁₋ₓCdₓTe at room temperature.

The lattice constant also depends on temperature. The relationship between the lattice constant and temperature can be expressed as follows [19]

$$a(T) = a(300\ K) + B(T)\ \left(\text{Å}\right) \qquad (2.2)$$

where $a(300\ K)$ is the lattice parameter at room temperature. In Table 2.1, values for B(T) are given. In Figure 2.4, the lattice constant of HgCdTe for different Cd mole fractions with respect to temperature is shown.

Table 2.1. Lattice parameter correction factor B(T) for different temperatures.

T(K)	100	200	300	400	500	600	700	800
B(T)	-0.007	-0.004	0	0.003	0.006	0.01	0.014	0.019
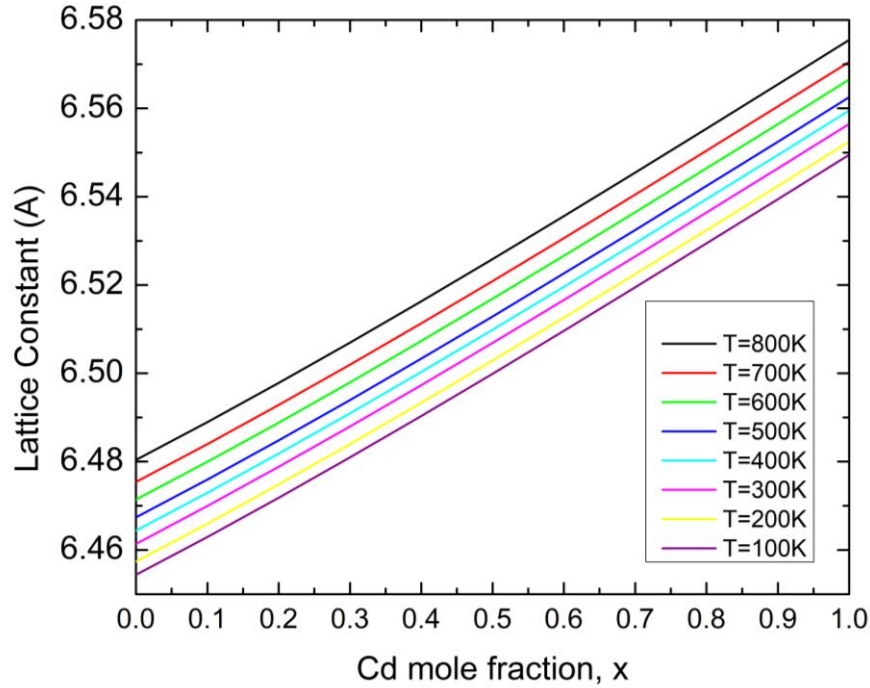
Figure 2.4. Lattice parameter of $Hg_{1-x}Cd_xTe$ as a function of temperature.

2.2.2. Energy Bandgap

HgCdTe has a direct energy bandgap, and its value changes with respect to mole fraction of Cd. CdTe is a semiconductor with 1.6088 eV energy bandgap, whereas the energy bandgap of HgTe is -0.2608 eV, which means the conduction band edge lies below the valance band edge. Hence, the bandgap of HgCdTe is between the energy bandgap values of HgTe and CdTe. CdTe and HgTe are fully miscible for the range of mole fraction from 0 to 1. As the mole fraction x is decreased, the energy bandgap value approaches to zero. The value of energy bandgap depends on both mole fraction and temperature. There are different expressions predicting the energy bandgap in literature. The most commonly used expression is stated by Hansen *et al*. [12]

$$E_g(x,T) = -0.302 + 1.93x - 0.81x^2 + 0.832x^3 + 5.35 \times 10^{-4}(1 - 2x)T \qquad (2.3)$$

where T is in kelvin, E_g is the energy bandgap in eV and x is the mole fraction. Equation (2.3) was obtained by fitting values measured for $x < 0.4$ [20]. In Figure 2.5, the energy bandgap of HgCdTe for CdTe mole fractions between 0.18 and 0.4 are given for room temperature and 77K with respect to Equation (2.3).
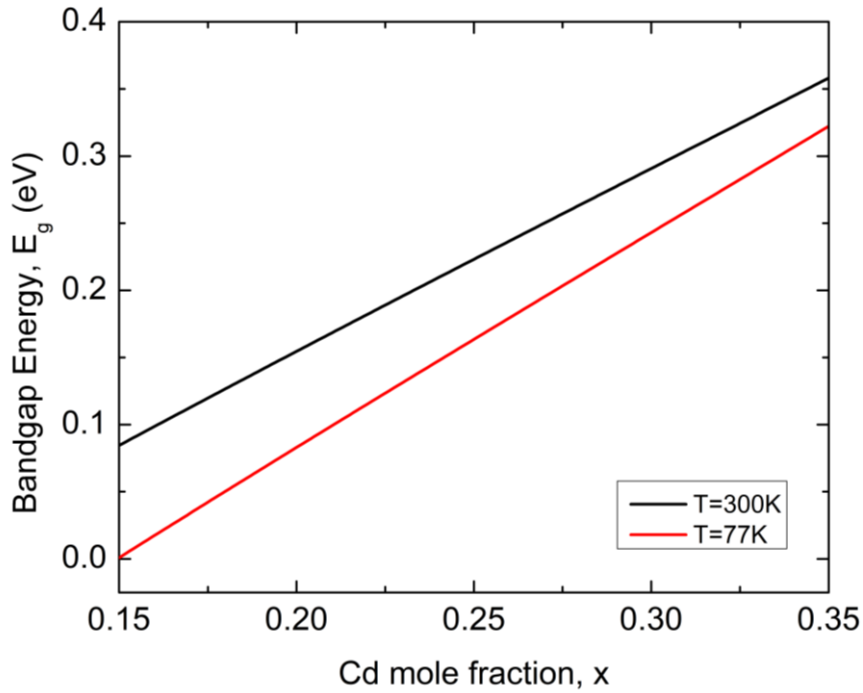
Figure 2.5. Bandgap energy of Hg$_{1-x}$Cd$_x$Te for 77 K and 300 K.

Cut-off wavelength of a material can be expressed as follows

$$\lambda_{cut-off} = \frac{1.24}{E_g} \qquad (2.4)$$

where $\lambda_{cut-off}$ is the cut-off wavelength in μm and E_g is the energy bandgap in eV. In Figure 2.6, the HgCdTe cut-off wavelength with respect to mole fraction is given for room temperature and 77 K.

By controlling the x value, energy bandgap of Hg$_{1-x}$Cd$_x$Te can be adjusted from 0.7 μm (x≈1) to 25 μm (x≈0.18 at 77 K). As the cut-off wavelength increases, the energy

24

bandgap starts to depend on cadmium mole fraction more strongly. For high cut-off wavelengths, small variation in the x value results in significant nonuniformity with respect to LWIR, MWIR and SWIR bands. Therefore, very large format VLWIR FPAs are more challenging.
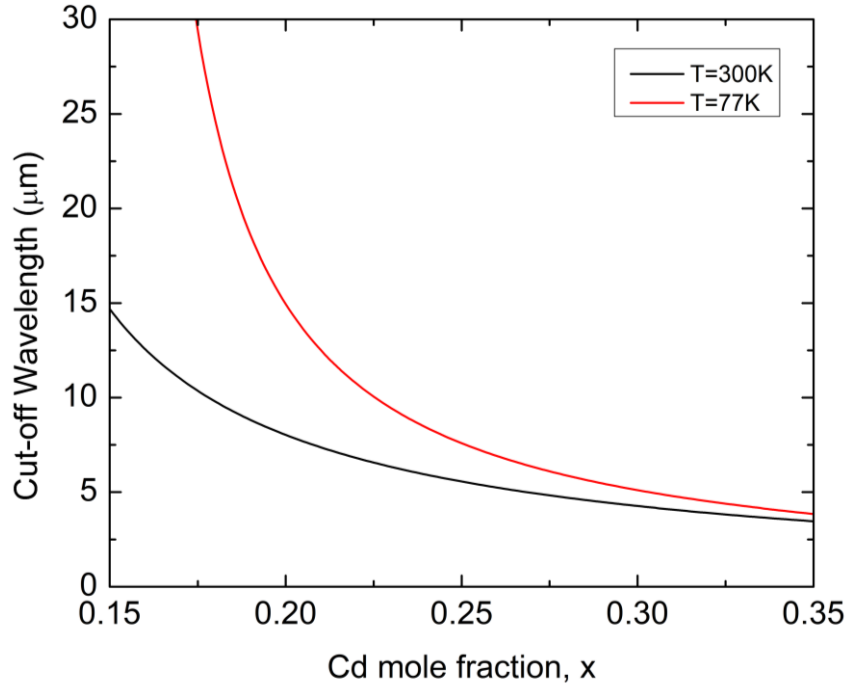
Figure 2.6. Cut-off wavelength of Hg$_{1-x}$Cd$_x$Te for 77 K and 300 K.

2.2.3. Intrinsic Carrier Concentration

The intrinsic carrier concentration *n$_i$ (cm^{-3})* of HgCdTe is given by the well-known expression by Hansen and Schmit [22]

$$n_i = (5.585 - 3.82x + 0.001253T - 0.001364xT) \times 10^{14} E_g^{\frac{3}{4}} T^{\frac{3}{2}} e^{\left(-\frac{E_g}{2kT}\right)} \qquad (2.5)$$

where x is the cadmium mole fraction, E_g is the energy bandgap in eV, and *k* is the Boltzmann constant in eV-K^{-1}. Equation (2.5) is valid for compositions x lying between 0.16 and 0.4. Intrinsic carrier concentration for different temperatures is plotted in Figure 2.7.
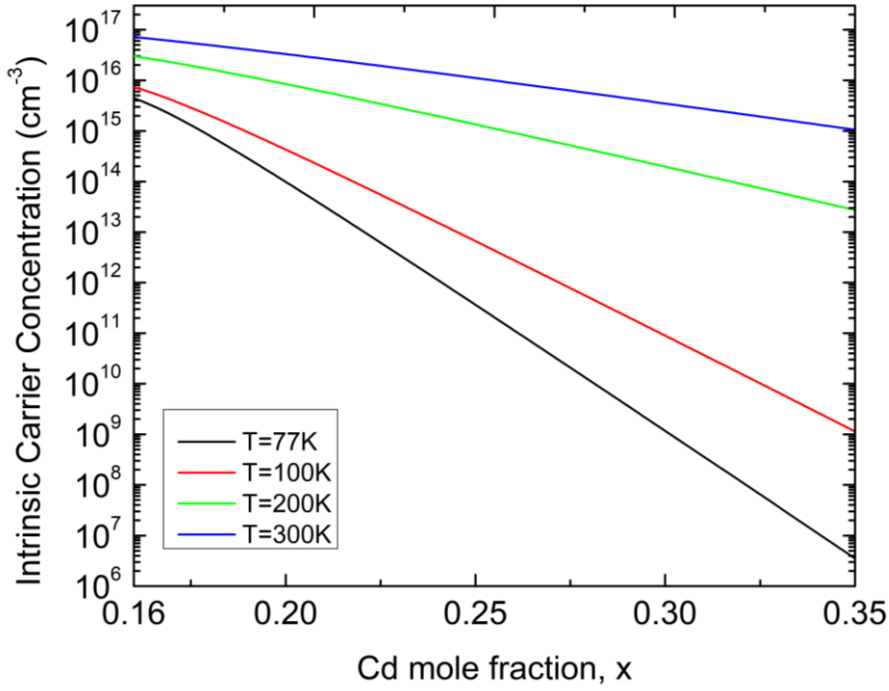
Figure 2.7. Intrinsic carrier concentration of Hg₁₋ₓCdₓTe versus x for different temperatures.

2.2.4. Mobility

Carrier lifetime and concentration are affected by the carrier mobility which is one of the most dominant parameters affecting the detector performance. Mobility of the material depends on both composition and temperature. In n-type HgCdTe, ionized impurity, acoustic phonon and optical phonon scattering are dominant scattering processes [23].

Due to the much larger hole effective mass ratio, the electron mobility in HgCdTe is roughly two orders higher than the hole mobility. The effective mass values can be calculated using the expression established by Weiler [24]

$$\frac{m}{m_e{}^*} = 1 + 2F + \frac{E_p}{3}\left(\frac{2}{E_g + \dfrac{1}{E_g + \Delta}}\right) \tag{2.6}$$

where E_p=19 eV, F =-0.8 and Δ=1 eV.

26

An expression for Hg$_{1-x}$Cd$_x$Te electron mobility in the Cadmium mole fraction range 0.2-0.6 and for T>50 K has been given by Rosbeck by fitting the Hall data [25]

$$\mu_e = \frac{9 \times 10^8 b}{T^{2a}}, \quad where \quad a = \left(\frac{0.2}{x}\right)^{0.6} \quad , \quad b = \left(\frac{0.2}{x}\right)^{7.5} \qquad (2.7)$$

where T is temperature in Kelvin. In Figure 2.8, this expression is plotted versus temperature with different x values. The electron mobility of HgCdTe in the above x range is in the order of 10^4-10^5 cm^2/(V-s) at 77 K. The hole mobility can be estimated to be 0.01 times the electron mobility [12].
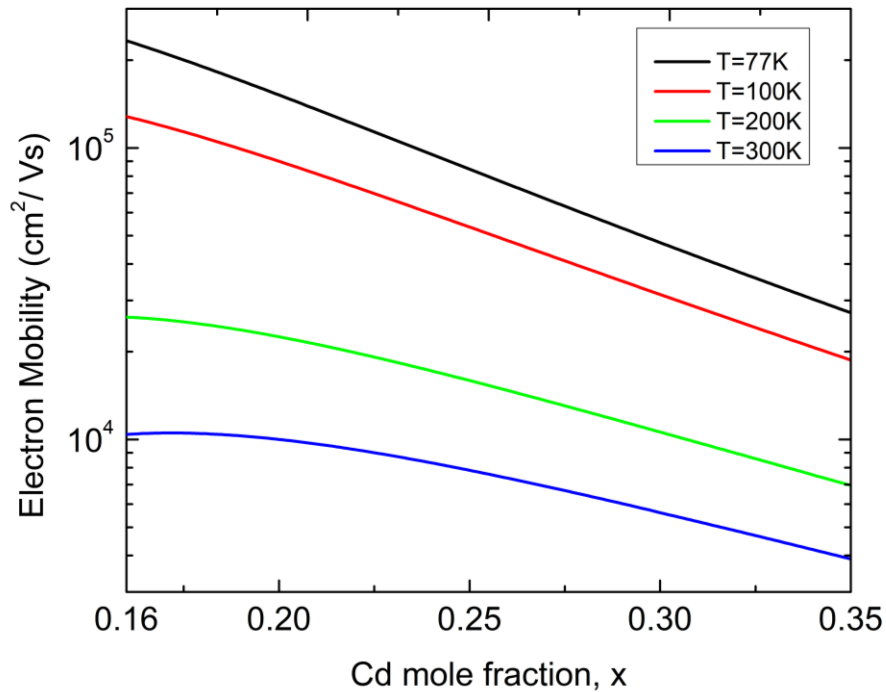
Figure 2.8. Electron mobility of Hg$_{1-x}$Cd$_x$Te for different temperatures.

2.2.5. Thermal Generation-Recombination Processes

Steady-state concentration of carriers is determined by generation-recombination mechanisms in semiconductors. By the generation-recombination processes' nature, fluctuations in carrier concentration occur, and these fluctuations cause noise that determines the upper limit of photodetector performance. While the effect of

recombination rates may be minimized by arranging where the recombination processes take place, the generation processes associated with fluctuations cannot be avoided. Hence, minority carrier lifetimes resulting from generation-recombination mechanisms establish one of the most significant material properties governing the performance parameters of detectors such as dark current, responsivity and quantum efficiency.

Electron-hole pairs can recombine in two different ways, either an electron can drop directly from conduction band to the valance which is direct recombination or indirect recombination occurs through the transition of an electron in the conduction band to an energy level (introduced by impurities and/or defects) in the bandgap followed by the capture of this level a hole from the valance band. Indirect recombination is also known as Shockley-Read-Hall (SRH) recombination.

The carrier lifetime in HgCdTe is determined by radiative, Auger and SRH recombination mechanisms shown in Figure 2.9. The radiative and Auger mechanisms are fundamental and intrinsic processes, whereas SRH recombination is extrinsic [26]. Beside these fundamental mechanisms, recombination at HgCdTe surface may also be dominant in the performance of HgCdTe detectors. Compared with the bulk, the interface at the surface contains higher defect density which results in fixed charges and interface traps leading to band-banding at the surface. For $Hg_{1-x}Cd_xTe$ having low x (0.2-0.3), the bandgap at 77 K changes between 0.1 and 0.25 eV. Hence, the band bending can be comparable with the bandgap energy, and the accumulation, depletion or inversion region can be easily formed at the surface [27]. The surface recombination velocity should be also used to determine the net lifetime of excess carriers. When carrier concentration is small, the lifetimes of different recombination mechanisms can be treated to be independent from each other, and the net recombination lifetime can be expressed as follows

$$\frac{1}{\tau_{eff}} = \frac{1}{\tau_{Radiative}} + \frac{1}{\tau_{Auger}} + \frac{1}{\tau_{SRH}} + \frac{2S}{d} \qquad (2.8)$$

28

where $\tau_{Radiative}$, τ_{Auger}, τ_{SRH} are the radiative, Auger and SRH lifetimes, respectively, S is the surface recombination velocity, and d is the thickness of the HgCdTe epitaxial layer.
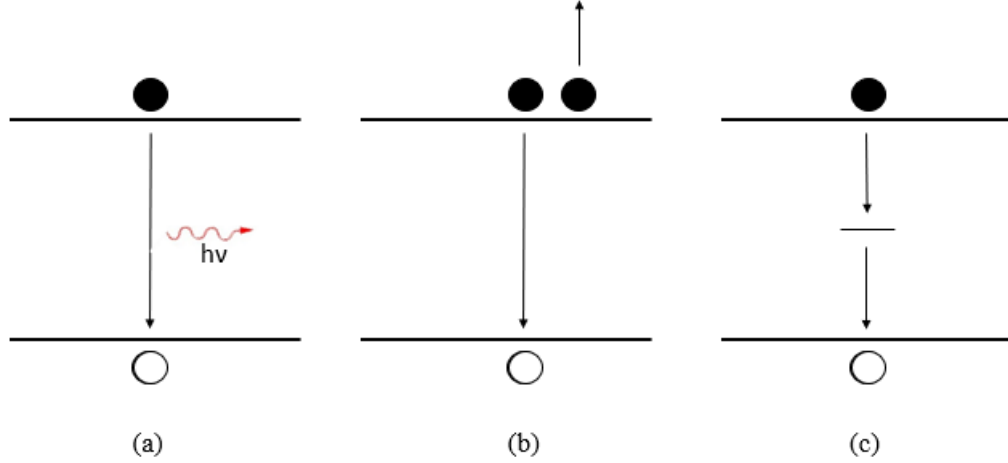
Figure 2.9. Dominant recombination mechanisms in narrow bandgap semiconductors: (a) radiative, (b) Auger and (c) SRH recombination.

2.2.5.1. Radiative Recombination

In radiative recombination mechanism, an electron from conduction band loses energy and recombines with a hole in the valance band. The energy which is lost in the recombination process is released as photon in a direct bandgap semiconductor such as HgCdTe. Radiative lifetime can be calculated as follows

$$\tau_R = \frac{n_i{}^2}{G_R(n_0 + p_0)} \tag{2.9}$$

where G_R is the generation rate (cm^{-3}-sec^{-1}), n_i is the intrinsic carrier concentration, and p_0 and n_0 are the hole and electron concentrations. G_R is expressed as follows:

$$G_R = 5.8 \times 10^{-13} n_i{}^2 \varepsilon_\infty{}^{\frac{1}{2}} \left(\frac{m}{m_e{}^* + m_h{}^*}\right)^{\frac{3}{2}} \left(1 + \frac{m}{m_e{}^*}\right) \left(\frac{300}{T}\right)^{\frac{3}{2}} \left(E_g{}^2 + 3kTE_g + 3.75k^2T^2\right) \tag{2.10}$$

where ε_∞ is the high frequency dielectric constant, m^* is the effective mass and m is the electron rest mass. It can be seem from Equation (2.10) that the radiative lifetime for intrinsic material changes with temperature as $\exp(E_g/kT)$. The radiative recombination process is illustrated in Figure 2.10.
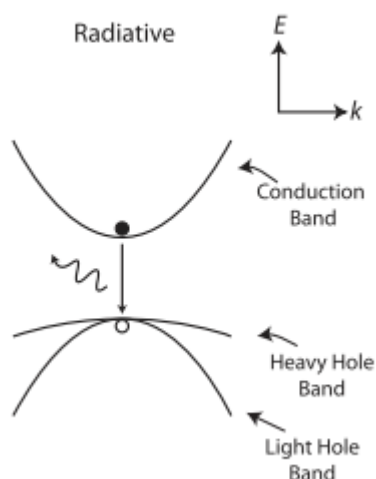
Figure 2.10. Radiative recombination mechanism [23].

2.2.5.2. Auger Recombination

Auger mechanism is another intrinsic recombination mechanism, and it becomes dominant in high-quality narrow gap semiconductors such as HgCdTe. In this mechanism, Coulomb interaction occurs between three particles (two electrons and one hole or two holes and one electron). Two of Auger recombination mechanisms have the lowest threshold energy and are denoted as Auger-1 and Auger-7 as shown in Figure 2.11.

Auger-1 mechanism dominates in n-type material which can be described as the Coulomb interaction of one hole and two electrons. An electron in conduction band recombines with a hole in the valance band and excess energy is transferred to another electron in the conduction band exciting the latter to a higher energy level. At moderate and high n-type doping levels, the Fermi level approaches the conduction band due to low density of states, hence the minimum energy which is required for the

Auger transition is increased. As a result, the suppression in Auger-1 processes can be achieved with highly doped n-type material [28]. Auger-1 lifetime is given by [29]

$$\tau_{A1} = \frac{2n_i^2}{n(n+p)}\tau_{A1}{}^i \tag{2.11}$$

where n_i is the intrinsic carrier concentration, n and p are the total electron and hole concentrations, respectively, and $\tau_{A1}{}^i$ is the intrinsic Auger-1 lifetime. The intrinsic Auger-1 lifetime is expressed as follows [29]

$$\tau_{A1}{}^i = \frac{3.8 \times 10^{-18}\varepsilon_\infty^2 \left(1 + \frac{m_e^*}{m_h^*}\right)^{\frac{1}{2}} \left(1 + 2\frac{m_e^*}{m_h^*}\right) exp\left(\frac{\left(1 + 2\frac{m_e^*}{m_h^*}\right)E_g}{\left(1 + \frac{m_e^*}{m_h^*}\right)kT}\right)}{\left(\frac{m_e^*}{m}\right)|F_1F_2|\left(\frac{kT}{E_g}\right)^{\frac{3}{2}}} \tag{2.12}$$

where $|F_1F_2|$ is the wave function overlap integral.

In p-type material Auger-7 is the dominant Auger mechanism, and in this process, the Coulomb interaction occurs between two holes and one electron. An electron in the conduction band recombines with a hole in the valance band, and another hole in the valance band is excited by excess energy into a higher energy state. Due to the higher density of states, heavy p-type doping does not have significant effect on the Auger-7 process [28]. Auger-7 lifetime is expressed by [29]

$$\tau_{A7} = \frac{2n_i^2}{p(n+p)}\tau_{A7}{}^i \tag{2.13}$$

where $\tau_{A7}{}^i$ is the intrinsic Auger-7 lifetime. The intrinsic Auger-7 lifetime is expressed in terms of intrinsic Auger-1 lifetime [29] as

$$\gamma = \frac{\tau_{A7}{}^i}{\tau_{A1}{}^i}. \tag{2.14}$$
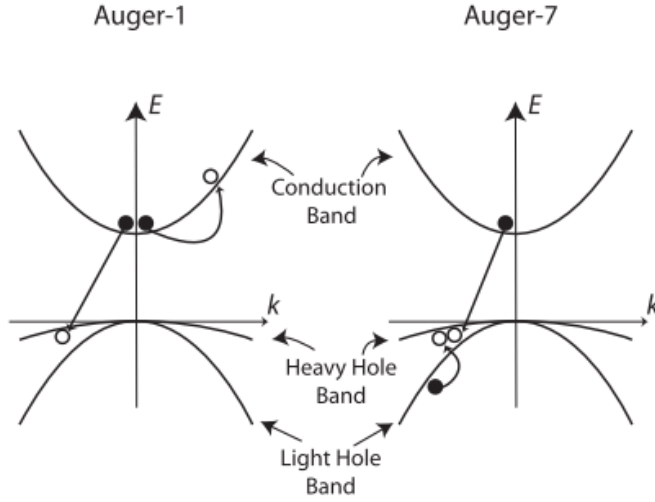
Figure 2.11. Two dominant mechanisms for Auger recombination in HgCdTe [23].

The above ratio is dependent on both temperature and Cadmium mole fraction, x. Casselman *et al.* [30] estimates this ratio as $3 \leq \gamma \leq 6$ in the x range of 0.16-0.4 for 50 K$\leq$T$\leq$300 K.

The net lifetime of the two dominant Auger processes is given by [29]

$$\tau_A = \frac{2\gamma\tau_{A7}{}^i}{1 + \gamma + \gamma\left(\dfrac{n}{n_i^2}\right) + \left(\dfrac{p}{n_i^2}\right)}. \tag{2.15}$$

2.2.5.3. Shockley-Read-Hall Mechanism

The Shockley-Read-Hall mechanism occurs due to defects and impurities which introduce recombination centers and traps located within the forbidden energy gap of the semiconductor. A single transition is defined by four different processes: electron emission, electron capture, hole emission and hole capture, which are illustrated in Figure 2.12. The lifetime due to SRH mechanism is expressed as [29]

$$\tau_{SRH} = \frac{\tau_{p0}(n + n_1 + \delta n) + \tau_{n0}(p + p_1 + \delta p)}{(n + p + \delta n)} \tag{2.16}$$

where δp and δn are the excess hole and electron concentrations. τ_{p0} and τ_{n0} (hole and electron SRH lifetimes) can be calculated using the following expressions

$$\tau_{n0} = \frac{1}{\sigma_n v_{tn} N_t} \quad and \quad \tau_{p0} = \frac{1}{\sigma_p v_{tp} N_t} \tag{2.17}$$

where σ_n and σ_p are the capture cross sections, v_{tn} and v_{tp} are the thermal velocities for electrons and holes, and N_t is the SRH center density.

For $\delta n = \delta p$, n_1 and p_1 are given by [23]

$$n_1 = N_c \, exp\left(\frac{E_t - E_c}{kT}\right) \quad and \quad p_1 = N_v \, exp\left(\frac{E_v - E_t}{kT}\right) \tag{2.18}$$

where N_c and N_v are the effective density of states for conduction and the valance bands, respectively.
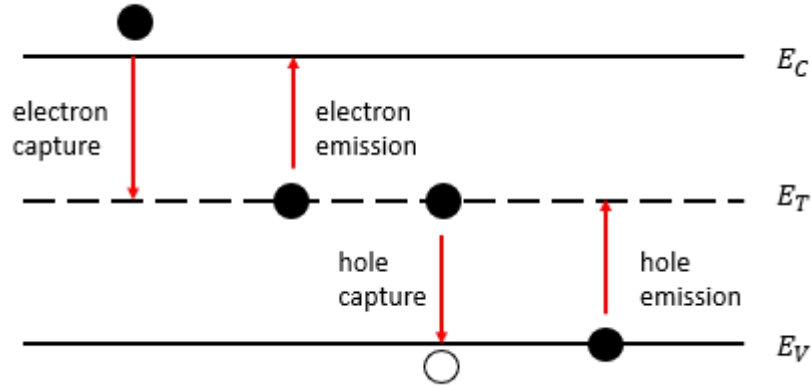
Figure 2.12. Shockley-Read-Hall mechanisms.

The recombination rate is maximized as trap level energy approaches the mid-gap. Hence, the most critical recombination centers are located at the middle of the bandgap. For this case, the net generation rate due to SRH states is given as [29]

$$(G - R)_{SRH} = \left(n_i^2 - n_0 p_0\right)\left[\tau_{p0}\left(n + n_i \, exp\left(\frac{E_t}{kT}\right)\right) + \tau_{n0}\left(p + n_i \, exp\left(\frac{-E_t}{kT}\right)\right)\right]^{-1}. \tag{2.19}$$

2.2.5.4. Surface Effects

The effective lifetime of HgCdTe detectors is strongly influenced by the properties of their surfaces and interfaces. Due to the weak bonding of Hg in the lattice, HgCdTe surface is very sensitive to physical and chemical treatments. Any wet etching and passivation deposition can lead to surface damage or change in stoichiometry. These imperfections create surface states which also generate and recombine carriers. Possible charge centers for a semiconductors surface are illustrated in Figure 2.13.
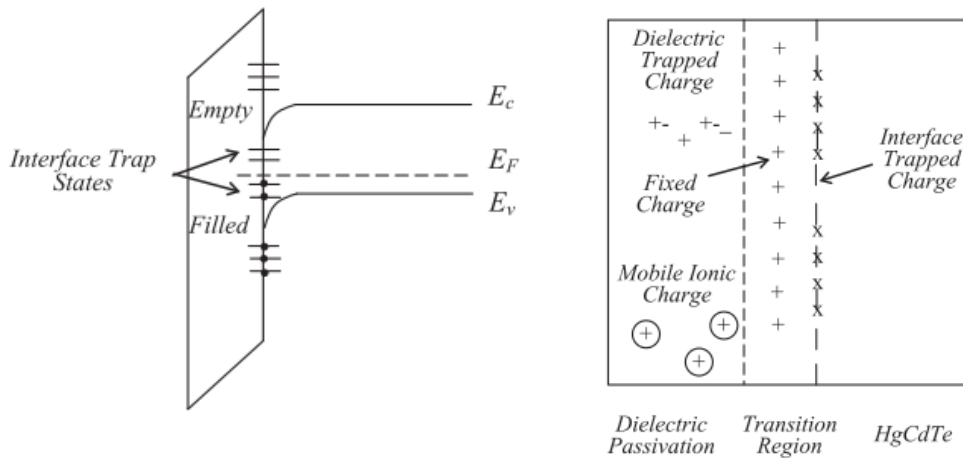
Figure 2.13. Interface states and surface band-bending [27].

The surface recombination velocity is characterized by the rate of recombination at the surface of the semiconductor and is expressed as follows [23]

$$S = \frac{kTD_{it}}{q} = \frac{\sqrt{C_n C_p}(n_0 + p_0)}{2n_i \left[cosh\left(\frac{E_t - E_i}{kT - u_0}\right) + cosh\left(\frac{q\phi_s + E_t - E_i}{kT - u_0}\right) \right]} \qquad (2.20)$$

where D_{it} is the interface trap density, and ϕ_s is the surface potential. The parameter, u_0 is given by [23]

$$u_0 = ln\left(\frac{C_n}{C_p}\right) \qquad (2.21)$$

where C_n and C_p are the parameters related to the probability of electron and hole capture by a defect state, respectively.

2.2.6. Diffusion Length

One of the main advantages of HgCdTe is that the high-quality material has long diffusion length. Diffusion length is defined as the mean distance a carrier may diffuse through material before recombination. Ideally, the absorption layer thickness should be within a diffusion length of the semiconductor material to minimize recombination. It is closely related to the excess carrier lifetime of a material, and it is expressed as [23]

$$L_{e,h} = \sqrt{\tau_{e,h} D_{e,h}} \qquad (2.22)$$

where $\tau_{e,h}$ (s) is the minority electron or hole lifetime, $L_{e,h}$ (cm) is the minority electron or hole diffusion length, and. $D_{e,h}$ $(cm^2 s^{-1})$ is the diffusion coefficient of electrons or holes related with carrier mobilities through Einstein's relation which is given as [23]

$$D_{e,h} = \frac{kT}{q} \mu_{e,h}. \qquad (2.23)$$

In Table 2.2, the typical material properties of n-type HgCdTe for alloy compositions suitable in both LWIR and MWIR bands for low carrier concentration are given [19].

Table 2.2. Properties of n-type HgCdTe.

Waveband (μm)	Operating Temperature (K)	Lifetime (μs)	Hole Mobility $(cm^2 V^{-1} s^{-1})$	Diffusion Constant $(cm^2 s^{-1})$	Diffusion Length (μm)
8-14	80	2-5	480	3.2	25
3-5	230	15-30	100	2	5

2.2.7. Optical Properties

Since the optimum layer thickness and optical transmittance percentage should be taken into consideration for epitaxial layer design, the absorption coefficient and refractive index are important parameters.

2.2.7.1. Absorption Coefficient

In optical absorption, electrons from the valance band are excited to the conduction band, which is called the direct transition. Absorption coefficient is a measure of the semiconductor's ability to absorb incident radiation, and it is used for optimization of layer thicknesses of material so as to provide maximum absorption while minimizing the generated thermal noise. Since HgCdTe is a direct bandgap material, its optical absorption characteristic is very sharp. Figure 2.14 shows the optical coefficients for different x values and different photon energies. In order to obtain near unity quantum efficiency and low dark current, the absorber thickness should be slightly higher than the inverse absorption coefficient. Hence, 10-20 μm thick layer of $Hg_{1-x}Cd_xTe$ is sufficient for high quantum efficiency.
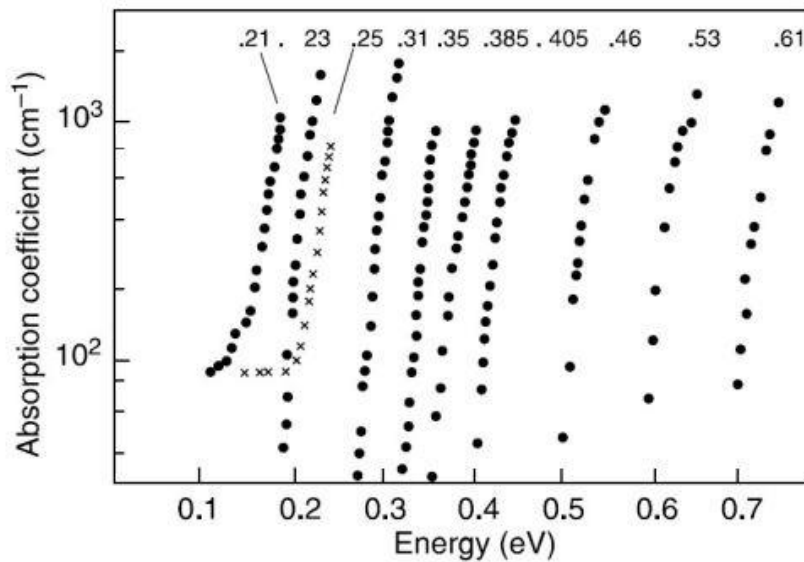
Figure 2.14. Optical absorption coefficient for $Hg_{1-x}Cd_xTe$ for different x values and photon energies at room temperature [31].

2.2.7.2. Refractive Index

The dependence of refractive index on temperature is usually estimated by using the Kramers and Kronig interrelations. For $Hg_{1-x}Cd_xTe$ with cadmium mole fraction from 0.276 to 0.540 and for temperature range 4.2 to 300 K, the following relation can be used [29]

$$n^2(\lambda, T) = A + \frac{B}{1 - \left(\frac{C}{\lambda}\right)^2} + D\lambda^2 \qquad (2.24)$$

where A, B, C and D are fitting parameters which depend on both cadmium mole fraction and temperature. They are expressed as follows [29]

$$A = 13.173 - 9.852x + 2.909x^2 + 10^{-3}(300 - T)$$
$$B = 0.83 - 0.246x + 0.0961x^2 + 8 \times 10^{-4}(300 - T)$$
$$C = 6.706 - 14.437x + 8.531x^2 + 7 \times 10^{-4}(300 - T) \qquad (2.25)$$
$$D = 1.953 \times 10^{-4} - 0.00128x + 1.853 \times 10^{-4}x^2 \,.$$

2.3. HgCdTe Focal Plane Arrays

It can be expected that p type absorber yields a significantly longer minority carrier diffusion length due to the much larger electron mobility. However, the minority carrier recombination lifetime is another parameter affecting the diffusion length, and this parameter depends strongly on the structural and electrical characteristics of the material. Theoretically, the highest performance photodiode is achieved with lightly doped p type absorber and a degenerate or wide gap n type cap layer. However, in 1985, Rogalski and Larkowski reported that the diffusion limited R_0A of n^+ - p detector is lower than for p^+ - n detector with a thick n type absorber [32]. The experimental results also support the indication of Rogalski and Larkowski. The most important advantages of p-on-n structure are that the control of n-type HgCdTe carrier concentration is easier in the range of $10^{14} - 10^{15} \, cm^{-3}$ by using extrinsic doping, while in p type absorber, control of carrier concentration at low levels is difficult [33].

Besides, the p type epilayers have limitations such as those occurring at the contacts and surfaces, as well as the SRH processes.

The homojunctions or heterojunctions of HgCdTe photodiodes have many configurations including mesa, planar and lateral n-p, n^+-n-p, p-n and n^+-p (p-n stands for a thick p-type layer as an absorber with a thin n-type surface layer, n^+ stands for highly doped n-type layer). The most widely utilized HgCdTe detector structures are backside illuminated planar and mesa structures which are illustrated in Figure 2.15. For the planar structure, either In-doped n-type epilayer implanted by p-type dopant arsenic (As) or p-type epilayer implanted by n-type dopant boron (B) are used. In the latter, p-type epilayer is constructed either by Hg vacancy or As-doping.

Procedure of processing of a planar device includes p-n junction formation by ion implantation and depositions of passivation and metal contact coating. On the other hand, mesa device structure usually consists of p-n junction formation by in-situ growth, mesa etching for isolation, passivation and metallization. Although process steps are easier, planar structures of HgCdTe may suffer from significant crosstalk between pixels and low pixel density due to high diffusion length of HgCdTe material. On the other hand, the mesa device structure can overcome high crosstalk problem. The pixels are etched down to absorption layer, and they are well isolated from each other. Hence, mesa structures are preferable to fabricate modern FPAs [15]. Near-ideal device performance can be obtained with both planar and mesa structures through the double layer heterojunction photodiode structure constructed on n type material. In this structure, the wider gap regions which have negligible contribution to thermally generated diffusion current are constructed to sandwich the narrow gap n type layer [33].
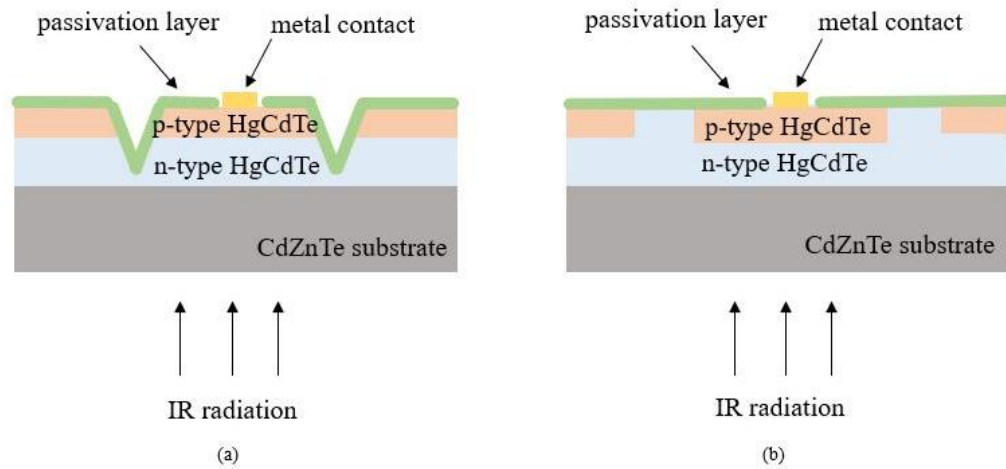
Figure 2.15. Schematic diagram of (a) mesa and (b) planar structure of p-on-n HgCdTe photodiodes.

There has been tremendous effort towards the development of MWIR and LWIR HgCdTe FPAs since the invention of HgCdTe. With the improvement of growth conditions and process studies, dual band detectors also became popular in recent years, and some successful results have been reported. In the following paragraphs, the studies on MWIR and LWIR second generation infrared detectors will be given.

In 2005, Chu *et. al.* [34] reported results of longwave infrared devices for both mesa and planar p-on-n heterojunction structures grown by liquid phase epitaxy (LPE). They fabricated 128x128 FPA with 10.8 μm cut-off wavelength and achieved NETD values as low as 16.42 mK with 98.7% operability.

Selex based in United Kingdom is one of the major HgCdTe FPA manufacturers. In 2006, they reported the results of p on n structure which was grown by metal organic vapor phase epitaxy (MOVPE) on GaAs. For 320x256/30 μm pitch with 10.0 μm cut-off wavelength at 77 K, mean NETD value was 25 mK with defected pixel percentage of 1.3 to 1.9%. Besides, they measured LW test arrays for different cut-off wavelengths, and compared R_0A values for various heterostructure designs. On a p on n heterostructure test array with 9.6 μm cut-off wavelength at 77 K, R_0A was measured as 800 Ω-cm^2 [35].

In 2008, Sizov *et. al.* [36] reported that the dark current of LWIR HgCdTe photodiodes with 11.6 μm cut-off wavelength was 5.3 nA at 77 K for $n^+ n^- p^+$ junction grown by molecular beam epitaxy (MBE) on Si substrate. 4x288 scanning array was fabricated and mean NETD≈9 mK was reached for 32° field of view with TDI function. However, substrate was not specified in this study.

BAE systems is an international defense, aerospace and security company which also works on HgCdTe FPAs. They recently developed back illuminated p on n heterojunction photodiode architecture, grown by two-layer LPE process. In 2009, they reported 1024x1024/19.5 μm pixel pitch FPA with 10.4 μm cut-off wavelength at 77 K exhibiting 99.4% operability [37].

In 2009, Mollard *et. al.* [38] CEA-LETI reviewed their results of planar MWIR and LWIR p-on-n photodiodes formed by arsenic implantation into an indium-doped base layer. 320x240/30 μm pixel pitch MWIR FPA with the cut-off wavelength of 5.1 μm was grown by MBE and characterized at 77 K. Mean NETD was 12 mK with an operability of 99.81%. The active layer of LWIR FPAs was grown by horizontal slider LPE. FPA was the same format with MWIR FPAs with the cut-off wavelength of 9.3 μm. Mean NETD was 29.8 mK with an operability of 99.64% under 14° field of view at 77 K.

AIM is a German company providing cooled HgCdTe based IR-modules form SWIR to VLWIR for nearly 40 years. In 2010, AIM reported their 640x512/15 μm pixel pitch LWIR FPA results. FPA was based on AIM's standard technology involving a backside illuminated planar structure on LPE HgCdTe layers grown on CdZnTe substrates. The p-type HgCdTe layers were doped by Hg vacancies, and p n junctions were performed by Boron ion implantation. The cut-off wavelength was 9.2 μm at 67 K. The mean NETD value was 37.2 mK with operability higher than 99.8% at 67 K for f/2.4 [39].

In 2011, SOFRADIR and CEA-LETI published their latest results on the development of MWIR and HOT MWIR HgCdTe FPAs. One of their products, 640x512/15 μm

pixel pitch namely LEO MW was optimized at operating temperature of 110 K. The cut-off wavelength was 5.3 μm at 80 K. The mean NETD value was 18 mK with operability over 99.5% with f/5.5 optics. After some technological improvements on standard n on p process, they introduced a new detector called LEO HOT which was MWIR 640x512/15 μm pixel pitch operating at temperatures up to 150 K with the cut-off wavelength 5 μm. The mean NETD value was below 20 mK up to 140 K with operability higher than 99.7% [40].

In 2013, Mollard *et al.* [41] from CEA-LETI reported their latest results for MWIR p-on-n HgCdTe detectors. A 640x512/15 μm pixel pitch FPA was fabricated with 5.3 μm cut-off wavelength at 80 K. The mean NETD value was 11.7 mK with 99.9% operability at 88 K. When the operating temperature was increased to 130 K, the mean NETD remained almost constant being below 11.8 mK with operability higher than 99.8%. These preliminary results yielded highly promising electrooptical performance for HOT MWIR detectors.

Ziegler, *et. al.* [42] reported large-format MWIR and LWIR FPAs developed at AIM in 2013. Liquid phase epitaxy (LPE) method was used to grow HgCdTe on CdZnTe for the fabrication of an n-on-p 1280x1024/15 μm pixel pitch FPA with 5.3 μm cut-off wavelength at 80 K. The mean NETD value was 17.8 mK with f/4 cold shield and the operability was 99.96%. Besides, the performance of FPA was evaluated at operating temperatures up to 130 K. The mean NETD value remained below 20 mK for temperatures smaller than 130 K, and increased to 22.5 mK at 130 K, whereas the operability was higher than 99.5% for all operating temperatures. LWIR 1280x1024/15 μm pixel pitch FPA with the cut-off wavelength of 8.8 μm at 80 K was also fabricated and characterized with f/2 cold shield. The mean NETD values was 30.4 mK with 99.81% operability at 71 K.

DEFIR, the joint laboratory between CEA-LETI and SOFRADIR has developed p on n photodiodes and focal plane arrays since 2005. They use p on n structure formed by arsenic implantation into an indium doped base layer. In 2014, they reported TV

format arrays with 15 μm pixel pitch and 8.95 μm cut-off wavelength. The mean NETD was 21 mK and the operability was 99.96% at 77 K under f/2 FOV. They also reported their p-on-n MWIR 640x512/15 μm pixel pitch FPA with cut-off wavelength of 5.3 μm at 80K. The mean NETD was around 12 mK with 99.90% operability at 88 K [43].

In 2015, AIM reported the results of LWIR 640x512/15 μm pitch FPA with cut-off wavelength 9.3 μm using LPE grown HgCdTe n on p structure. The overall operability of the FPA was ∼99.4% and NETD value was 23 mK with f/2.05 at ∼70 K [44]. The standard technology in AIM is n on p diode with the p type HgCdTe layer Hg vacancy doped. Nowadays, in order to decrease dark current and increase the working temperature, they started to study extrinsic doping for n on p technology. Besides, p on n planar detectors were manufactured in AIM with LPE grown HgCdTe on CdZnTe substrates (n-type material was In doped). The format was 640x512 with 20 μm pitch size. The dark current density of the detectors is compared to Rule 07 in Figure 2.16.
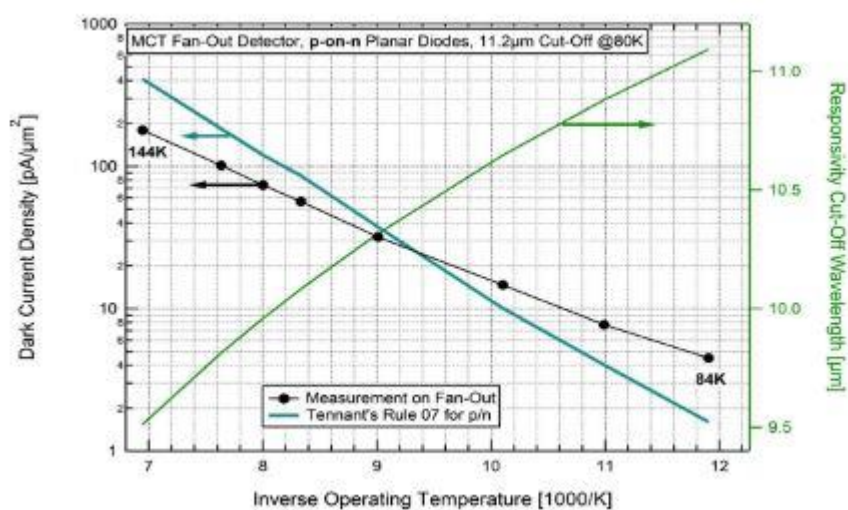
Figure 2.16. Dark current density for LWIR MCT p on n at AIM [44].

In 2015, CEA-LETI reported their planar p-on-n HgCdTe infrared local plane arrays operating in the LWIR band. FPAs were grown by liquid phase epitaxy (LPE) and p type doping was constructed by arsenic. For 320x256/30 μm pitch with 11.6 μm cut-off wavelength at 78 K, the mean NETD value was 36.2 mK with 99.9% operability.

The dark current density was evaluated as a function of 1000/T and the lowest dark current density of 8×10^{-13} A/cm^2 was obtained at 23 K. At working temperature of 78 K, the dark current density was measured as 8×10^{-5} A/cm^2 [45].

SOFRADIR is a French company producing cooled IR detectors for different applications such as military, security and space applications. They developed the HgCdTe technology based on an n on p structure for both MWIR and LWIR bands up to the last ten years. The last decade trend in SOFRADIR was the study of extrinsic p on n technology to meet the design requirements of small pixel pitch FPAs with higher operating temperature, operability and image quality. In 2015, they introduced a product namely DAPHNIS which was a 1024x768/10 μm pitch FPA with cut-off wavelength 5 μm developed by p on n homojunction planar technology. The dark current was characterized as diffusion limited, and the dark current density was 2 mA/cm^2 at 200 K. Mean NETD was 26 mK at 90 K with 99.8% operability under f/2 optics [46].

In 2016, AIM reported their longwave HgCdTe FPAs results involving both p on n and n on p planar photodiode technology. They measured dark current density of 0.1 pA/μm^2 on p on n test diodes with cut-off wavelength of 11.4 μm at 80 K. They reported an FPA with 512x320 format, 20 μm pitch and 11 μm cut-off wavelength at 80 K yielding a mean NETD value of 25 mK with only 0.45% defective pixels. On the other hand, they reported 0.2 pA/μm^2 dark current density for an n on p planar structure with cut-off wavelength 11.4 μm at 80 K. They did not see much difference between the dark current densities of p-on-n and n-on-p technologies for the same cut-off wavelength [47].

In 2016, Pere-Laperna *et. al.* [48] from SOFRADIR reported the results of their product DAPHNIS FPAs with 5.3 μm cut-off wavelength at 110 K having 10 μm pixel pitch and 1024x768 or 1280x720 format. LPE grown n-on-p (Hg vacancy doped) planar technology was used for FPA fabrication. The device was characterized under both f/2 and f/4 optics at different operating temperatures. From 90 K to 120 K, the

mean NETD value stayed constant equaling to 26 mK and 29 mK for f/2 and f/4, respectively. The operability was over 99.8% for f/2, and over 99.5% for f/4 up to 110 K.

In 2017, SOFRADIR reported LW Scorpio FPAs with cut-off wavelength of 9.3 μm, 640x512 format and 15 μm pixel pitch. Highest operating temperature with substantial performance was defined as 90 K. Quantum efficiency was above 70% for wavelengths shorter than 8.6 μm and NETD was 22 mK under f/2 optics [49].

Since 2000s, a considerable effort has been directed towards improving FPAs with multicolor capability in order to eliminate temporal registration and spatial alignment problems. The unit cell of integrated dual band focal plane arrays includes two collocated detectors which are sensitive to different spectral bands. Both simultaneous and sequential mode detectors can be fabricated from multilayer materials. Back illuminated back-to-back photodiode working as a bias selectable n-p-n is the simplest two-color HgCdTe detector, which is illustrated in Figure 2.17. In dual-band detectors which are back-illuminated, the epilayer which is sensitive to shorter cut-off wavelength is grown first, before the longer cut-off wavelength epilayer. The shorter cut-off photodiode acts as a long wavelength pass filter for the top layer [50].
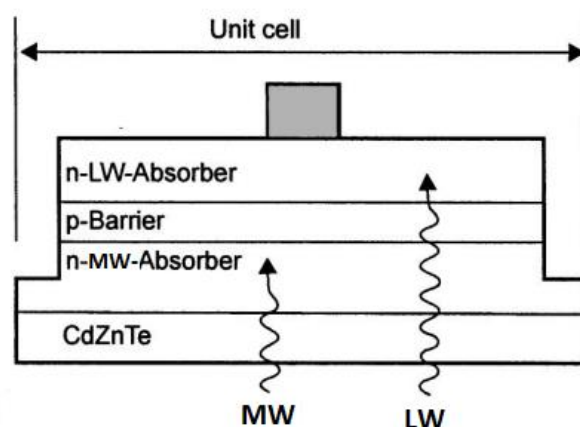
Figure 2.17. Cross-section view of unit cell for bias-selectable n-p-n MW/LW structure [50].

44

In back-to-back photodiode, each unit cell has single indium bump that enables sequential bias selectivity of the spectral bands. When the bias is positive, LWIR photodiode is reverse biased, whereas the bottom (MW) one is forward biased. The photocurrent which is supplied by MWIR is shunted, and hence the total photocurrent is supplied by the LW epilayer. When the bias voltage polarity is changed, the mechanism reverses. For two color MW/LW HgCdTe detectors, the absorption layer thickness is strongly correlated with the crosstalk. In two-color detectors, crosstalk is generally referring to spectral crosstalk within one pixel of MW/LW arrays. The absorption layer design should be determined in a way to obtain minimum crosstalk and maximum quantum efficiency [50]. In the following paragraphs, recent studies on MWIR\LWIR third generation infrared detectors will be given.

Diagnostic/Retrieval Systems (DRS) works on high density vertically integrated photodiode (HDVIP) technology to develop third generation FPAs. In 2001, Kinch et al. from DRS reported the performance of 320x240/50 μm pitch two-color MW/LW FPA. Spectral bands were 3.0-5.2 μm and 8.0-10.2 μm, and mean NETD values were 9 mK and 23 mK under f/3 optics with 97.1% and 96.3% operability for MWIR and LWIR bands, respectively. The spectral crosstalk of the array was reported to be smaller than 3% [51].

Dual band detectors of Raytheon Vision Systems are based on n-p-n triple layer heterojunction back-to-back diode detector structure with narrow trenches isolating mesa. In 2006, they reported the initial results of 1280x720/20 μm pitch dual band detector. The LWIR cut-off was 10.5 μm and that of MWIR was 5.5 μm at 78 K. FPAs demonstrated high sensitivity at 78 K with NETD values smaller than 30 mK and 20 mK with f/3.5 apertures for LWIR and MWIR, respectively. Pixel operability was greater than 99.9% in the MWIR band and greater than 98% in the LWIR band [52].

CEA-LETI reported their results for MWIR/LWIR dual band FPA which was developed using pseudo-planar structure in 2007. In pseudo planar structure, each pixel includes of two n on p structure photodiodes for different spectral bands. One is

located at the bottom of an etched hole, while the other is on the surface. A common contact enables biasing of both upper and lower p-type layers. In this structure, the two detectors can perform simultaneously. An FPA was fabricated with 256x256 format, 30 μm pixel pitch and 4.8 μm and 9.7 μm cut-off wavelength for MWIR and LWIR, respectively. The best NETD values were 12 mK and 25 mK at 77 K with f/2 optics with the operability as high as 99.1% and 95.1% for MWIR and LWIR, respectively [53].

In 2009, SOFRADIR introduced their prototype ALTAIR, 640x512/24 μm pitch MW/LW dual band detector. The semi-planar structure featured two standard n on p photodiodes per pixel, located in two absorbing layers associating with two different spectral bands. Each pixel had two independent contacts and separate input stages to simultaneously integrate the photocurrent from both bands. MWIR detector was sensitive to 3-5 μm, whereas LWIR detector responded to radiation in the 8-9.5 μm wavelength interval. The crosstalk between different spectral bands was 1%. The mean NETD values were 20 mK and 25 mK with 99.5% operability for MWIR and LWIR bands, respectively [54].

In 2010, SOFRADIR reported their latest product, 640x512/20 μm pitch, ALTAIR dual band detector which was the improved version of an older product with 24 μm pitch. The structure and working principle were the same as previous version. The mean NETD values were 12.5 mK and 23.9 mK for f/2 optics at 80 K operating temperature for MWIR and LWIR bands, respectively [55].

In 2014, Weida Hu *et. al.* [56] from National Laboratory for Infrared Physics in Shanghai Institute of Technical Physics reported the results of 128x128 MW/LW array which was fabricated by simultaneous nonplanar B implantation on the photodiodes with mesa isolation. The cut-off wavelengths were 4.8 μm and 9.7 μm, and peak detectivities were 3.2×10^{11} and 4.3×10^{10} cmHz$^{1/2}$/W for MWIR and LWIR, respectively. Ultralow LW-to-MW crosstalk of 1.25% and MW-to-LW crosstalk of 0.7% were achieved.

This chapter has presented historical development of $Hg_{1-x}Cd_xTe$ and material properties. Literature survey on MWIR, LWIR and dual-band $Hg_{1-x}Cd_xTe$ detectors were also summarized by concentrating on the most recent studies. The detector epilayer structure and fabrication procedure details of test arrays and the 320x256 FPA fabricated in this work are explained in the next chapter.

CHAPTER 3

FABRICATION OF LONGWAVE HGCDTE
TEST ARRAYS AND FOCAL PLANE ARRAY

Infrared FPA production consists of a detailed micro-fabrication process. In this thesis study, test arrays with 30 μm pitch pixels and LWIR 320x256/30 μm FPAs were fabricated with developed processes. The HgCdTe layers used in this study were grown by Molecular Beam Epitaxy (MBE) at the Quantum Devices and Nanophotonics Research Laboratory of the Electrical and Electronics Engineering Department, Middle East Technical University (METU). The fabrication processes were conducted at ASELSAN. Before going into the details of the fabrication processes, a brief information will be given about MBE growth and epilayer structures.

3.1. MBE Growth

Growth of single-crystal high quality MCT material has many difficulties because of high Hg vapor pressure. High vapor pressure makes controlling the composition and stoichiometry of material more challenging. Material properties such as dopant density, alloy composition and crystalline defect density are strongly dependent on growth conditions. In general, two epitaxial growth methods are used: vapor phase epitaxy (MOCVD and MBE) and liquid phase epitaxy (LPE) for HgCdTe growth [15].

MBE is an ultra-high vacuum (UHV) system which contains beam shutters, their actuating mechanisms, source ovens, in situ characterization tools, a substrate holder and heater, beam-flux monitors and cryopanels to act as cryopumps. The schematic of an MBE chamber is shown in Figure 3.1 [57]. The system utilizes low vacuum levels less than 5×10^{-11} Torr, and minimizes the contamination during growth. Thanks to high vacuum, the atoms and molecules can arrive the substrate without any collision.

Shutters opening and closing times are much shorter than the growth time of single atomic layer, which enables a designer to control stoichiometry, composition and uniformity more accurately [19].
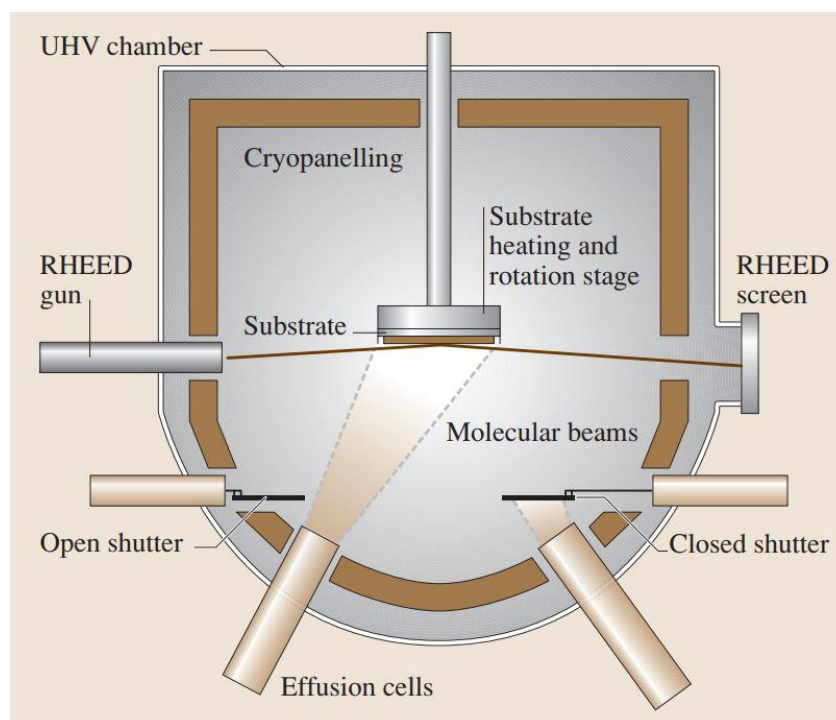
Figure 3.1. Schematic of a typical system for MBE [58].

The advantages of MBE growth are summarized in the following items.

- The MBE growth temperature for HgCdTe is around 185 ^{o}C, whereas LPE and MOCVD growth temperatures are much larger than that of MBE, around 300 ^{o}C – 400 ^{o}C. The low temperature reduces the diffusion of constituent or dopant atoms, and makes constructing abrupt junctions possible [59].
- MBE has relatively small growth rates with respect to other techniques, and this allows the reliable growth of multilayer thick layers [59].
- In-situ monitoring of the growing film is possible with MBE systems. Mass spectrometry and reflection high-energy-electron diffraction (RHEED) are often used [57].

50

3.2. Epilayer Structure

FPAs with three different passivation process were fabricated on the same epilayer and investigated in this study. The epilayers have the P+ on n hetero-structure. The epilayers were grown on CdZnTe substrates using the MBE technique with In and As the n and p type dopants, respectively. The absorber (~7 μm with 0.23 cadmium mole fraction) doping is kept at low level being in the order of 10^{15} cm^{-3}. Hence, low doping density in the absorber layer is necessary to keep the recombination lifetime long and dark current small. The absorber layer thickness is selected based on the absorption coefficient of the material and the expected diffusion length. The p-type layer Cd mole fraction is selected to be higher than that of the absorber in order to minimize the contribution of the Auger-7 mechanism in this layer to the dark current. The top layer, HgTe, is preferred due to its high work function to establish good ohmic contact on p-type doped HgCdTe [60].

As p-type dopant (As) activation, two-step annealing was performed on epilayers before fabrication of test arrays and FPA. During MBE growth, As atoms incorporate into the metallic (Cd, Hg) sublattice of the zinc blende crystal under Te-saturated conditions. This mechanism results in much higher Hg vacancies in as-grown HgCdTe than the density of Te vacancies. As atoms should be placed on Te sites in order to be activated as p-dopants [61], [62]. The dopant activation step includes two-step thermal anneal under Hg overpressure including a short high temperature and a long low temperature step. In the first step, As atoms are activated at high temperature over 400 ^{o}C, and in the second step, Hg vacancies forming in the material due to high temperature annealing step and during growth are annihilated at temperatures around 250 ^{o}C [28].

3.3. Fabrication of Test Arrays and FPA

Handling and processing HgCdTe are very challenging, since it is very fragile and sensitive material due to the weak nature of Hg-Te bonds. Necessary precautions such as not exposing the material to temperature higher than 80 ^{o}C should be taken during

fabrication steps in order not to degrade the material properties. In this study, test arrays and FPAs were fabricated in the 30 μm pitch mesa structure incorporating in-situ doped p-on-n material. The test arrays (fabricated on the same wafer piece with the FPA) include pixels identical to those of the FPA. However, the test arrays were hybridized to Si fan-out substrates while the focal plane array was bonded to an ROIC by flip chip alignment/bonding technique. Hybridization of the test arrays to the Si fan-out substrate facilitates direct electrical access to the pixels as well as allowing optical characterization through backside illumination. In order to allow reliable electrical and optical characterization, test pixels are connected in shunt in the form of matrices. Hence, this arrangement allows acceptable signal to noise ratio in the measurements performed during the characterization.

In order to compare the characteristics of FPAs and test pixels fabricated with different passivation/annealing processes, three different FPAs were fabricated as follows.

- FPA-1 was fabricated with a double passivation layer (CdTe/ZnS). This material was annealed once (only after growth for dopant activation).
- FPA-2 was fabricated with only CdTe passivation layer and annealed twice. The first annealing process was for dopant activation after growth, and the second one was performed after CdTe coating.
- FPA-3 was fabricated with a double passivation layer (CdTe/ZnS). The only difference between the first and the third FPA was an additional annealing process applied to this FPA after CdTe passivation layer deposition.

The steps of the utilized fabrication processes for FPA-2 are as follows.

- Since the fabrication process has many steps, alignment markers should be placed to be able to align the different processes with respect to each other. As a first step, alignment marks were placed with photolithography.
- Pixels with 30 μm pitch were formed on the wafer through the definition of mesas by wet etching with a Bromine based solution. Mesa etching was performed to be deep enough to isolate the mesas from each other in order to

52

minimize the electrical and optical crosstalk between the pixels. A partial photograph of the wafer after mesa etching is shown in Figure 3.2.
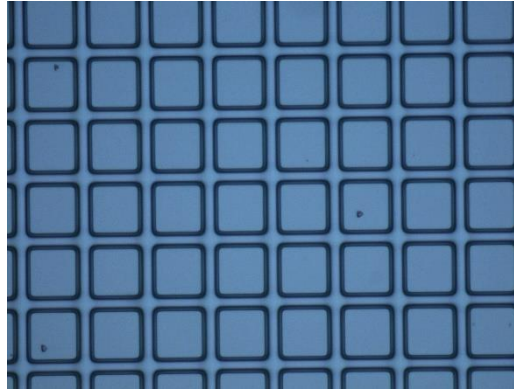
Figure 3.2. Mesa pattern constructed by mesa etch.

- CdTe as a passivation layer was coated in an MBE system.

- Thermal annealing under Hg overpressure was performed as a passivation annealing in order to enhance the passivating properties of the CdTe/HgCdTe interface. A compositionally graded CdTe/HgCdTe interface improves the defective interface, which acts as repulsive barrier for both electron and holes and reduces surface recombination velocity [63].

- Annealed passivation layer was etched to form both p and n-type ohmic contacts on the top of the HgTe and the absorption layers, respectively. Ohmic contact metals were formed by thermal evaporation in a high vacuum chamber.

- Flip-chip bonding process is a method for interconnecting pixels to external circuitry such as Si fan-out or ROIC with In bumps. In order to prepare the wafers for hybridization to fan-out and ROIC, under bump metallization (UBM) coating was performed followed by the formation of In bumps through thermal evaporation and lift off. (Figure 3.3).
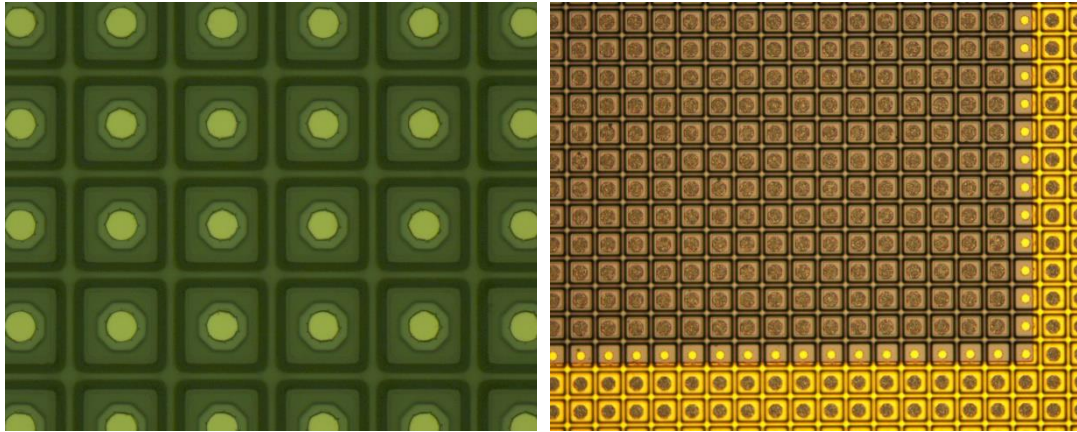
Figure 3.3. UBM and In photolithography and sample after In coating and lift-off.

Fan-out and ROIC should also be processed for UBM and In coating before hybridization. Flip-chip bonding was done under formic acid to break the oxide layer on In bumps.

The process steps are illustrated schematically in Figure 3.4.
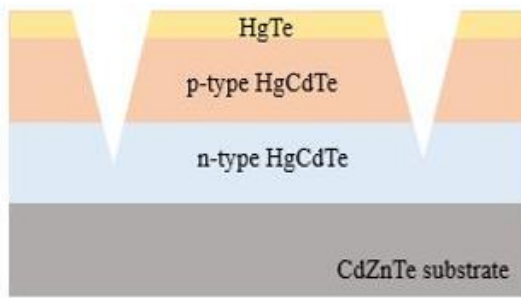
(a) Mesa Etch
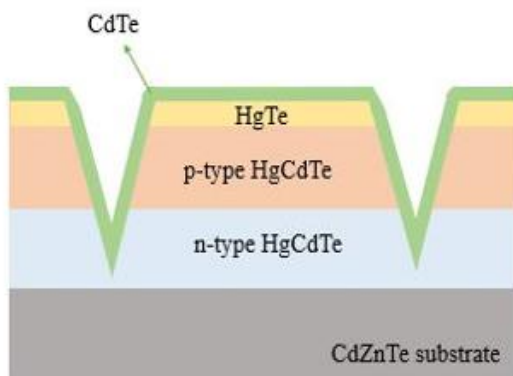
(b) Passivation Coating
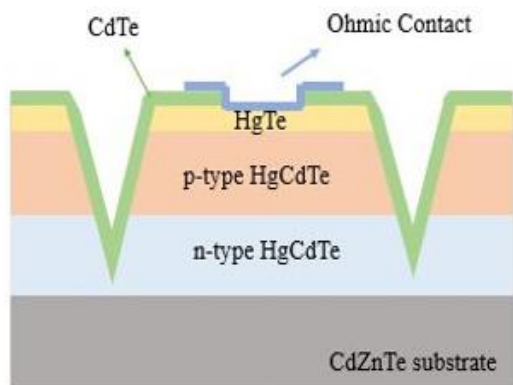
(c) Passivation Etch
and
Ohmic Contact Deposition
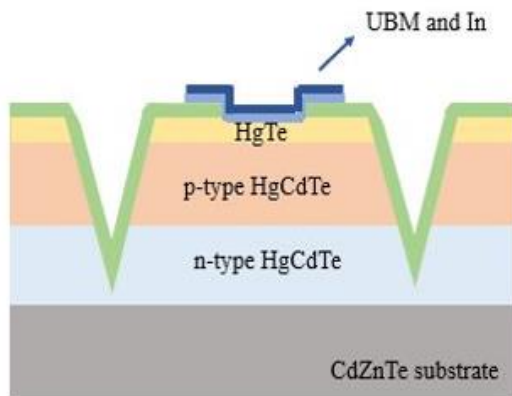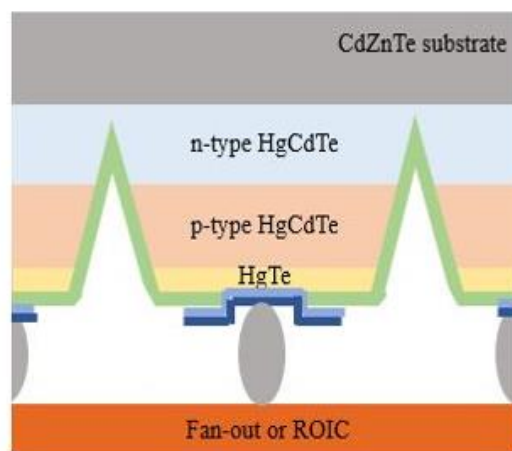
Figure 3.4. Fabrication process steps.

The fabrication process for FPA-1 and FPA-3 include additional steps of ZnS deposition and etching of ohmic contact openings.

This chapter presented a brief information about MBE growth, epilayer structure and the fabrication process steps for the 30 μm pitch detectors investigated in this study. The pixel and FPA characterization study will be described along with the presentation and interpretation of the results.

CHAPTER 4

DETECTOR CHARACTERIZATION AND DISCUSSION

This chapter presents the characterization study conducted on the focal plane arrays and the test pixels. FPA level characterization yields the properties of the FPA such as responsivity and NETD histograms and pixel operability (percentage of the operable pixels). Characterization at the pixel level is conducted on test pixels hybridized to a fan-out circuit. The purpose of pixel level characterization is identification of the signal to noise ratio of the pixels independent of the read-out integrated circuit. Hybridization of the test pixels to the fan-out circuit facilitates electrical access to the pixels in a configuration allowing optical characterization through back side (substrate side) illumination. It should be noted that the test pixel structure is identical to the FPA pixels. While we have characterized the test pixels in detail, we have also used these characterization results in order to estimate the FPA level performance for the verification of the NETD measurements on the FPA.

Figure 4.1 shows the configuration of the test pixels connected in shunt through shorting of the p-sides by the fan-out circuit. Photograph of the hybrid is given in Figure 4.2. The fan-out structure consists of 1, 2x2, 3x3 and 4x4 pixels in the shunt connection arrangement. The main purpose of shunting the test pixels is to increase the signal to noise ratio of the test set-up (detector and preamplifier) during the noise measurements. Hence, reliable noise measurements cannot be performed if the detector noise is below or comparable to the input referred noise of the preamplifier.
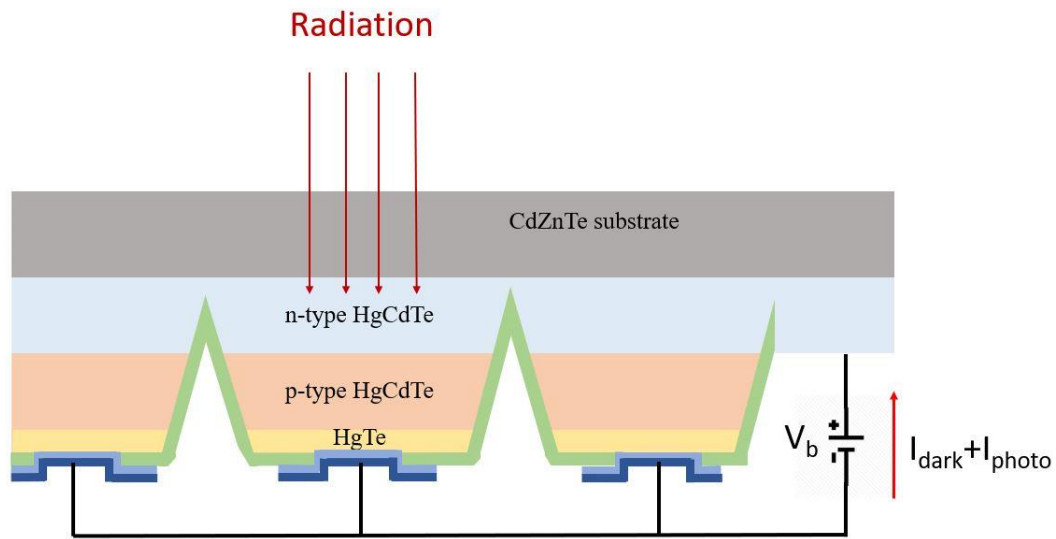
Figure 4.1. Configuration of test pixels shunted by Si fan-out.
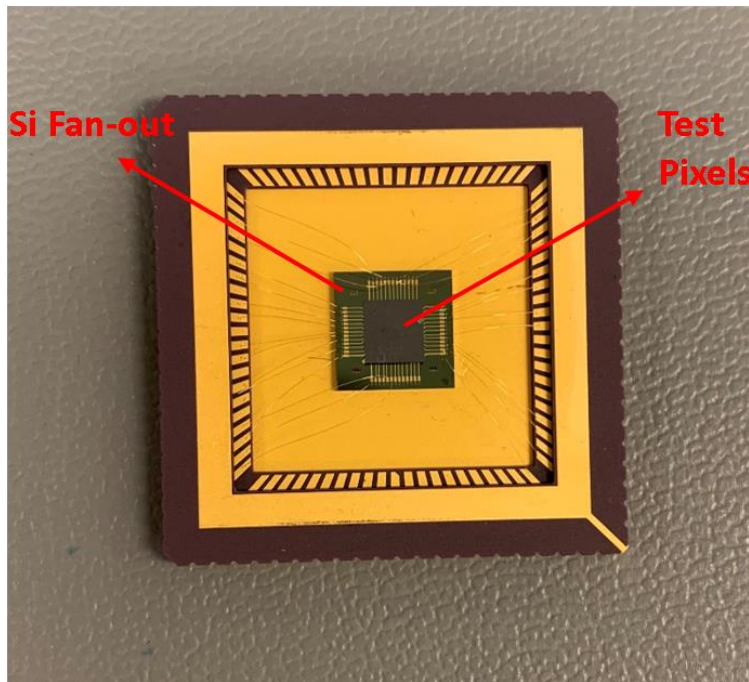
Figure 4.2. Test pixels bonded to Si fan-out.

Test pixel level characterization includes dark/photo current, spectral responsivity and noise measurements. After obtaining these characterization results, the other performance parameters of the detector such as quantum efficiency and detectivity can be determined.

4.1. Dark Current Components

Dark current measurements were performed on the test array with 30 μm pitch pixels by using Keithley 6430 source meter. I_{dark}-V characteristics of 30x30 μm^2 diodes were taken in a test dewar at 78 K under zero illumination corresponding to 1, 2x2, 3x3 and 4x4 diodes.

The dark current-bias voltage measurements were carried out at various temperatures in order to identify the following characteristics of the detectors.

- Dominant dark current components under various reverse bias voltage ranges at the typical operation temperature (78 K) of the detector.
- The variation of the dynamic resistance of the detectors with the bias voltage.
- Variation of the dark current with temperature at various reverse bias voltages which yields some material properties such as G-R lifetime.

There is an upper limit for the pixel operability of the LWIR HgCdTe detector technology due to unavoidable defects and some level of nonuniformity in the material. Therefore, one should not expect identical characteristics in the fabricated test pixels. Due to this reason, while measuring all the test pixels on the array, we have used the measurement results on the test pixels with similar characteristics in order to extract the above described data.

The detector manufacturer can optimize the fabrication processes and the sensor structure if the effects of different current mechanisms on the performance of the detector are known. Generally, current-voltage characteristics or resistance-voltage characteristics are used to quantify the performance of infrared detectors. Major dark current components are diffusion current, generation recombination in depletion

region, tunneling and shunt leakage currents. Shunt leakage appears as an additional dark current component in nonideal detectors and may be due threading dislocations and/or surface leakage in the epilayers. This component of the dark current generally depends linearly on the applied reverse bias voltage exhibiting ohmic behavior.

4.1.1. Diffusion Current

Flow of thermally generated carriers from higher concentration region to lower concentration produces diffusion current in semiconductors. In an ideal p-n junction, it is the only and unavoidable current mechanism. This current density can be expressed as [7], [64]

$$J_{diff} = q \left(\frac{L_p}{\tau_p} \frac{n_i^2}{N_D} + \frac{L_n}{\tau_n} \frac{n_i^2}{N_A} \right) \left(e^{\frac{qV}{kT}} - 1 \right) \qquad (4.1)$$

where V is the applied bias. Diffusion current mechanism is strongly temperature dependent. By using the relation between mobility, diffusion constant and diffusion length, the same expression can be expressed as

$$J_{diff} = \sqrt{qkT} \left(\sqrt{\frac{\mu_p}{\tau_p}} \frac{n_i^2}{N_D} + \sqrt{\frac{\mu_n}{\tau_n}} \frac{n_i^2}{N_A} \right) \left(e^{\frac{qV}{kT}} - 1 \right). \qquad (4.2)$$

When bias voltage is increased, the current increases significantly while the differential resistance accordingly decreases in the forward bias region. The forward biased characteristics can be divided into two subregions. One is governed by diffusion current at small biases, where the current increases exponentially. The other corresponds to low but stable resistance under larger bias voltages, which is the series resistance of the diode [65]. In order to fit the experimental data to the theoretical dark current mechanisms, first series resistance should be calculated and removed from the data.

4.1.2. Generation-Recombination (G-R) Current

Defects within the depletion region result in generation and recombination of carriers. Temperature dependence of G-R current is weaker when compared with that of diffusion current. Hence, this type of current becomes dominant at lower temperatures if the detector does not suffer considerably from tunneling currents.

G-R current density can be expressed as [7], [65], [66]

$$J_{g-r} = \frac{q n_i W_{dep} \sqrt{V_{bi} - V}}{2\tau} \left(e^{\frac{qV}{2kT}} - 1 \right)$$

$$W_{dep} = \sqrt{\frac{2\varepsilon}{q} \frac{N_A + N_D (V_{bi} - V)}{N_A N_D}} \quad , \quad V_{bi} = \frac{kT}{q} \ln \left(\frac{N_A N_D}{n_i^2} \right)$$

(4.3)

where V_{bi} is built-in potential and W is depletion width. Depletion width, intrinsic carrier concentration and built-in potential can be found from the above equations, and the experimental data can be fitted to theoretical generation-recombination mechanisms in order to extract the carrier g-r lifetime.

4.1.3. Tunneling Current

Tunneling of the carriers from the valance band to conduction band directly or through trap states in the depletion region results in tunneling currents. This mechanism is relatively temperature independent, and it strongly depends on band-gap and doping levels. If the transition occurs directly, it is called band-to-band (BTB) tunneling current. Thermally excited carriers can transit to conduction band via trap levels, and in this case, it is called trap assisted tunneling (TAT) current. Tunneling mechanisms are illustrated in Figure 4.3.

Band-to-band tunneling may be dominant in narrow gap semiconductors under moderate and high reverse bias. Band to band tunneling starts when the conduction band on the n side is aligned to the valance band on the p side. Band to band tunneling current density is defined as [67]

$$J_{btb} = \frac{q^3 E \sqrt{2m_e}(V_{bi} - V)}{4\pi^3 \hbar^2 \sqrt{E_g}} \left(e^{-\frac{\pi\sqrt{m_e/2}E_g^{3/2}}{2qE\hbar}} \right) \qquad (4.4)$$

where E is the electric field.
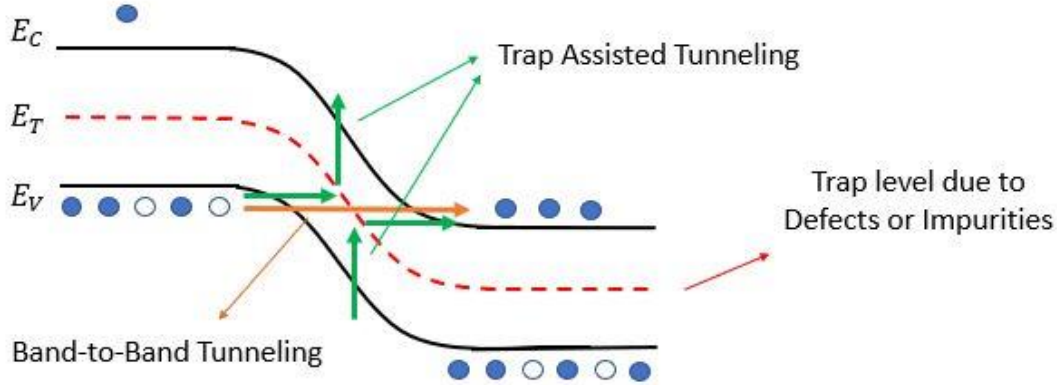
Figure 4.3. Band diagram illustrating tunneling processes.

Trap assisted tunneling current may be the dominant dark current mechanism in low bandgap materials at low temperatures where the thermally generated current components (g-r and diffusion) may be relatively small. Current density due to the tunneling of electrons (from the p-side valence band to the n-side conduction band) through traps can be expressed as [68], [69]

$$J_{TAT} = qN_t \left(\frac{1}{C_p p_1 + w_v N_v} + \frac{1}{w_c N_c} \right)^{-1} W_{dep}. \qquad (4.5)$$

In the above expression, C_p is the hole capture coefficient and p_1 is given as

$$p_1 = N_v e^{-E_t/kT}. \qquad (4.6)$$

The parameters $w_v N_v$ and $w_c N_c$ are the tunneling rates from the valence band to the trap level and from the trap level to the conduction band respectively. These rates

depend on the location of the trap in the bandgap, E_g-E_t (E_t measured from the top of the valence band). w_cN_c is expressed as [68]

$$w_cN_c = \frac{\pi^2 q m_e E M^2}{h^2 (E_g - E_t)} \left(e^{-\frac{4\sqrt{2m_e/2}(E_g-E_t)^{3/2}}{3qE\hbar}} \right) \qquad (4.7)$$

where M is the matrix element associated with trap potential, and E is the electric field at the junction. When the values of the physical constants and the material parameters are inserted into the above equation, the tunneling rate from the trap level into the conduction band states is expressed as

$$w_cN_c = \frac{6 \times 10^5 E}{E_g - E_t} \left(e^{-\frac{1.7 \times 10^{-7} E_g^{1/2}(E_g-E_t)^{3/2}}{E}} \right) \qquad (4.8)$$

where the electric field E is $\frac{q N_D W_{dep}}{\epsilon_0 \epsilon_s} \left(\frac{V}{cm} \right)$.

In case, the tunneling rate is not limited by the hole capture (w_cN_c, $w_vN_v << C_pp_1$) and assuming that $w_vN_v \cong w_cN_c$, the trap assisted tunneling current density expression can be simplified as

$$J_{tat} = q N_t W w_c N_c. \qquad (4.9)$$

4.1.4. Ohmic Leakage Current

Dislocations in the material and surface leakage currents may result in excess dark current showing linear dependence on the bias voltage, which is namely ohmic leakage current. This mechanism exhibits shunt-like behavior in the I-V characteristic of the detector. Shunt current can be expressed as

$$I_s = \frac{V}{R_{sh}} \qquad (4.10)$$

where V is the applied voltage and R_{sh} is the diode shunt resistance.

4.2. Pixel Level Characterization

Dark current modeling was performed on the I$-V$ characteristics of test diodes in order to identify the major dark current components and parameters related with them. First, by using empirical equations given in Chapter 2, necessary parameters were calculated at the operation temperature and Cd mole fractions of the epilayers. Then, the following procedure was pursued for fitting.

- Series resistance should be calculated and removed from data, which is effective at moderate/large forward bias voltages.

- Under moderate and low reverse bias, trap assisted tunneling mechanism may be responsible for the dark current. Hence, trap level as $\frac{E_t}{E_g}$ and N_t can be calculated by fitting Equation (4.5) and (4.7) to the measured data after isolating the trap-assisted tunneling component of the dark current.

- Generation-recombination lifetime can be calculated by fitting the experimental data to Equation (4.3) at the bias voltages where this component is dominant.

- Diffusion current is likely to be dominant at elevated operation temperatures where this current component can be isolated from the other components and parameters such as carrier recombination lifetime can be extracted.

The material parameters used in this study are given in Table 4.1.

Table 4.1. Material parameters for Hg$_{1-x}$Cd$_x$Te (x = 0.231) at 78 K used in dark current modeling.

N_A, N_D (cm^{-3})	E_g (eV)	n_i (cm^{-3})	V_{bi} (V)	ε_s (F/cm)
$1 \times 10^{17}, 8 \times 10^{15}$	0.133	4.624×10^{12}	0.120	1.524×10^{-12}

4.2.1. Diffusion Length Analysis

A difficulty in the characterization of detectors constructed with materials exhibiting considerable carrier diffusion length is the lateral collection by the detector mesa

under test. This may result in the overestimation of both dark current and the quantum efficiency of the detector unless the active area of the pixel is corrected after determining the diffusion length. This correction is especially necessary in the characterization of small dimension pixels which are more prone to lateral collection which is the case in this work. We should note here that the lateral collection length may be different than the vertical diffusion length in the mesa structure due to possibly different rates of surface recombination in these regions. Lateral collection length analysis was performed through the utilization of photo-response measurements as follows.

The lateral collection length was evaluated from the dependence of photo current on the diode size. Electron-hole pairs generated in the p-n junction and those collected laterally contribute to the detector current [70]. The photo current can be evaluated as

$$I_p = j_p \times Area \qquad (4.11)$$

where j_p is the photo current density.

The lateral collection contribution to the current was considered in order to calculate the active area of the test pixel. Corresponding diode active areas can be defined as

For a single diode: $A_d = (Pitch\ Size + 2 \cdot L_d)^2$

For 2x2 diode: $A_d = (2 \cdot Pitch\ Size + 2 \cdot L_d)^2$

For 3x3 diode: $A_d = (3 \cdot Pitch\ Size + 2 \cdot L_d)^2$

For 4x4 diode: $A_d = (4 \cdot Pitch\ Size + 2 \cdot L_d)^2$

The details of active area calculations for 1 and 4x4 diodes are given in Figure 4.4.
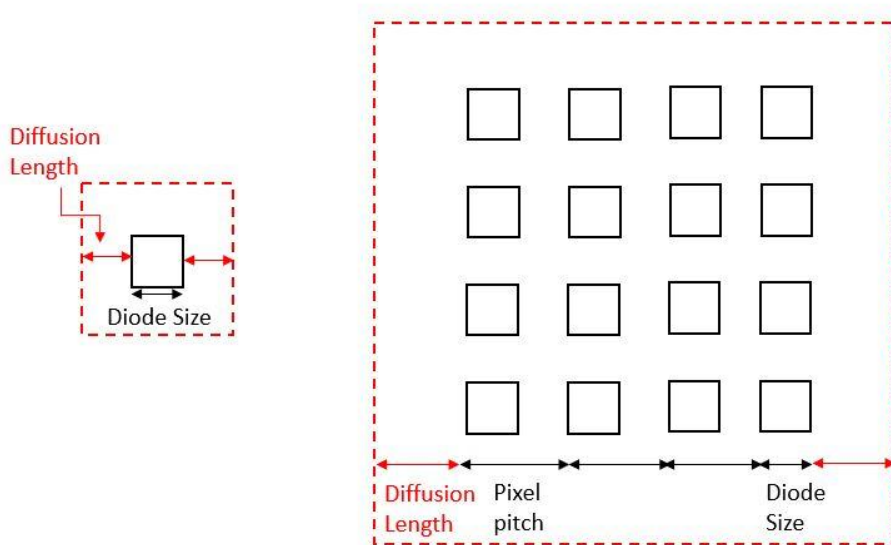
Figure 4.4. The area calculations for 1 and 4x4 diodes.

The experimental photo current values at 10 mV reverse bias for 1, 2x2, 3x3 and 4x4 diodes were obtained and the square root of these values was plotted with respect to diode size as shown in Figure 4.5. In mesa structure, pixel pitch and diode size can be assumed to be same. The lateral collection length, L_c, was found as 3 μm from the half of the intersection point between x axis and a trend line passing across the experimental data points.
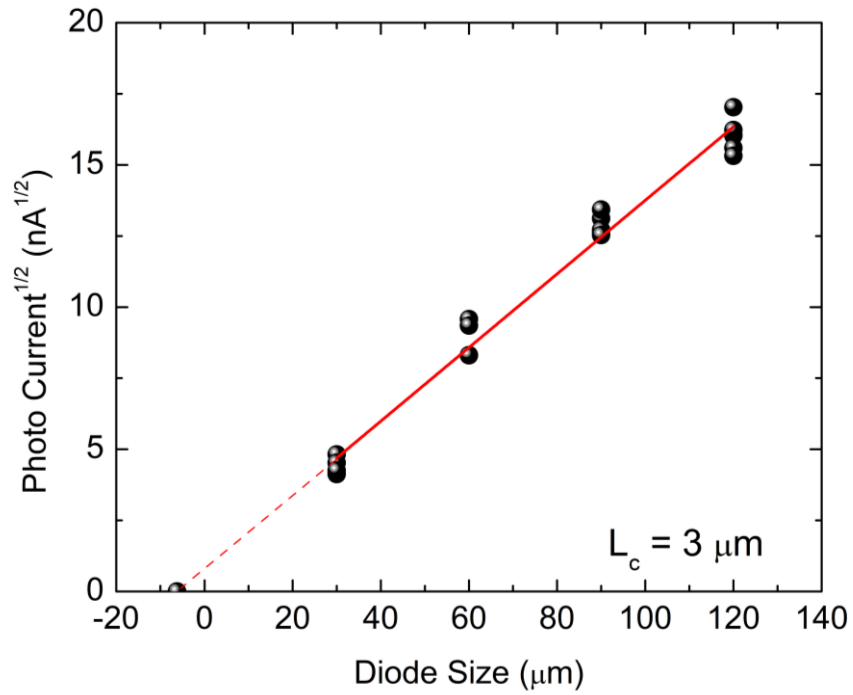
Figure 4.5. Calculation of L_c from linear fitting.

4.2.2. Dark Current Analysis

The dark current characteristics of the test pixels fabricated with different processes are presented in Figure 4.6-Figure 4.8. The differences between the processes utilized in the fabrication of these pixel arrays are summarized in Table 4.2.

Table 4.2. Variation in test pixel arrays fabrication.

	First Passivation Layer	Second Passivation Layer
Pixel Array-1	CdTe	ZnS
Pixel Array-2	Annealed CdTe under Hg overpressure	-
Pixel Array-3	Annealed CdTe under Hg overpressure	ZnS
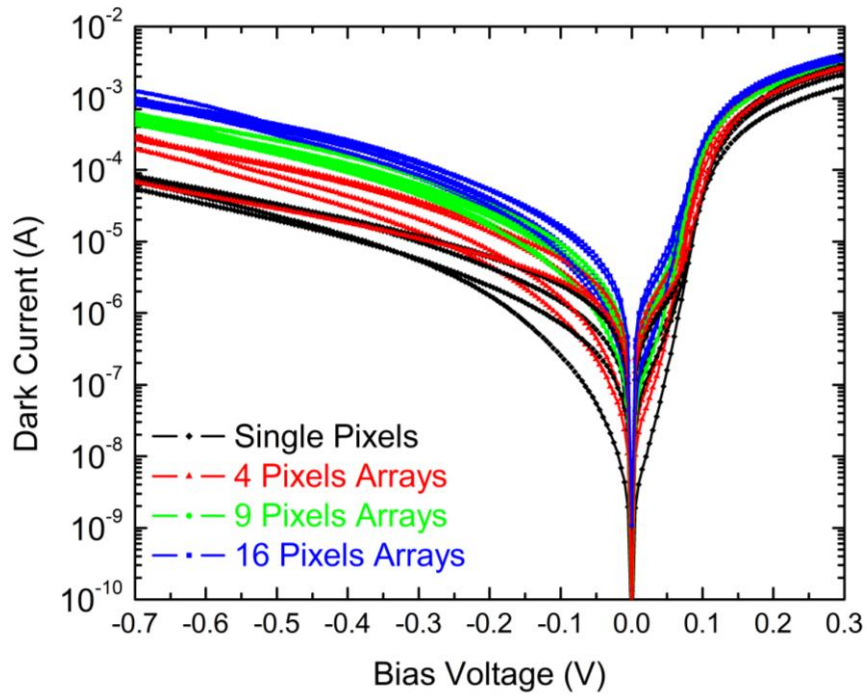
Figure 4.6. The I-V characteristics of Pixel Array-1 under dark at 77 K.
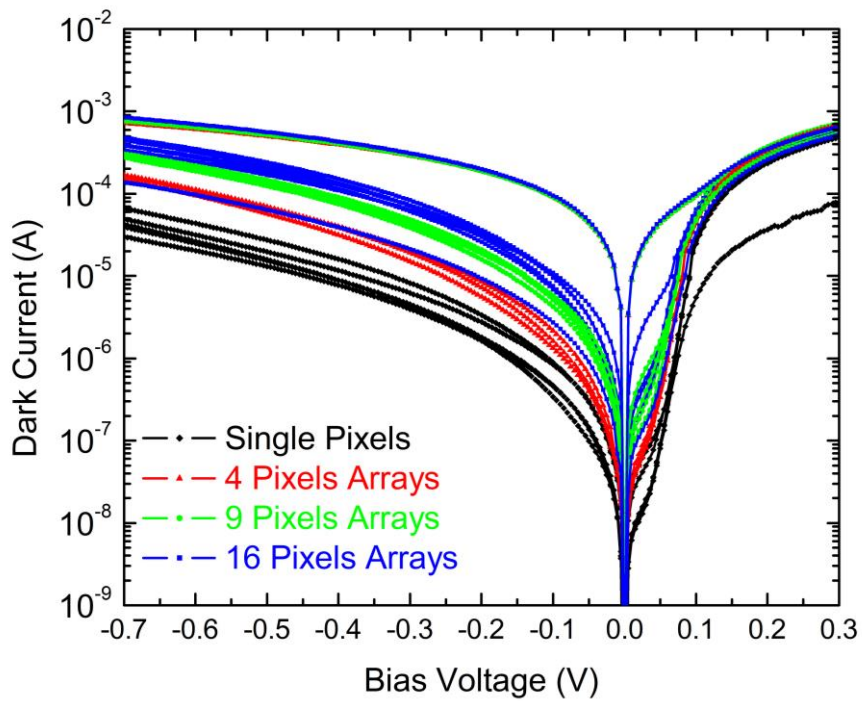
Figure 4.7. The I-V characteristics of Pixel Array -2 under dark at 77 K.
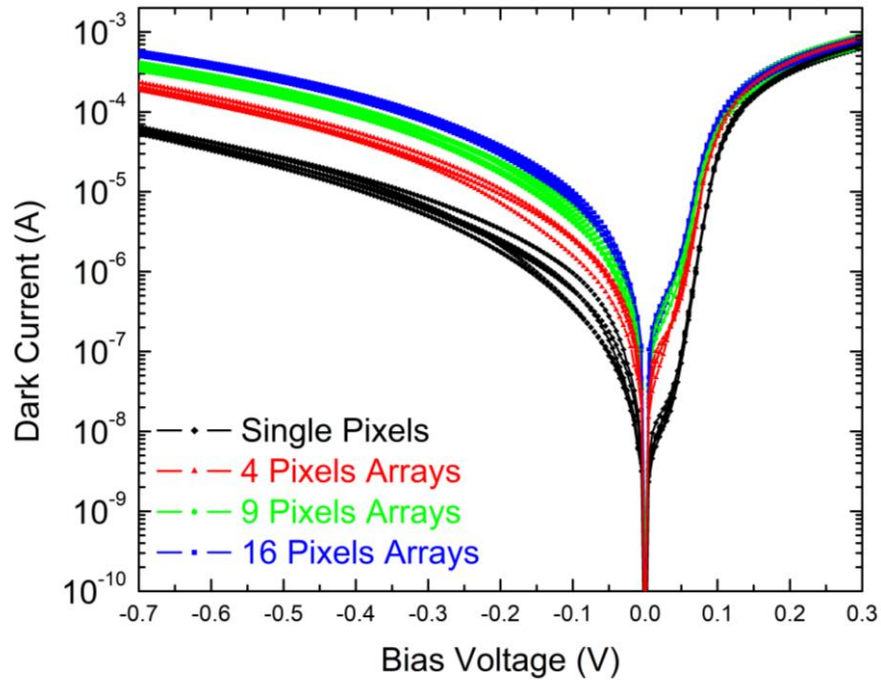
Figure 4.8. The I-V characteristics of Pixel Array-3 under dark at 77 K.

As can be seen from the above figures, the measurement results of Pixel Arrays-1 and 2 are scattered which is possibly due to improper passivation technique applied to these arrays. The scattering in the results cannot be attributed to nonuniformity in the material since all the pixels arrays were fabricated using the same epilayer structure. An important observation is the comparable dark current levels obtained when the functional pixels of Array-1 and Array-2 are considered together with the pixels of Array-3 which exhibits less scattered data. Regarding the degraded pixels of Arrays 1 and 2, higher dark currents in those pixels are likely to be due to less perfect surface passivation since all the arrays were subjected to the same fabrication process except the passivation step which is not supposed to change the bulk components of the dark current.

Since the characteristics of Pixel Arrays-1 and 2 are degraded, the pixels of these arrays were not subjected to detailed dark current analysis. Indeed, such an analysis would be difficult due to the uncertainty in the characteristics of these detectors. On

69

the other hand, since the functional pixels in all arrays show similar dark current-bias voltage characteristics, it can be suggested that the dark currents in these pixels are generated by similar mechanisms. However, there is no reason to assume that the dark current of the pixels with acceptable characteristics is generated by bulk mechanisms. Hence, the pixel dark currents in the arrays may still be dominated by the surface leakage in which case it can be concluded that none of the passivation processes is ideal in terms of passivating the surface charge. The passivation process applied to Pixel Array-3 seems to be somewhat better than the others. Therefore, we have conducted dark current modeling study on Pixel Array-3 in order to estimate the performance limiting factors associated with this array and the utilized passivation process.

Figure 4.9 shows the dark current characteristics of Pixel Arrays-3 which are obtained by dividing the total dark current measured on an array to the number of pixels in the array. It should be noted that the differences in the forward bias characteristics result from the combination of the series resistance of the metal interconnection line on the fan-out circuit and the metallization contact resistance. The bias voltage dropping on the junction (which determines the diode current) is equal to the voltage drop on the series resistance subtracted from the applied bias. Since the arrays having larger number of pixels conduct higher dark currents (resulting in larger voltage drop on the metal lines), the voltage drop on the pixel junctions of these arrays is smaller than those of the arrays with smaller number of pixels. It should also be noted that this difference is not reflected to the reverse bias characteristics due to much larger junction resistances in this region.

In order to extract sufficient data for dark current modeling of Pixel Array 3, this array was subjected to variable temperature (50–190 K) I-V measurements by using a He cryostat. Figure 4.10 shows the averaged dark current characteristics of a single pixel which was obtained by measuring the current of two 9-pixel arrays shunted and dividing the measured current by 18.

70
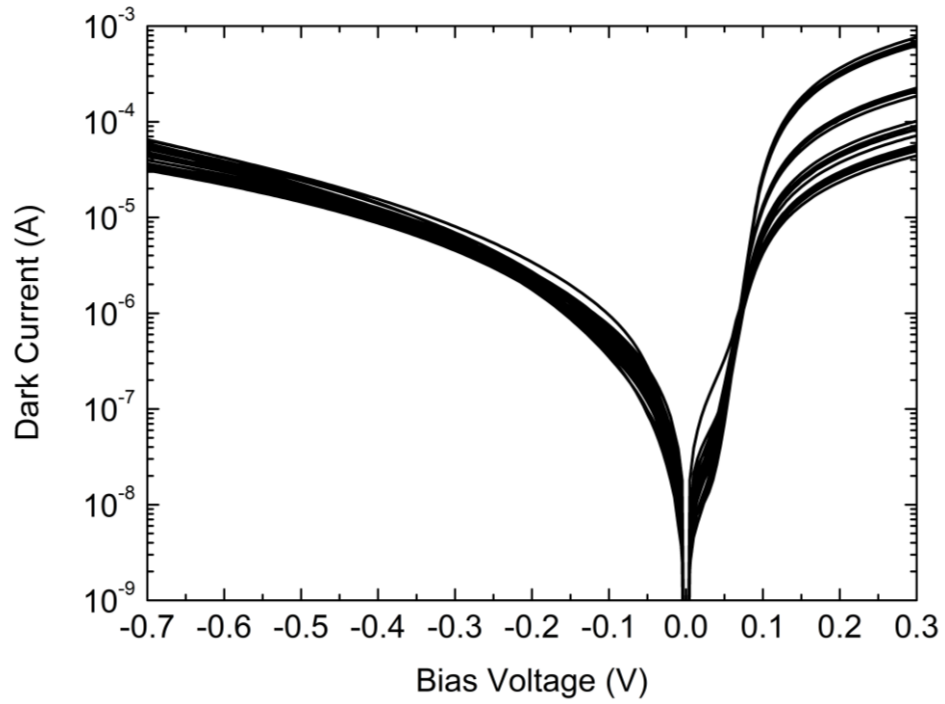
Figure 4.9. The I-V characteristics of every single pixel in Pixel Array-3 under dark at 77 K.
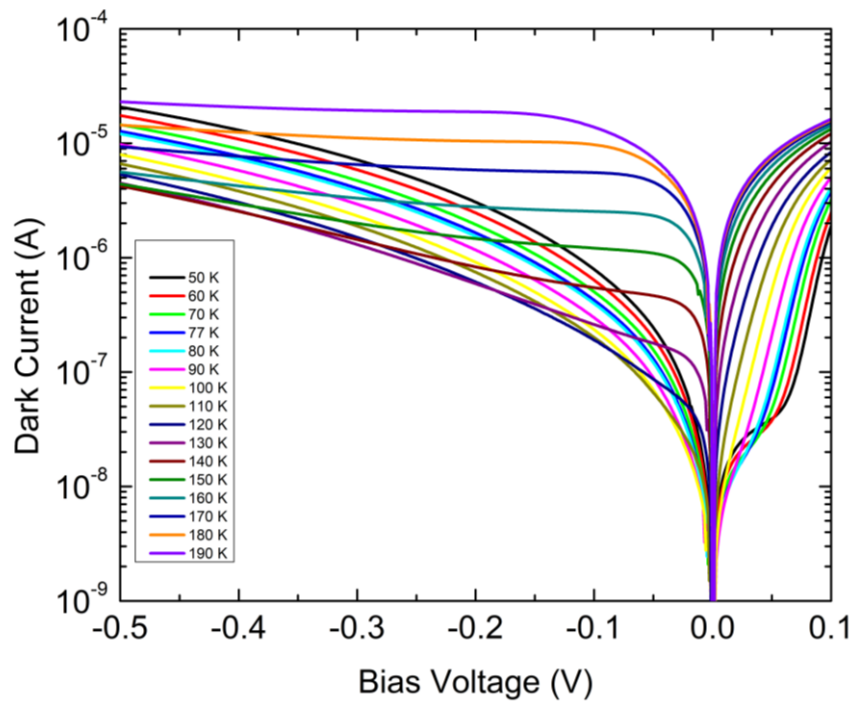
Figure 4.10. The dark current characteristics varying with temperature.

One possible approach to extract various material parameters and performance degrading mechanisms may be the fitting of the following equation to the measured I-V characteristic of the detectors. The total dark current can be expressed as

$$I_{dark} = I_{diff} + I_{G-R} + I_{TAT} + I_{SH} \tag{4.12}$$

where I_{diff}, I_{G-R}, I_{TAT} and I_{SH} are the diffusion, G-R, TAT and shunt (ohmic leakage) components of the dark current. However, due to the large number of unknown parameters, precise material extraction through this approach would be too difficult. Therefore, we have chosen to initiate the dark current analysis at elevated temperatures and small enough bias voltage where the diffusion component of the dark current is expected to be dominant. Indeed, at relatively high temperatures (T≥ 150K) and low/moderate reverse bias voltages, the diodes seem to be diffusion limited. (see Figure 4.10). In order to justify this observation, we provide in Figure 4.11 the dark current thermal activation energy of 0.161 eV extracted from the dark current measured under 200 mV reverse bias at various temperatures. This activation energy corresponds to the bandgap energy of the material in the temperature region of interest. Hence, the temperature dependence of the diffusion component of the dark current is dominated by n_i^2 dependence which increases in proportion to exp(Eg/kT). Therefore, the data given in Figure 4.11 confirms the diffusion dominated operation of the diode at and above 150 K.
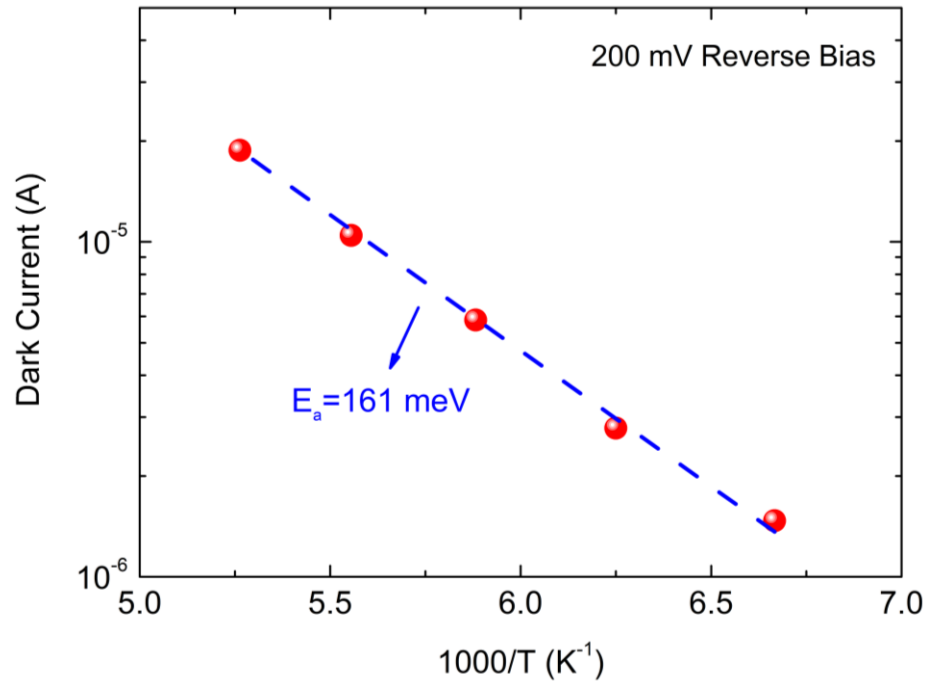
Figure 4.11. Activation energy at diffusion limited region.

As the temperature is lowered, the generation-recombination and tunneling mechanisms start to considerably contribute to the dark current (see Figure 4.12). The soft breakdown characteristic observed in a wide reverse bias region suggests the presence of trap assisted tunneling (TAT) and the absence of band to band tunneling in this bias region. This observation will be verified by detailed dark current modeling in the following sections.

Diffusion and G-R current expressions are well known as given by Equations (4.1)-(4.3). Figure 4.12 shows the measured I-V characteristics together with the results of fitting considering the diffusion and G-R components of the dark current only. The onset of trap assisted tunneling can clearly be observed in this figure.
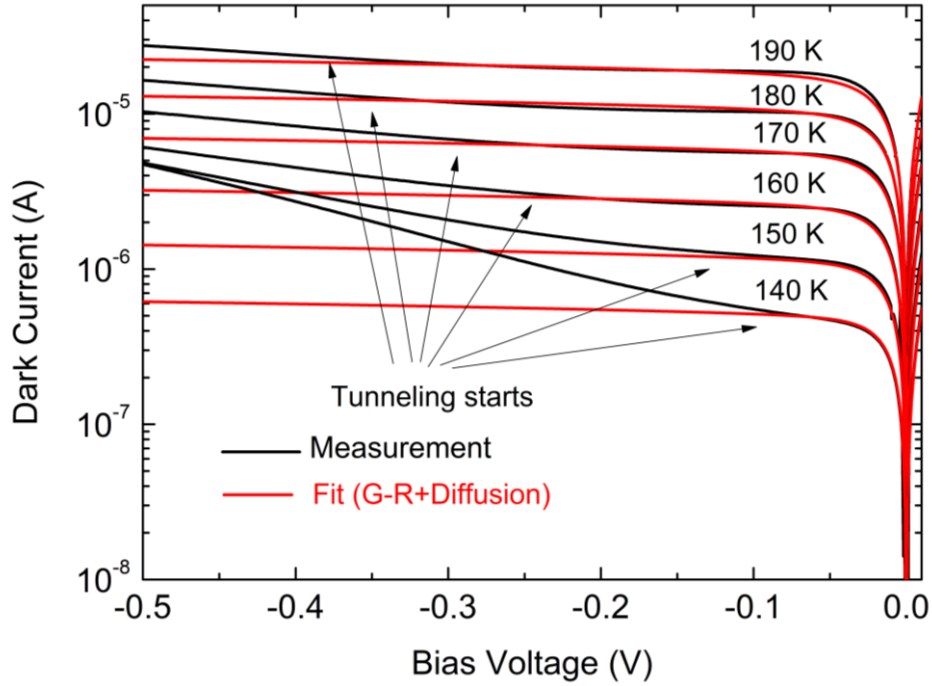
Figure 4.12. Fit characteristics without trap-assisted tunneling.

Diffusion current constants were estimated by fitting experimental data at 8 different elevated temperatures (120-190 K) and under reverse bias voltages where the TAT mechanism does not set in. The temperature dependence of the normalized diffusion constant is presented in Figure 4.13 showing that the diffusion current increases somewhat in proportion to $n_i{}^2$. The deviation from the $n_i{}^2$ line is due to the temperature dependence of the additional parameters in the expression for the diffusion current coefficient.

In a p^+-n junction, the diffusion current coefficient (defined as C in Figure 4.13 above) can be expressed as

$$C = qA \frac{L_p}{\tau_p} \frac{n_i{}^2}{N_D} \left[\frac{s\frac{\tau_p}{L_p} + tanh\left(\frac{d_{abs}}{L_p}\right)}{1 + s\frac{\tau_p}{L_p} + tanh\left(\frac{d_{abs}}{L_p}\right)} \right] \qquad (4.13)$$

74

where d_{abs} is the thickness of absorber layer, and s is the recombination velocity at the end of the n side of the diode. In case the term in the brackets approaches 1, C can be approximated as

$$C = qA\frac{L_p}{\tau_p}\frac{n_i^2}{N_D} = qA\sqrt{\frac{D_p}{\tau_p}}\frac{n_i^2}{N_D}. \qquad (4.14)$$

The above approximation (being independent of s) simplifies the extraction of material parameters from dark current modeling.
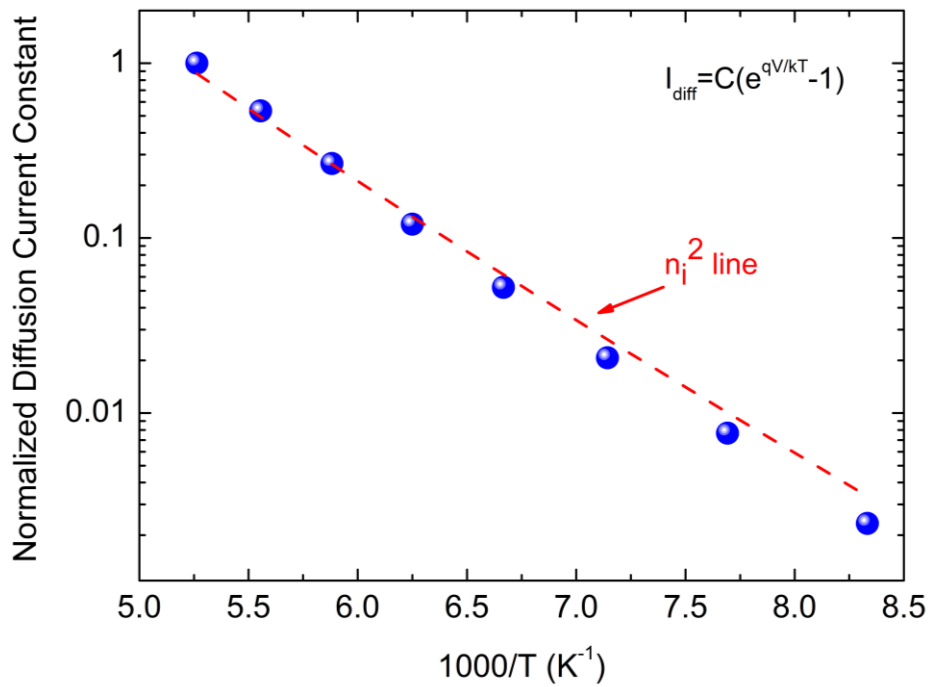
Figure 4.13. The temperature dependency of diffusion current coefficient.

As stated by Equation (4.14), the obtained diffusion current coefficients (C) can be utilized to extract the hole recombination lifetime (τ_p) in case the doping (N_D) and hole mobility (μ_p) in the n-side are known. Hence, the hole diffusion coefficient (D_p) in this side of the diode is linked to the hole mobility through the Einstein relation stating that $D_p = kT\mu_p/q$. Unfortunately, there does not exist much data in the literature regarding the minority carrier (hole) mobility in n-type HgCdTe. The lack of this data can be attributed to the fact that most of the photovoltaic HgCdTe detectors were

constructed in the n on p structure until recently. Hence, in this structure, minority carriers establishing the dark current are electrons making the electron mobility in the p-type material of interest. We have used the results of the hole mobility measurement in n-type HgCdTe (through Haynes Shockley experiment) of Y. Shacham-Diamand and I. Kidron [71] to model the temperature dependence of the hole mobility in the n-side of our detectors as $10^8 T^{-2.78}$. Figure 4.14 shows the hole recombination lifetime, τ_p, appearing in the diffusion current coefficient expression (Equation (4.14)) extracted from the measured data with the above-mentioned hole mobility modeling.

The hole recombination lifetime τ_p depends on the G-R (SRH) ($\tau_{pG\text{-}R}$), Auger (τ_{Auger}) and radiative ($\tau_{radiative}$) lifetimes of the holes as implied by the following equation

$$\frac{1}{\tau_p} = \frac{1}{\tau_{pAuger}} + \frac{1}{\tau_{pRadiative}} + \frac{1}{\tau_{pG-R}}. \qquad (4.15)$$

As can be seen from the above equation, the overall hole recombination lifetime is linked to the G-R recombination lifetime. In trap free or low G-R center density (very pure and high crystal quality HgCdTe material), the G-R recombination lifetime is much larger than the Auger and radiative lifetimes and the lifetime is mostly determined by the Auger and radiative lifetimes (Auger lifetime generally being smaller than the radiative lifetime). This is the reason for calling the best HgCdTe photovoltaic detectors (those used to establish the well-known Rule 07 [72]) as Auger limited detectors. On the other hand, G-R lifetimes differing by several orders of magnitude have been reported for the HgCdTe material.
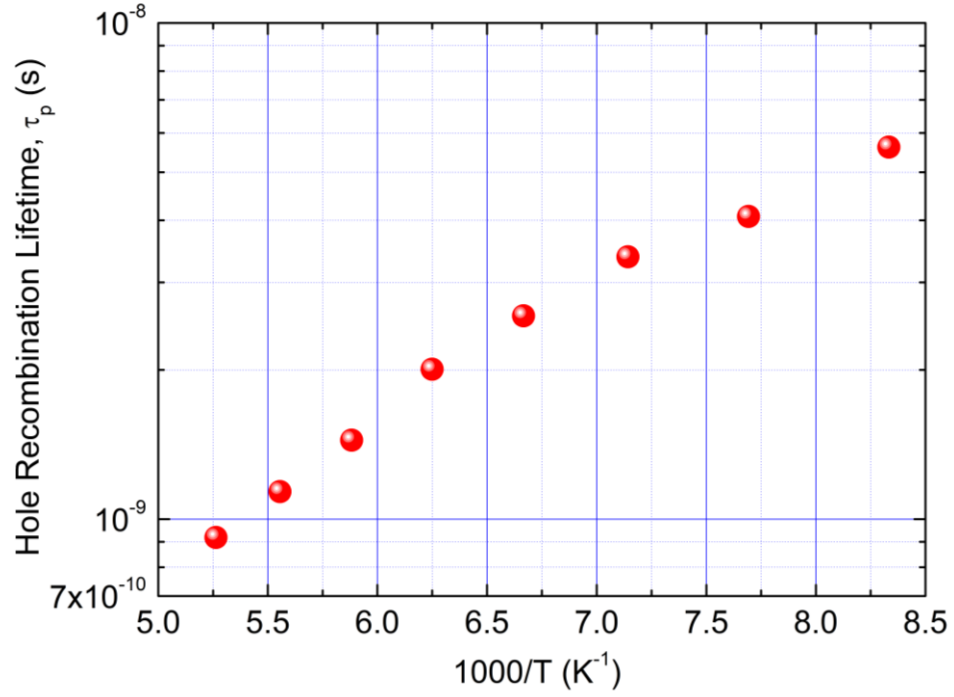
Figure 4.14. The hole recombination lifetime, τ_p at various temperatures.

A precise estimation of $\tau_{pG\text{-}R}$ is performed in this study by combining the data extracted from the G-R and diffusion components of the dark current obtained through dark current analysis as follows.

The net recombination rate due to the SRH process is expressed as

$$R = \frac{np - n_i^2}{\tau_{pG-R}(n + n_1) + \tau_{nG-R}(p + p_1)}. \tag{4.16}$$

In the depletion regions where n and p are negligibly small, the above expression can be written as

$$R = \frac{-n_i^2}{\tau_{pG-R}n_1 + \tau_{nG-R}p_1} = G \tag{4.17}$$

where

$$n_1 = n_i e^{\frac{E_T - E_i}{kT}} \quad and \quad p_1 = n_i e^{\frac{E_i - E_T}{kT}}. \tag{4.18}$$

In the above expression, E_t is the trap level energy and E_i is the intrinsic level.

Electron and hole G-R lifetimes can be expressed in terms of the electron and hole capture cross sections (σ_n and σ_p), thermal velocity (v_{th}) and trap density (N_T) as

$$\tau_{nG-R} = \frac{1}{\sigma_n v_{th} N_T} \quad and \quad \tau_{pG-R} = \frac{1}{\sigma_p v_{th} N_T}. \tag{4.19}$$

Inserting the expressions for n_1 and p_1 into Equation (4.17), the SRH net recombination rate in the depletion region is obtained as

$$R = \frac{-n_i^2}{\tau_{pG-R} n_i e^{\frac{E_T - E_i}{kT}} + \tau_{nG-R} n_i e^{\frac{E_i - E_T}{kT}}}. \tag{4.20}$$

If the effective G-R recombination lifetime ($\tau_{\text{G-R}}$) is defined as

$$\tau_{G-R} = \tau_{pG-R} \left(e^{\frac{E_T - E_i}{kT}} + K e^{\frac{E_i - E_T}{kT}} \right). \tag{4.21}$$

$$K = \frac{\tau_{nG-R}}{\tau_{pG-R}} = \frac{\sigma_n}{\sigma_p}. \tag{4.22}$$

$$R \cong \frac{-n_i^2}{\tau_{G-R}}. \tag{4.23}$$

Since net recombination rate is defined as the difference between the recombination and generation rates, negative net recombination rate means that generation rate is exceeding the recombination rate which makes sense due to the absence of free carriers in the depletion region. Therefore, the SRH mechanism taking place in the depletion region contributes to the reverse current of the diode by the generation of carriers in the depletion region through the trap level.

The position of the trap level E_T with respect to E_i can be obtained if $\tau_{\text{G-R}}$ and τ_{pG-R} are extracted from the G-R and diffusion components of the dark current and Equation (4.21) is utilized. Since the ratio of the capture cross sections (K) is an additional

unknown, Equation (4.21) must be fitted to the experimental data using the effective G-R lifetimes ($\tau_{G\text{-}R}$) and hole G-R recombination lifetime ($\tau_{pG\text{-}R}$) extracted through I-V measurements conducted at various temperatures. It should be noted that $\tau_{pG\text{-}R}$ can be obtained using Equation (4.15) if the Auger and radiative recombination lifetimes are known, since the hole recombination lifetime τ_p has already been extracted from the diffusion current coefficient as shown in Figure 4.14. For this purpose, we have separately calculated the Auger and radiative lifetimes in the HgCdTe material of interest to construct the following plot (Figure 4.15) for $\tau_{pAuger,radiative}$ which is the overall hole recombination lifetime that would be obtained in case only the Auger and radiative recombination processes are active (no SRH process). Hence τ_{pAuger} is the Auger lifetime resulting from Auger 1 and Auger 7 processes while Auger 7 is not to be dominant in the n-side of the diode where most of the diffusion current is generated.
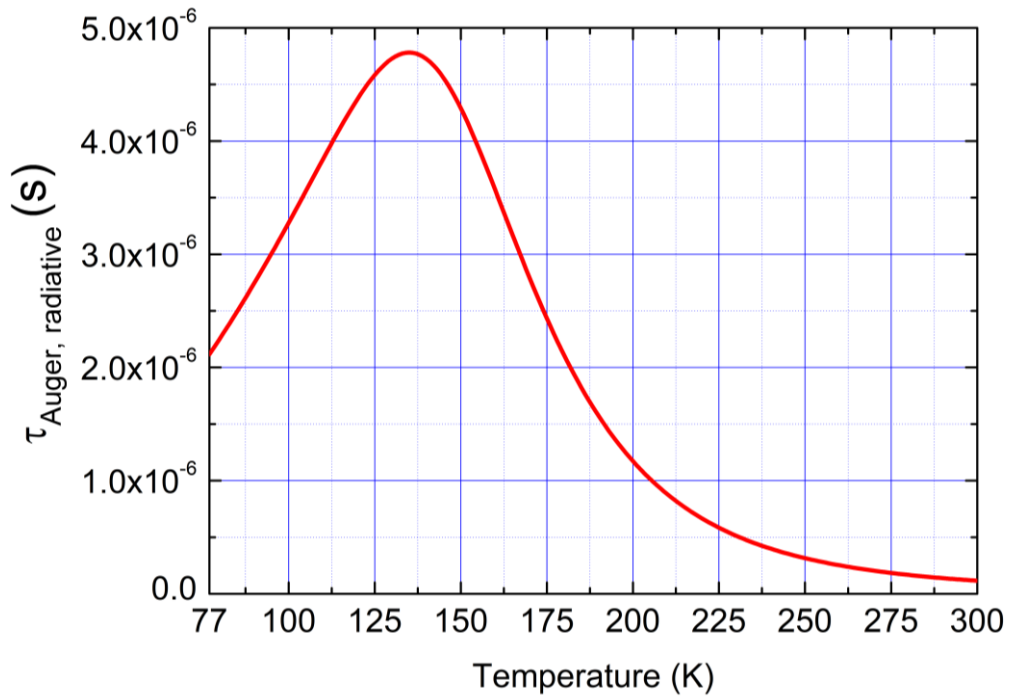

Figure 4.15. The Auger and radiative recombination lifetime at various temperatures.

79

As seen from the above plot and Equations (4.14)-(4.15), overall hole recombination lifetime τ_p will be governed by the hole G-R lifetime (τ_{pG-R}) if the latter is much smaller than $\tau_{Auger,radiative}$.

$$\frac{1}{\tau_p} \cong \frac{1}{\tau_{pG-R}} \quad if \ \tau_{pAuger,radiative} \gg \tau_{pG-R}. \qquad (4.24)$$

When Figure 4.14 and Figure 4.15 are compared, it can be concluded that the hole recombination lifetime, τ_p, is governed by τ_{pG-R} since the τ_p extracted from the diffusion current modeling is much smaller than the recombination lifetime due to the combination of Auger and radiative recombination mechanisms. As will be described below, we have used the extracted values of τ_{pG-R} together with the effective G-R lifetime, τ_{G-R}, (determined from the G-R component of the dark current) in order to find the location of the dominant trap responsible for the G-R current.

The temperature dependency of the effective G-R lifetime is presented in Figure 4.16 (green spheres). This data is extracted from the G-R component of the dark current (Equation (4.3)) through dark current analysis at detector temperatures where the G-R current is not negligible. Figure 4.16 also shows the fit of Equation (4.21) to this data by setting the hole G-R lifetime (τ_{pG-R}) equal to the hole recombination lifetime (τ_p) obtained from the diffusion current. There is good agreement between Equation AB and the measurement data in case E_T-E_i in Equation (4.21) is set to have E_g-$E_t=0.64E_g$ and $K=\sigma_p/\sigma_n=0.12$. This result shows that the dominant trap level generating the G-R component of the dark current resides $0.36E_g$ (roughly $E_g/3$) above the valence band edge. A hole trap at this energy has been reported by different research group [73], [74]. Unikovsky and Nemirovsky [75] observed two traps in $Hg_{0.78}Cd_{0.22}Te$ detectors by dark current characterization. The trap energies were identified as ~$E_g/3$ and ~$2E_g/3$ with the former trap energy being very close to our finding. The authors have observed strong TAT current generated by those traps.
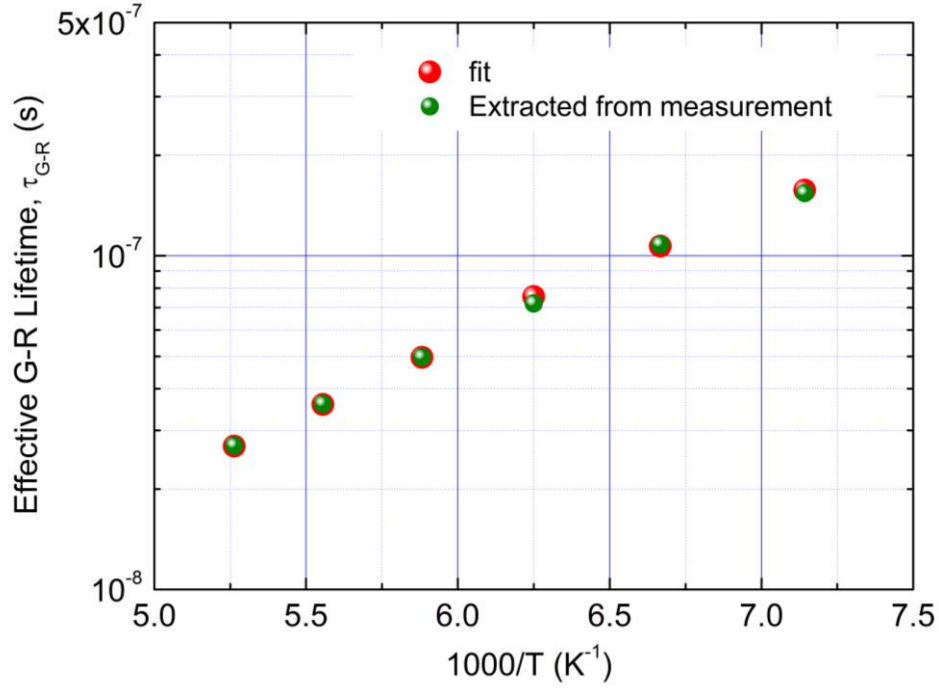
Figure 4.16. The effective G-R lifetime and fit results.

Having determined the hole G-R lifetime, τ_{pG-R}, information regarding the trap properties can be obtained through Equation (4.19). However, there are two unknowns in this expression which are hole capture cross section σ_p and the trap density N_t. As described below, we estimated the order of these parameters, through the TAT current component of the dark current obtained by dark current analysis.

Since the G-R current component of the detector suggests the presence of a trap at an energy level of $0.36E_g$, it can be argued that this trap may also be generating the TAT current observed through the I-V characterization of the detectors. Since, the barrier from the trap level to the conduction band is larger than the tunneling rate from the valence band to the trap level, the TAT current generated by this trap should be limited by the former. Therefore, we have used Equations (4.8) and (4.9) to model the TAT current due to this trap with E_g-E_t=0.64E_g and $N_t \cong 2.5 \times 10^{14}$ cm^{-3}. As shown in Figure 4.17, the model predictions are in good agreement with the measurement results in the bias and temperature regions where the TAT current is significant.
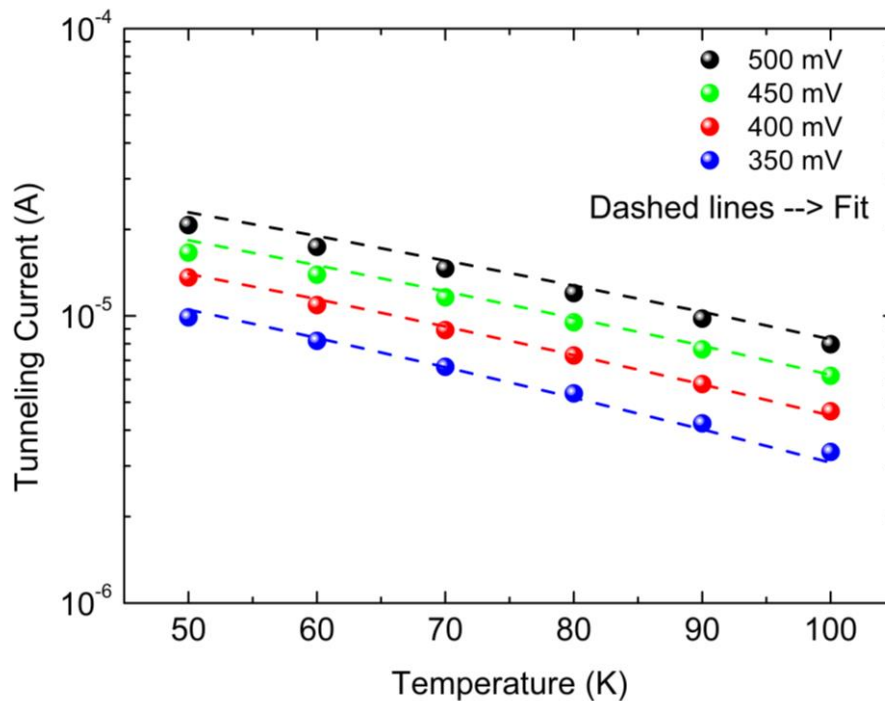
Figure 4.17. TAT current modelling.

After obtaining various parameters needed for more detailed dark current analysis, we performed dark current modeling at different temperatures in a wide enough bias region. Figure 4.18, Figure 4.19 and Figure 4.20 present detailed dark current modeling results at 130, 150 and 180 K operation temperatures, respectively. At 130 K operation temperature, the dominant component of the dark current is diffusion under low reverse bias voltages while the bias dependent shunt leakage exceeds the diffusion component as the reverse bias reaches moderate range. The G-R current is insignificant in the entire bias range. However, as will be shown in the following sections, the G-R component of the dark current is effective in determining the signal to noise ratio of the detector at low frequencies by introducing considerable 1/f noise at the typical bias voltages under the operation conditions. The significance of the dark current sets in under larger bias voltages where the dark current of the detector starts to be dominated by this relatively temperature insensitive current component. At 150 K, the detector is diffusion limited at low bias voltages and the TAT mechanism starts to contribute to the dark current beyond 300 mV reverse bias voltage. On the other

hand, as the temperature increases, the TAT mechanism becomes negligible and the detector reaches diffusion limited condition. The dark current of the detector is dominated by the diffusion component under low and moderate bias voltages at temperatures at and above 150 K.

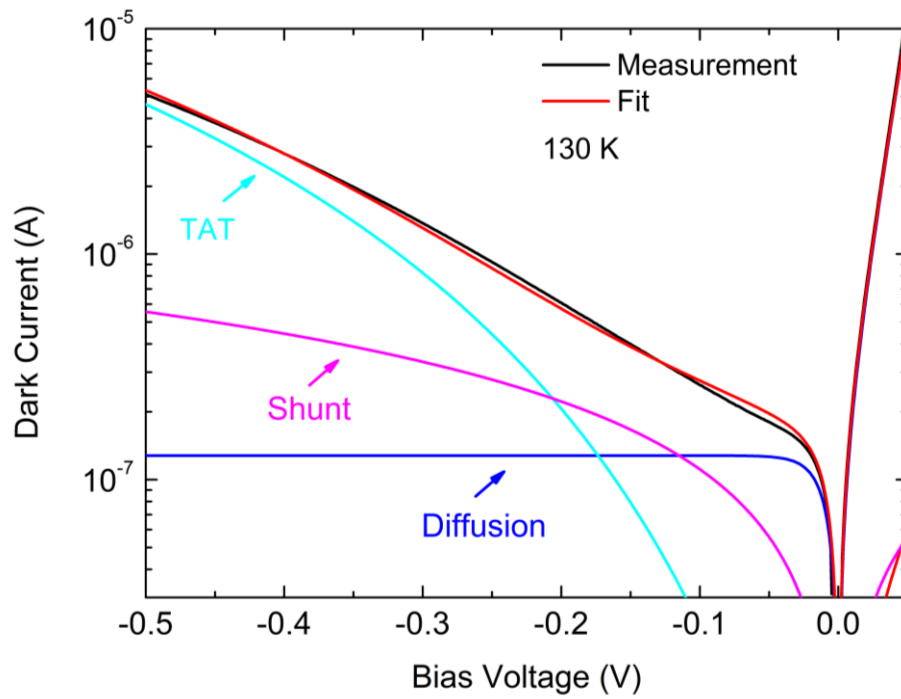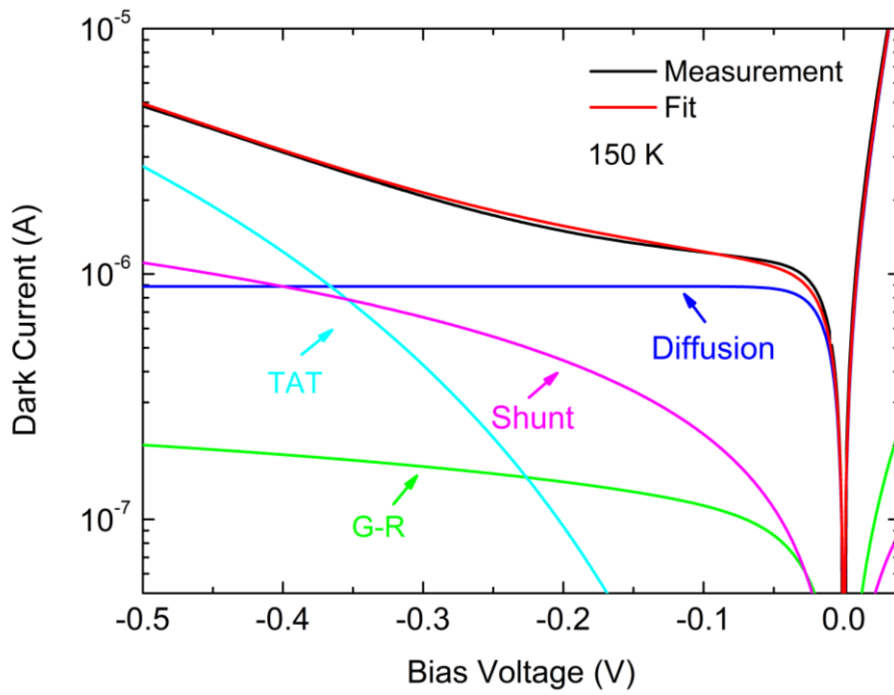

Figure 4.18. Dark current modeling at 130 K.

Figure 4.19. Dark current modeling at 150 K.
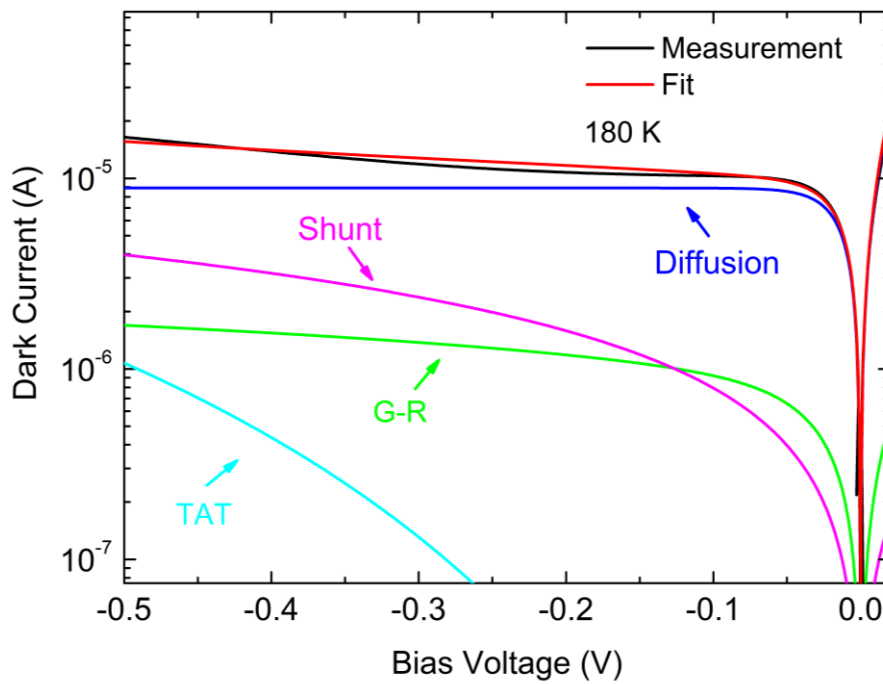
Figure 4.20. Dark current modeling at 180 K.

84

There are two possible sources of the shunt leakage current namely surface effects and dislocations in the material. Gopal and his research group [76] have constructed a theoretical model to investigate the ohmic shunt resistance in HgCdTe junction. They related the ohmic leakage with recombination mechanisms in the junction. Since the G-R mechanism changes with intrinsic carrier concentration, the temperature dependence of the shunt resistance should be correlated with n_i. Besides, they discussed the temperature dependency of the shunt resistance in terms of the source of the leakage current with different surface charge densities at interface or around dislocations, and they reported similar behavior of the shunt resistance whether it is originated from interface or bulk. Hence, it is difficult to distinguish the origin of leakage current by only analyzing the change of the shunt resistance with temperature.

The trend of the shunt resistance with temperature differs with respect to surface condition (accumulation, inversion or depletion). If the transition of space charge region from depletion to inversion occurs due to increasing charge density with temperature, the shunt resistance tends to be saturated at low temperature. In our detector, at high temperatures, the shunt resistance changes with n_i, however, it saturates at low temperatures. Figure 4.21 shows the shunt resistance extracted by the dark current modeling at various temperatures. Unfortunately, without additional data such as the sign of the fixed charges at the interface, the origin of the shunt leakage current cannot be determined.
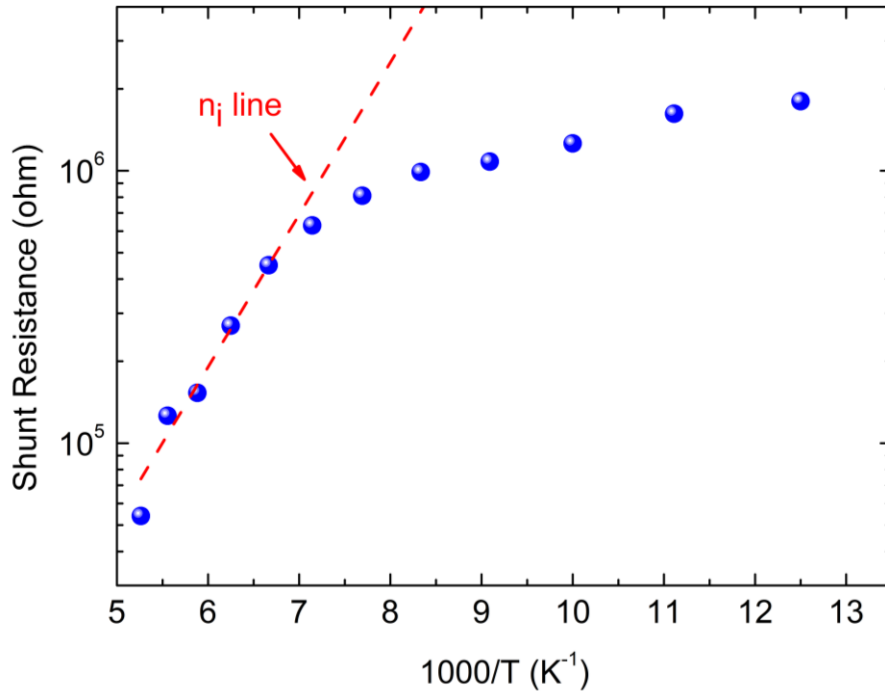
Figure 4.21. The shunt resistance of the detector at various temperatures.

In order to identify the origin of the shunt leakage current, the 150 K I-V characteristic of a detector fabricated with the same wafer (with similar pixel dimensions) but with a different passivation process was compared to the characteristics of the detector which was fabricated in this thesis study. The other detector was fabricated at the Quantum Devices and Nanophotonics Research Laboratory of the Electrical and Electronics Engineering Department of METU. The same parameters were used to fit the dark current component expressions except the trap density (2.5×10^{13} cm^{-3} in the detector fabricated at METU). Besides, there does not exist shunt leakage at the detector fabricated at METU. This is an indication showing that the shunt leakage originates from the surface due to unideal passivation in the other detectors. In addition, it shows a strong evidence for the shunt leakage current originated surface effects and explains the reason of saturated shunt resistance at low temperatures. On the other hand, similar G-R currents in the detectors suggests that the G-R component of the dark current arises from bulk mechanisms. Another interesting observation is the suppressed TAT current in the detector fabricated at METU indicating an order of

magnitude decrease in the trap density. It is not clear yet why the detectors exhibit different trap densities. This difference may be attributed to different annealing processes and possible annihilation of most of the traps by the annealing process applied at METU. Indeed, the detector fabricated at METU yielded dark current densities almost in the order of 10^{-5} A/cm^2 under low bias voltages at 78 K.

Another data that can be extracted from the above analysis is the capture cross section of the trap at $0.36E_g$. Hence, already obtained hole G-R recombination lifetime can be expressed in terms of the hole capture cross section (σ_p) as

$$\tau_{pG-R} = \frac{1}{\sigma_p v_{th} N_t}.$$

<div align="right">(4.25)</div>

The thermal velocity in the above expression can be modeled as $(8kT/\pi m^*_{hh})$ where m^*_{hh} is the heavy hole effective mass ($0.55m_o$) [66]. Figure 4.22 shows the variation of the hole capture cross section with temperature for $N_t=2.5\times10^{14}$ cm^{-3} (as determined from TAT current fit). The trap exhibits a repulsive capture barrier [77] of 50 meV. It should be noted that these properties can be verified through deep level transient spectroscopy (DLTS) measurements. For the time being, we are not able to verify these properties through the data existing in the literature due to limited information on the characteristics of traps in HgCdTe as well as the difficulty of DLTS measurements on traps with capture barriers.
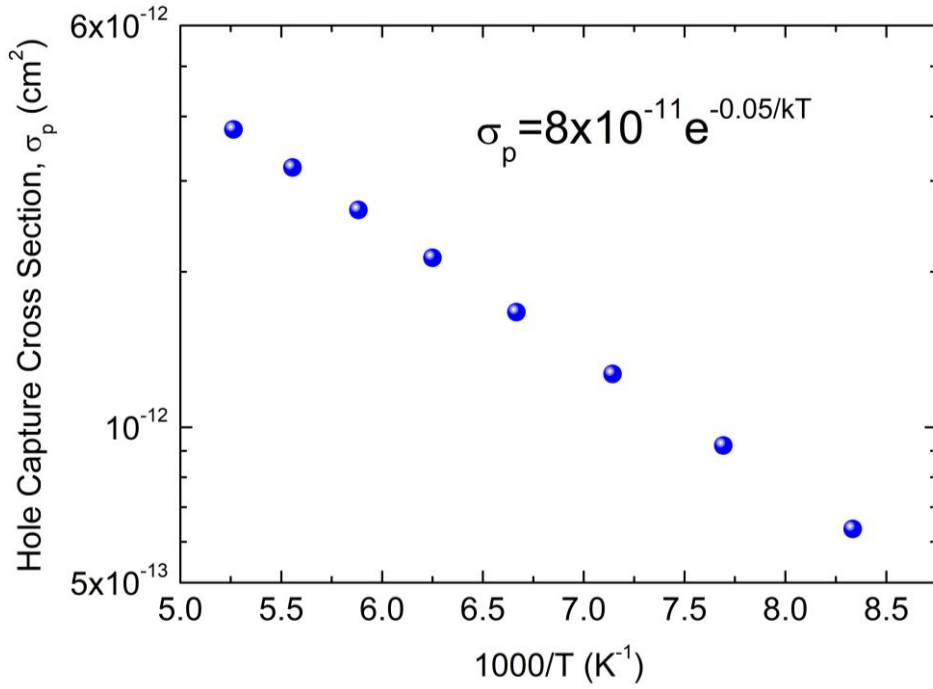
Figure 4.22. Variation of hole capture cross section with temperature.

4.2.3. Noise Analysis

After the detailed analysis of dark current components of the diode, spectral noise measurements were performed at METU with Agilent 3570A Dynamic Signal Analyzer in order to identify the noise contributions of different dark current mechanisms. Noise current spectral density measured at 90 K with different bias voltages is shown in Figure 4.23.

As indicated before, at low temperatures, the dark current is strongly dominated by TAT and shunt currents under moderate and large reverse bias voltages. 1/f noise contribution of the TAT mechanism can be expressed by the following relation [68]

$$i_{n-TAT} = \alpha_{TAT}(I_{TAT})^\beta \qquad (4.26)$$

where α_{TAT} and β are the fitting parameters. On the other hand, it should be noted that at low bias voltages, G-R dark current component is also likely to contribute to 1/f

noise. The relation between 1/f noise and G-R component of the dark current can be expressed as [78]

$$i_{n-G-R} = \alpha_{G-R} I_{G-R} \qquad (4.27)$$

where α_{G-R} is fitting parameter.

The contribution of the shunt current component to the 1/f noise can be described as [79]

$$i_{n-SH} = \alpha_{SH} I_{SHUNT}. \qquad (4.28)$$
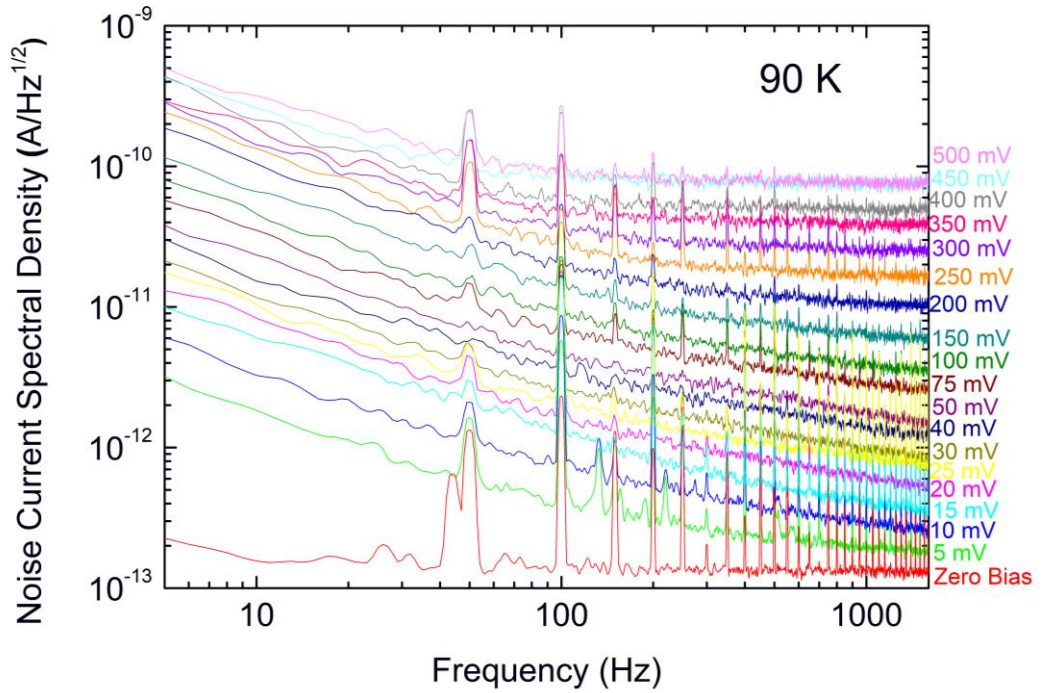
Figure 4.23. Noise current spectral density of the detector at 90 K.

1/f noise at 1 Hz is determined for different bias voltages by extrapolating the data and curve fitting is performed considering the shunt leakage and TAT mechanisms as shown in Figure 4.24. At low bias voltages, since the dark current is dominated by shunt leakage (TAT is negligible) at 90 K, measured 1/f noise comprises with ohmic leakage mechanism contribution with $\alpha_{SH}=1.2 \times 10^{-3}$ which is close to the shunt current coefficient of noise contribution [79]. As bias voltage increases, TAT mechanism

starts to contribute the 1/f noise of the detector with $\alpha_{TAT}=0.8\times10^{-6}$ and $\beta=0.57$ which are very close to the fitting parameters obtained by Nemirovsky and Unikovsky for LWIR HgCdTe with cadmium mole fraction of 0.22 [68]. Since the G-R component of the dark current at 90 K is negligible due to high effective G-R lifetime, additional measurements were needed in order to determine the noise coefficient of the G-R mechanism.
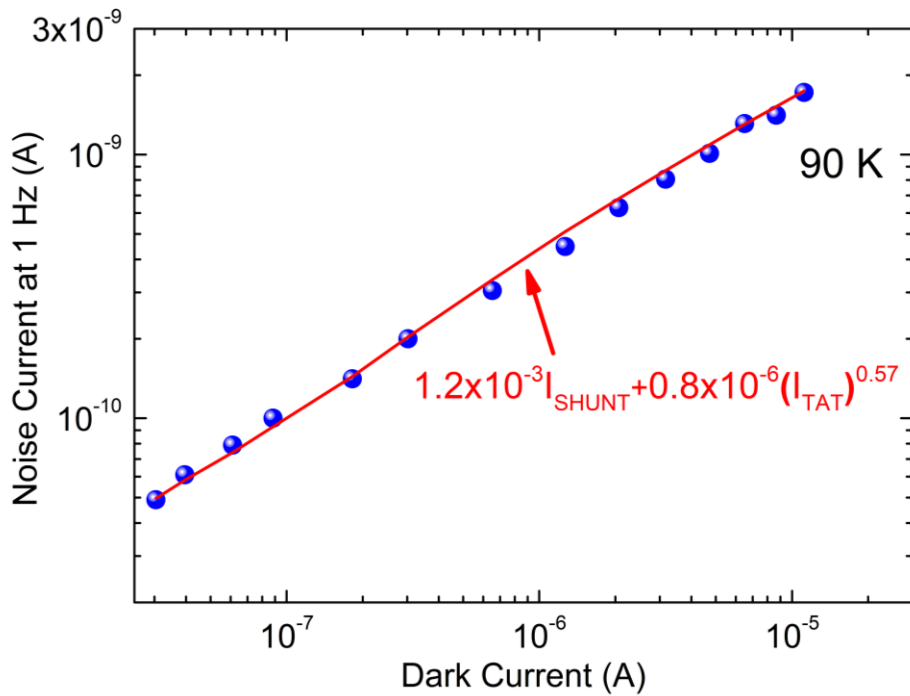
Figure 4.24. Noise current fit with combination of shunt and TAT current contributions at 90 K.

Noise current spectral density was measured at various temperatures under 500 mV reverse bias in order to determine the contribution of the G-R mechanism to 1/f noise as shown in Figure 4.25. By combining the data obtained through 90 K noise fitting with variable temperature noise measurements under 500 mV reverse bias, α_{G-R} was found as 3×10^{-4} as shown in Figure 4.26. This value of α_{G-R} is close to those reported for detectors constructed with other materials [79].

90
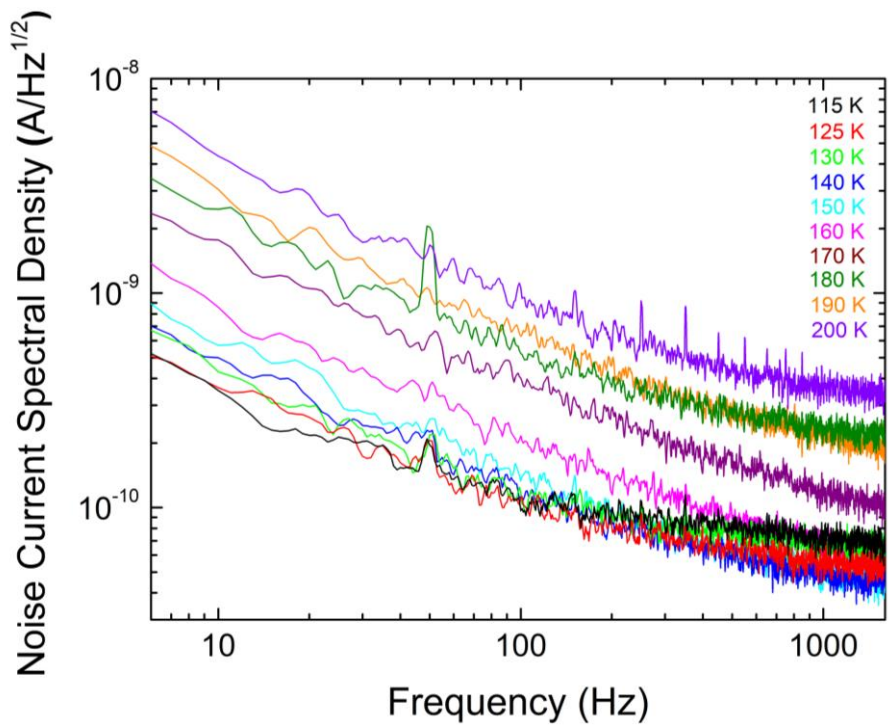
Figure 4.25. Noise current spectral density of detector at various temperatures.
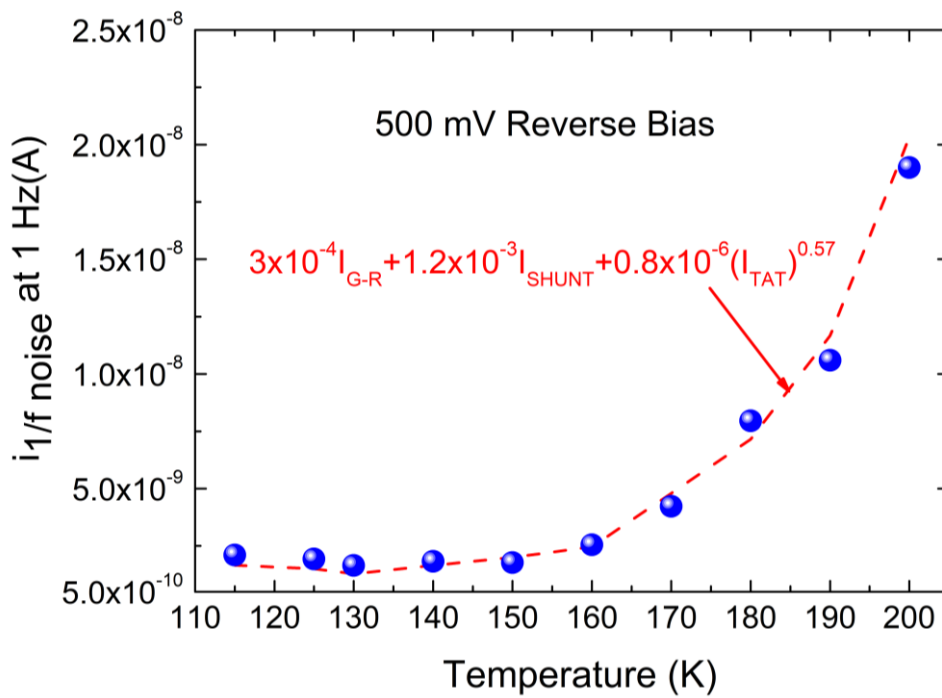
Figure 4.26. Noise current fit considering all contributor components.

91

4.2.4. Responsivity and Quantum Efficiency

The responsivity measurement procedure consists of measurement of blackbody response, measurement of normalized spectral response and calculation of the peak factor. Blackbody responsivity which is defined as the signal output from a detector in response to 1 Watt of modulated power at frequency f from a blackbody at temperature T should be measured first. Since the blackbody radiates at the whole wavelength spectrum, the portion of the radiation integrated by detector should be considered by calculating the peak factor (Figure 4.27). The normalized spectral response of the detector is measured and multiplied with blackbody exitance in order to find the portion of the radiation integrated by the detector. Then, the peak factor is calculated as follows

$$peak\ factor = \frac{Total\ Amount\ of\ Radiation}{The\ Portion\ of\ Radiation\ Integrated\ by\ Detector}. \quad (4.29)$$

In order to find the responsivity spectrum of detector, the normalized spectral response is multiplied with the peak factor.

Blackbody responsivity was measured by using a blackbody integrated with a chopper, a preamplifier and a lock-in amplifier. Lock-in amplifier was locked at the frequency of the chopper which modulates the radiation. The test setup is illustrated in Figure 4.28. The blackbody was set to 500 ºC and the chopper frequency was at 23 Hz. The detector was at 78 K in a liquid nitrogen dewar. The optical power falling on detector was calculated by considering the blackbody temperature and aperture diameter, distance of the detector to blackbody, the detector area and window transmission. The output of the lock in amplifier was multiplied with the preamplifier trans-impedance gain and divided by power falling on the detector. The blackbody responsivity of Pixel Array-3, R_{BB}, was calculated as 2.26 A/W.
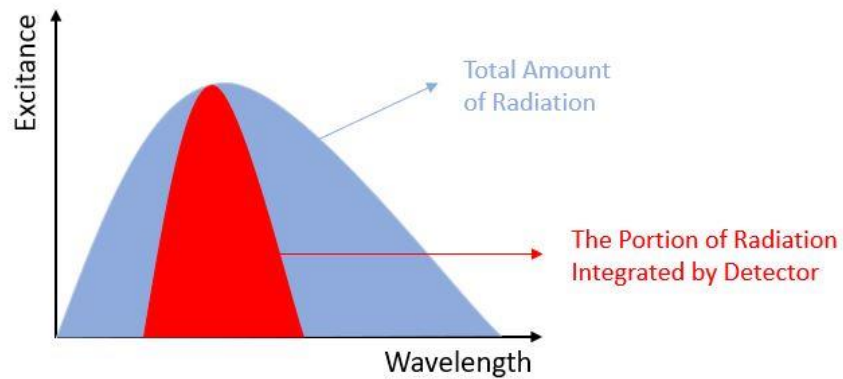
Figure 4.27. Representation of blackbody exitance and detector normalized spectral response.

The normalized spectral response of the detector at 78 K was obtained with an FTIR system. The 50% cut-off wavelength of the detector was measured to be ~9.5 μm. The peak factor was found as 2.34 as explained previously.
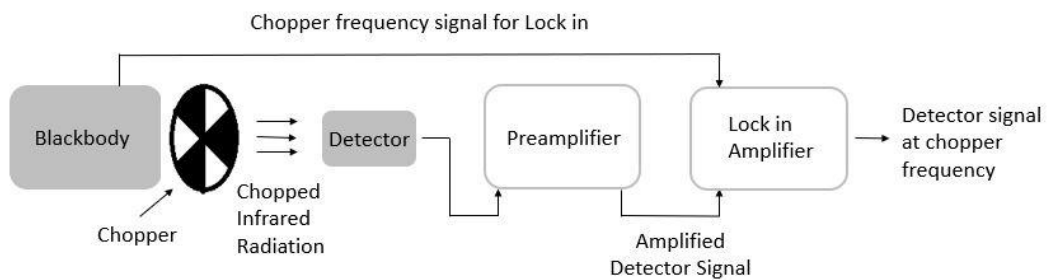
Figure 4.28. Blackbody responsivity measurement setup configuration.

After measuring the blackbody responsivity and calculating the peak factor, the peak responsivity was found as 5.3 A/W resulting in the spectral response shown in Figure 4.29. Surface reflection loss was accounted for while calculating the responsivity and the intrinsic quantum efficiency of the detector.
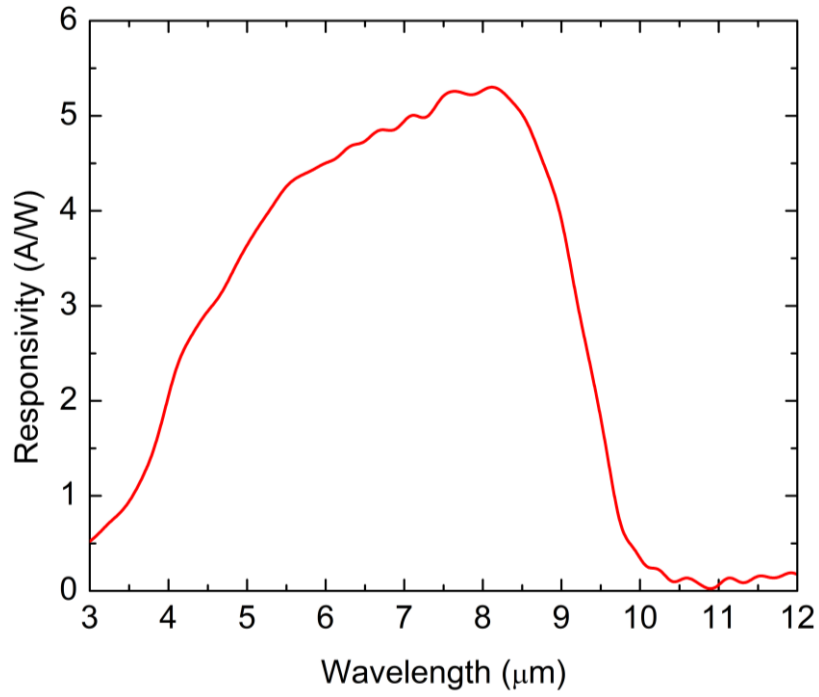
Figure 4.29. Responsivity spectrum of Pixel Array-3.

The correlation between the quantum efficiency and responsivity is expressed as follows

$$R = \eta \frac{\lambda}{1.24}. \qquad (4.30)$$

Quantum efficiency was calculated as ~80% from Equation (4.30). The quantum efficiency spectrum is illustrated in Figure 4.30.
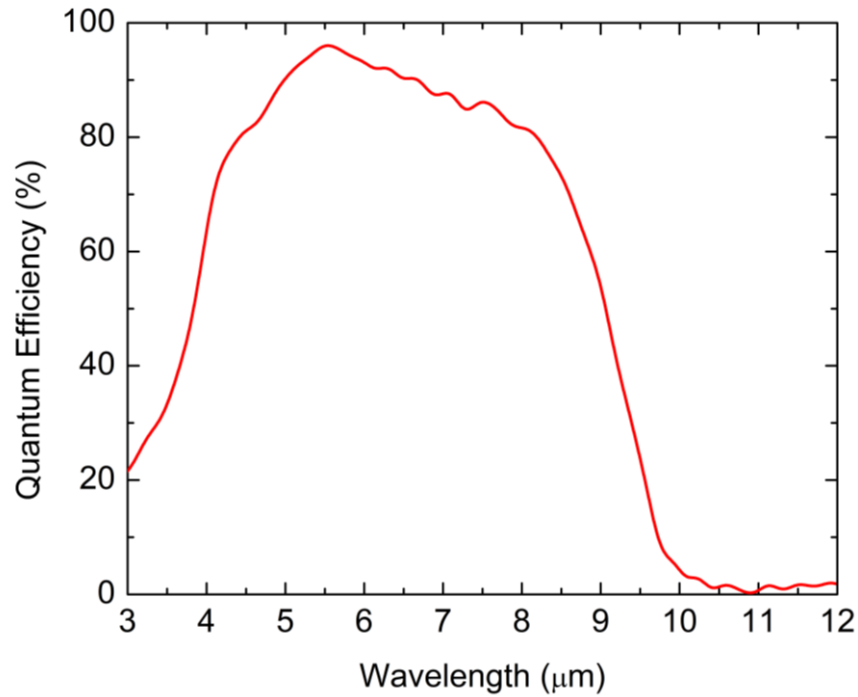
Figure 4.30. Quantum efficiency spectrum of Pixel Array-3.

4.3. FPA Level Characterization

Specific detectivity and NETD were calculated from the dark current, noise and responsivity measurements by using Equation (1.13) and (1.14) for f/2 optics at 1 kHz frequency (where the dominant noise components are shot and Johnson). Specific detectivity was found to be ~1×10^{11} cmHz$^{1/2}$/W. Figure 4.31 shows the corresponding NETD of the FPA versus the integration time. ROIC noise (~1000 e$^-$) was included in the NETD calculations. The FPA exhibits desirable NETD characteristic even with integration times in the order of micro-seconds.
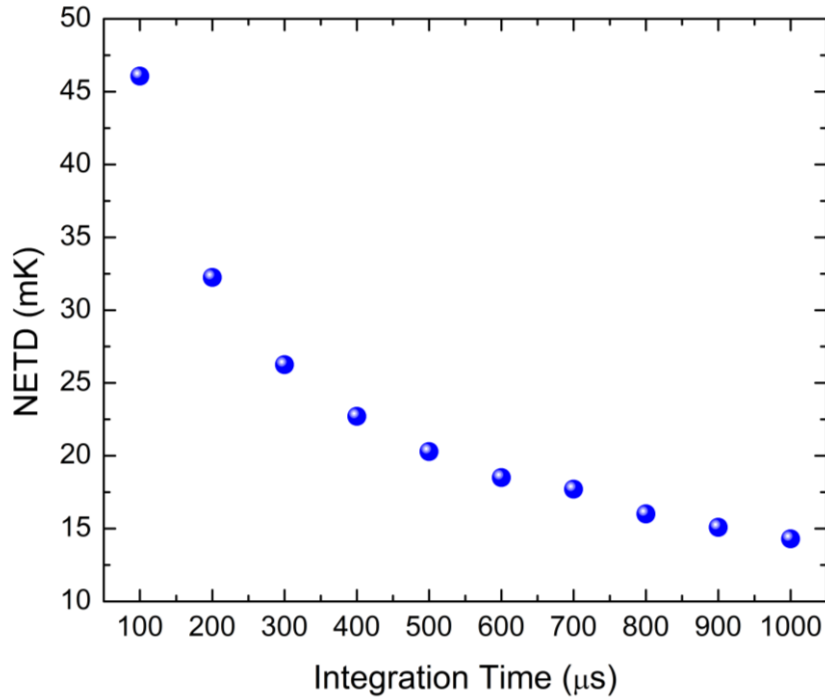
Figure 4.31. Calculated NETD for various integration time.

Fabricated FPA with 320x256 format and 30 μm pixel pitch was flip-chip bonded to commercial ISC0903 ROIC produced by FLIR Systems. A dewar with f/2 aperture and a blackbody source were used to characterize the FPA connected to imager electronics. Operability of the FPA was ~83% for ~400 μs integration time (pixels with NETD higher than two times of the mean NETD were defined as defective).The dead pixels were due to imperfect processing applied to a part of the FPA which is visible as image degradation in this part as can be seen from the thermal images given in Figure 4.32 and Figure 4.33. Responsivity nonuniformity of the FPA was 22%. It should be noted that above reported characteristics were obtained on the detectors fabricated with an unoptimized passivation process.

Figure 4.32. Indoor image taken by 320x256 heterojunction FPA.

Figure 4.33. Outdoor image taken by 320x256 heterojunction FPA.

CHAPTER 5

CONCLUSION

This thesis study reports the detailed dark current analysis concentrating on the performance degrading mechanisms in the LWIR HgCdTe p on n detectors. The epilayer was grown by MBE on CdZnTe substrates at the Quantum Devices and Nanophotonics Research Laboratory of the Electrical and Electronics Engineering Department of METU. 320x256/30 μm pitch FPA with cut-off wavelength of 9.5 μm (78 K) and pixel arrays were fabricated for optical and electrical characterization.

Dark current modeling including diffusion, generation-recombination, shunt and trap assisted tunneling currents were carried out at various temperatures. While the detectors exhibit diffusion dominated dark current at temperatures at and above 130 K under reverse bias voltages, the major component of the dark current is trap assisted tunneling at low temperatures (80 K). One of the objectives of this work was the analysis of the trap assisted tunneling current which is dominant current mechanism at operating temperatures for LWIR HgCdTe detectors and investigation of trap properties including the trap energy level, the trap density and the capture cross section characteristics. A hole trap in the n-side at an energy of $0.36E_g$ measured from the valence band edge was found with a density in the order of 10^{14} cm^{-3}. Another major dark current component in the detector was found to be the shunt leakage current which seemed to result from the surface conditions due to unideal passivation process. The noise measurements and modeling indicate that the shunt current component introduces significant 1/f noise with a noise coefficient comparable to that of the G-R current which is in the order of 10^{-3}. The TAT current was also observed to introduce 1/f noise to exhibit noise current at 1 Hz expressed as $0.8 \times 10^{-6}(I_{TAT})^{0.57}$.

Specific detectivity of the detectors was found to be ~1×10^{11} cmHz$^{1/2}$/W corresponding to desirable NETD characteristic even with integration times in the order of micro-seconds.

In conclusion, this thesis study shed light on the detailed characterization of LWIR HgCdTe detectors including dark current modeling, noise analysis and optical properties. Different passivation techniques were compared in terms of dark current levels, and the performance degrading mechanisms were investigated. We believe that the results reported in this thesis will be invaluable for improving the performance of LWIR HgCdTe detectors in the mesa structure.

REFERENCES

[1]   A. Rogalski, "Infrared detectors: an overview," Infrared Phys. & Technol., vol. 43, no. 3-5, pp. 187-210, 2002.

[2]   E. S. Barr, "Historical survey of the early development of the infrared spectral region," Amer. J. of Phys., vol. 28, no. 1, pp. 42-54, 1960.

[3]   G. Gaussorgues and S. Chomet, "Infrared thermography," NDT & E Int., vol. 6, no. 29, p. 393, 1996.

[4]   A. Rogalski and K. Chrzanowski, "Infrared devices and techniques," Optoelectronics Review, vol. 10, no. 2, pp. 111-136, 2002.

[5]   V. I. Kostylev, "Bistatic radar: principles and practice", in Scattering Fundamentals, John Wiley & Sons, ch. 10, pp. 193-223, 2007.

[6]   A. Rogalski, "Infrared detectors," CRC press, 2010.

[7]   C. Besikci, "EE 514-Infrared devices and systems METU Lecture Notes," 2012.

[8]   G. D. Boreman, "Detectors," in Basic Electro-optics for Electrical Engineers, SPIE Press, ch. 5, pp. 67-69, 1998.

[9]   M. Henini and M. Razeghi, "HgCdTe 2D arrays-technology and performance limits," in Handbook of Infrared Detection Technologies, Elsevier, ch. 8, pp. 269-305, 2002.

[10]   A. Rogalski, "Infrared thermal detectors versus photon detectors: I. Pixel performance," Proc. of SPIE, vol. 3182, pp. 14-25, 1997.

[11]   H. C. Liu, M. Gao, J. McCaffrey, Z. R. Wasilewski, and S. Fafard, "Quantum dot infrared photodetectors," Appl. Phys. Lett., vol. 78, no. 1, pp. 79-81, 2001.

[12]   A. Rogalski, "HgCdTe infrared detector material: history, status and outlook," Rep. on Prog. in Phys., vol. 68, no. 10, p. 2267, 2005.

[13]   P. Y. Emelie, "HgCdTe auger-suppressed infrared detectors under non-equilibrium operation," Ph.D. dissertation, Dept. Elect. Eng., The Univ. of Michigan, 2009.

[14]   J. Stiens, C. De Tandt, G. Shkerdin, V. Kotov, R. Vounckx, and W. Vandermeiren, "Infrared thermo-electric photodetectors," in Laser Pulse Phenomena and Applications, ch.8, pp. 143-164, 2010.

[15]   W. Lei, J. Antoszewski, and L. Faraone, "Progress, challenges, and opportunities for HgCdTe infrared materials and detectors," Appl. Phys. Rev., vol. 2, no. 4, 041303, 2015.

[16]   R. S. Allgaier, "History of narrow-gap semiconductors and semimetals," 1945-65, Semicond. Science and Technol., vol. 5, no. 3S, 1990.

[17]   A. Rogalski, "History of infrared detectors," Opto-Electronics Rev., vol. 20, no. 3, pp. 279-308, 2012.

[18]   C. Downs and T. Vandervelde, "Progress in infrared photodetectors since 2000," Sensors, vol. 13, no. 4, pp. 5054-5098, 2013.

[19]   S. Kasap and A. Willoughby, "Mercury Cadmium Telluride: Growth, Properties and Applications," John Wiley & Sons, vol. 38, 2011.

[20]   G. L. Hansen, J. L. Schmit, and T. N. Casselman, "Energy gap versus alloy composition and temperature in Hg1−xCdxTe," J. of Appl. Phys., vol. 53, no. 10, pp. 7099-7101, 1982.

[21]   J. Wenus, J. Rutkowski, and A. Rogalski, "Two-dimensional analysis of double-layer heterojunction HgCdTe photodiodes," IEEE Trans. on Electron Devices, vol. 48, no. 7, pp. 1326-1332, 2001.

[22]   G. L. Hansen and J. L. Schmit, "Calculation of intrinsic carrier concentration in Hg1−xCdxTe," J. of Appl. Phys., vol. 54, no. 3, pp. 1639-1640, 1983.

[23]   G. K. O. Tsen, "Investigation of molecular beam epitaxy grown p-type mercury cadmium telluride for infrared detector applications," Ph.D. dissertation, Dept. Elect., Electron. and Comput. Eng., The Univ. of Western Australia, 2010.

[24]   M. H. Weiler, "Magnetooptical properties of Hg1-xCdxTe alloys," in Semiconductors and Semimetals, Elsevier, vol. 16, pp. 119-191, 1981.

[25]   J. P. Rosbeck, R. E. Starr, S. L. Price, and K. J. Riley, "Background and temperature dependent current-voltage characteristics of HgCdTe photodiodes," J. of Appl. Phys., vol. 53, no. 9, pp. 6430-6440, 1982.

[26]   T. K. Parashar, "Theoretical modelling of basics parameters of HgCdTe material," J. of Electron., vol. 6, pp. 295-303, 2017

[27]   J. Zhang, "A fundamental study of interface effects in HgCdTe materials and devices," Ph.D. dissertation, Dept. Elect., Electron. and Comput. Eng., The Univ. of Western Australia, 2015.

[28]   G. K. Ahluwalia and R. Patro, "Infrared detectors," in Applications of Chalcogenides: S, Se, and Te, Springer, pp. 409-445, 2017.

[29]   A. Rogalski, K. Adamiec, and J. Rutkowski, "Narrow-Gap Semiconductor Photodiodes," SPIE Press, 2000.

[30]   T. N. Casselman and P. E. Petersen, "A comparison of the dominant Auger transitions in p-type (Hg, Cd)Te," Solid State Commun., vol. 33, no. 6, pp. 615-619, 1980.

[31]   A. M. Itsuno, "Bandgap-engineered HgCdTe infrared detector structures for reduced cooling requirements," Ph.D. dissertation, Dept. Elect. Eng., The Univ. of Michigan, 2012.

[32]   A. Rogalski and W. Larkowski, "Comparison of photodiodes for the 3-5, 5 mu m and 8-14 mu m spectral regions," Electron Technol., vol. 18, no. 3, pp. 55-69, 1985.

[33]   A. Rogalski and R. Ciupa, "Long-wavelength HgCdTe photodiodes: n+-on-p versus p-on-n structures," J. of Appl. Phys., vol. 77, no. 7, pp. 3505-3512, 1995.

[34]   M. Chu, S. Terterian, D. Walsh, H. K. Gurgenian, S. Mesropian, R. J. Rapp, and W. D. Holley, "Recent progress on LWIR and VLWIR HgCdTe focal plane arrays," in Infrared Technology and Applications XXXI, SPIE, vol. 5783, pp. 243-250, 2005.

[35]   C. L. Jones, L. G. Hipwood, C. J. Shaw, J. P. Price, R. A. Catchpole, M. Ordish, C. D. Maxey, H. W. Lau, R. C. Mistry, M. C. Wilson, A. D. Parsons, J. Gillespie, L. Baggaley, M. Wallis, "High performance MW and LW IRFPAs made from HgCdTe grown by MOVPE," in Infrared Technology and Applications XXXII, SPIE, vol. 6206, p. 620610, 2006.

[36]   F. F. Sizov, V. V. Vasiliev, J. V. Gumenjuk-Sichevska, Y. E. Kamenev, S. A. Dvoretsky, and N. N. Mikhailov, "MCT detectors: From IR to sub-mm and mm wavelength bands," in Optical Design and Engineering III, SPIE, vol. 7100, p. 71002C, 2008.

[37]   M. B. Reine, "History of HgCdTe infrared detectors at BAE Systems," in Infrared Technology and Applications XXXV, SPIE, vol. 7298, p. 72982S, 2009.

[38]   L. Mollard, G. Destefanis, N. Baier, J. Rothman, P. Ballet, J. P. Zanatta, M. Tchagaspanian, A. M. Papon, G. Bourgeois, J. P. Barnes, C. Pautet, P. Fougeres, "Planar p-on-n HgCdTe FPAs by arsenic ion implantation," J. of Electron. Mater., vol. 38, no. 8, pp. 1805-1813, 2009.

[39]   J. Ziegler, D. Eich, S. Hanna, A. Bauer, H. Bitterlich, M. Bruder, K. M. Mahlein, H. Lutz, T. Schallenberg, J. Wenisch, R. Wollrab, (2010). "Recent results of two-dimensional LW-and VLW-HgCdTe IR FPAs at AIM," in Infrared Technology and Applications XXXVI, SPIE, vol. 7660, p. 766038, 2010.

[40]   Y. Reibel, L. Rubaldo, G. Bonnouvrier, S. Verdet, D. Billon-Lanfrey, G. Destéfanis, L. Mollard, J. Baylet, J. Rothman, G. Druart, N. Guerineau, "Latest developments in advanced MCT infrared cooled detectors," in Electro-Optical and Infrared Systems: Technology and Applications VIII, SPIE, vol. 8185, p. 818503, 2011.

[41]   L. Mollard, G. Bourgeois, C. Lobre, S. Gout, S. Viollet-Bosson, N. Baier, G. Destefanis, O. Gravrand, J. P. Barnes, F. Milesi, A. Kerlain, L. Rubaldo, A. Manissadjian, "p-on-n HgCdTe infrared focal-plane arrays: from short-wave to very-long-wave infrared," J. of Electron. Mater., vol. 43, no.3, pp. 802-807, 2014.

[42]   J. Ziegler, H. Bitterlich, R. Breiter, M. Bruder, D. Eich, P. Fries, R. Wollrab, J. Wendler, J. Wenisch, "Large-format MWIR and LWIR detectors at AIM," in Infrared Technology and Applications XXXIX, SPIE, vol. 8704, p. 87042L, 2013.

[43]   P. Castelein, N. Baier, O. Gravrand, L. Mollard, D. Brellier, F. Rochette, A. Kerlain, L. Rubaldo, Y. Reibel, G. Destefanis, (2014). "Latest developments in the p-on-n HgCdTe architecture at DEFIR," in Infrared Technology and Applications XL, SPIE, vol. 9070, p. 90702Y, 2014.

[44]   R. Breiter, H. Figgemeier, H. Lutz, J. Wendler, S. Rutzinger, and T. Schallenberg, "Improved MCT LWIR modules for demanding imaging applications," in Infrared Technology and Applications XLI, SPIE, vol. 9451, p. 945128, 2015.

[45]   N. Baier, C. Cervera, O. Gravrand, L. Mollard, C. Lobre, G. Destefanis, G. Bourgeois, J. P. Zanatta, O. Boulade, and V. Moreau, "Latest developments in long-wavelength and very-long-wavelength infrared detection with p-on-n HgCdTe," J. of Electron. Mater., vol. 44, no. 9, pp. 3144-3150, 2015.

[46]   Y. Reibel, N. Péré-Laperne, L. Rubaldo, T. Augey, G. Decaens, V. Badet, L. Baud, J. Roumegoux, A. Kessler, P. Maillart, N. Ricard, O. Pacaud, G. Destéfanis, "Update on 10μm pixel pitch MCT-based focal plane array with enhanced functionalities," in Infrared Technology and Applications XLI, SPIE, vol. 9451, p. 94512E, 2015.

[47]   M. Haiml, D. Eich, W. Fick, H. Figgemeier, S. Hanna, M. Mahlein, W. Schirmacher, and R. Thöt, "Low dark current LWIR HgCdTe focal plane arrays at AIM," in Earth Observing Missions and Sensors: Development, Implementation, and Characterization IV, SPIE, vol. 9881, p. 988116, 2016.

[48]   N. Péré-Laperne, J. Berthoz, R. Taalat, L. Rubaldo, A. Kerlain, E. Carrère, and L. Dargent, "Latest developments of 10μm pitch HgCdTe diode array from the legacy to the extrinsic technology," in Infrared Technology and Applications XLII, SPIE, vol. 9819, p. 981920, 2016.

[49]   L. Rubaldo, R. Taalat, J. Berthoz, M. Maillard, N. Péré-Laperne, A. Brunner, P. Guinedor, L. Dargent, A. Manissadjian, Y. Reibel, A. Kerlain, "Latest improvements on long wave p on n HgCdTe Technology at Sofradir," in Infrared Technology and Applications XLIII, SPIE, vol. 10177, p. 101771E, 2017.

[50]   A. Rogalski, "Third-generation infrared photon detectors," Optical Engineering, vol. 42, no. 12, pp. 3498-3517, 2003.

[51]   M. A. Kinch, "HDVIP FPA technology at DRS infrared technologies," in Infrared Technology and Applications XXVII, SPIE, vol. 4369, pp. 566-578, 2001.

[52]   D. F. King, W. A. Radford, E. A. Patten, R. W. Graham, T. F. McEwan, J. G. Vodicka, R. E. Bornfreund, P. M. Goetz, G. M. Venzor, S. M. Johnson, J. E. Jensen, B. Z. Nosho, J. A. Roth, "Third-generation 1280× 720 FPA development status at Raytheon Vision Systems," in Infrared Technology and Applications XXXII, SPIE, vol. 6206, p. 62060W, 2006.

[53] G. Destefanis, J. Baylet, P. Ballet, P. Castelein, F. Rothan, O. Gravrand, J. Rothman, J. P. Chamonal, A. Million, "Status of HgCdTe bicolor and dual-band infrared focal arrays at LETI," J. of Electron. Mater., vol. 36 no. 8, pp. 1031-1044, 2007.

[54] Y. Reibel, F. Chabuel, C. Vaz, D. Billon-Lanfrey, J. Baylet, O. Gravrand, P. Ballet, G. Destefanis, "Infrared dual-band detectors for next generation," in Infrared Technology and Applications XXXVII, SPIE, vol. 8012, p. 801238, 2011.

[55] Y. Reibel, L. Rubaldo, C. Vaz, P. Tribolet, N. Baier, and G. Destefanis, "MCT (HgCdTe) IR detectors: latest developments in France," in Electro-Optical and Infrared Systems: Technology and Applications VII, SPIE, vol. 7834, p. 78340M, 2010.

[56] W. Hu, Z. Ye, L. Liao, H. Chen, L. Chen, R. Ding, L. He, X. Chen, W. Lu, "128× 128 long-wavelength/mid-wavelength two-color HgCdTe infrared focal plane array detector with ultralow spectral cross talk," Opt. Lett., vol. 39, no. 17, pp. 5184-5187, 2014.

[57] R. J. Martín-Palma and A. Lakhtakia, "Vapor-deposition techniques," in Engineered Biomimicry, Elsevier Inc., pp. 383-398, 2013.

[58] P. Capper, S. Irvine, and T. Joyce, "Epitaxial crystal growth: methods and materials," Springer Handbook of Electron. and Photon. Mater., pp. 271-301, 2007.

[59] S. Franchi, "Molecular beam epitaxy: fundamentals, historical background and future prospects," in Molecular Beam Epitaxy, Elsevier, pp. 1-46, 2013.

[60] E. Janik and R. Triboulet, "Ohmic contacts to p-type cadmium telluride and cadmium mercury telluride," J. of Phys. D: Applied Physics, vol. 16, no. 12, p. 2333, 1983.

[61] P. Boieriu, C. H. Grein, H. S. Jung, J. Garland, and V. Nathan, "Arsenic activation in molecular beam epitaxy grown, in situ doped HgCdTe (211)," Appl. Phys. Lett., vol. 86, no. 21, p. 212106, 2005.

[62] J. W. Garland, C. Grein, and S. Sivananthan, "Arsenic p-doping of HgCdTe grown by molecular beam epitaxy (MBE): a solved problem?," J. of Electron. Mater., vol. 42, no. 11, pp. 3331-3336, 2013.

[63] R. Pal, A. Malik, V. Srivastav, B. L. Sharma, V. R. Balakrishnan, V. Dhar, and H. P. Vyas, "Engineering interface composition for passivation of HgCdTe photodiodes," IEEE Trans. on Electron Devices, vol. 53, no. 11, pp. 2727-2734, 2006.

[64] V. Gopal, W. Qiu, and W. Hu, "Modelling of illuminated current–voltage characteristics to evaluate leakage currents in long wavelength infrared mercury cadmium telluride photovoltaic detectors," J. of Appl. Phys., vol. 116, no. 18, p. 184503, 2014.

[65] Y. Li, Z. H. Ye, C. Lin, X. N. Hu, R. J. Ding, and L. He, "Parameter determination from current–voltage characteristics of HgCdTe photodiodes in forward bias region," Opt. and Quantum Electron., vol. 45, no. 7, pp. 641-648, 2013.

[66] H. Kocer, Y. Arslan, and C. Besikci, "Numerical analysis of long wavelength infrared HgCdTe photodiodes," Infrared Phys. & Technol., vol. 55, no. 1, pp. 49-55, 2012.

[67] J. Wang, X. Chen, W. Hu, Z. Ye, C. Lin, X. Hu, J. Guo, F. Xie, J. Zhou, J. Liang, X. Wang, W. Lu, "Temperature dependence characteristics of dark current for arsenic doped LWIR HgCdTe detectors," Infrared Phys. & Technol., vol. 61, pp. 157-161, 2013.

[68] Y. Nemirovsky and A. Unikovsky, "Tunneling and 1/f noise currents in HgCdTe photodiodes," J. of Vac. Sci. & Technol. B: Microelectronics and Nanometer Structures Processing, Measurement, and Phenomena, vol. 10, no. 4, pp. 1602-1610, 1992.

[69] V. Gopal, S. K. Singh, and R. M. Mehra, "Analysis of dark current contributions in mercury cadmium telluride junction diodes," Infrared Phys. & Technol., vol. 43, no. 6, pp. 317-326, 2002.

[70] K. O. Boltar and N. I. Iakovleva, "HgCdTe photodiodes current-voltage characteristics simulation," in 17th International Conference on Photoelectron. and Night Vision Devices, SPIE, vol. 5126, pp. 43-51, 2003.

[71] Y. Shacham-Diamand and I. Kidron, "Haynes–Shockley experiment on n-type HgCdTe," J. of Appl. Phys., vol. 56, no. 4, pp. 1104-1108, 1984.

[72] W. E. Tennant, ""Rule 07" revisited: Still a good heuristic predictor of p/n HgCdTe photodiode performance?," J. of Electron. Mater., vol. 39, no. 7, pp. 1030-1035, 2010.

[73] C. E. Jones, K. James, J. Merz, R. Braunstein, M. Burd, M. Eetemadi, S. Hutton, J. Drumheller, "Status of point defects in HgCdTe," J. of Vac. Sci. & Technol. A: Vacuum, Surfaces, and Films, vol. 3, no. 1, pp. 131-137, 1985.

[74] R. Zucca, D. D. Edwall, J. S. Chen, S. L. Johnston, and C. R. Younger, "Minority carrier lifetimes of metalorganic chemical vapor deposition long-wavelength infrared HgCdTe on GaAs," J. of Vac. Sci. & Technol. B: Microelectronics and Nanometer Structures Processing, Measurement, and Phenomena, vol. 9, no. 3, pp. 1823-1828, 1991.

[75] A. Unikovsky and Y. Nemirovsky, "Trap-assisted tunneling in mercury cadmium telluride photodiodes," Appl. Phys. Lett., vol. 61, no. 3, pp. 330-332, 1992.

[76] V. Gopal and S. Gupta, "Temperature dependence of ohmic shunt resistance in mercury cadmium telluride junction diode," Infrared Phys. & Technol., vol. 45, no. 4, pp. 265-271, 2004.

[77] D. L. Polla and C. E. Jones, "Deep level studies of $Hg_{1-x}Cd_xTe$. I: Narrow-band-gap space-charge spectroscopy," J. of Appl. Phys., vol. 52, no. 8, pp. 5118-5131, 1981.

[78] L. Ciura, A. Kolek, J. Jureńczyk, K. Czuba, A. Jasik, I. Sankowska, and J. Kaniewski, "1/f Noise modeling of InAs/GaSb superlattice mid-wavelength infrared detectors," Opt. and Quantum Electron., vol. 50, no. 1, p. 36, 2018.

[79] C. Besikci, "Extended short wavelength infrared FPA technology: status and trends," in Quantum Sensing and Nano Electron. and Photon. XV, SPIE, vol. 10540, p. 105400P, 2018.